Synthesis, Deposition, and Microstructure Development of Thin Films Formed by Sulfidation and Selenization of Copper Zinc Tin Sulfide Nanocrystals

A DISSERTATION
SUBMITTED TO THE FACULTY OF THE
UNIVERSITY OF MINNESOTA
BY

Boris David Chernomordik

IN PARTIAL FULFILLMENT OF THE REQUIREMENTS
FOR THE DEGREE OF
DOCTOR OF PHILOSOPHY

Eray S. Aydil, Co-Advisor
David J. Norris, Co-Advisor

August 2014

Acknowledgements

I am forever grateful to my advisors, Eray Aydil and David Norris, who guided me and sculpted me into a scientist. Their support, advice, patience, and openness have helped me become a confident researcher. They will continue to be an inspiration to me in the future. I especially appreciate Eray's open door policy and that he will always make time to meet and help. I also greatly appreciate David's support and encouragement despite being across the globe.

I will cherish the memories and experiences of working with all of my fellow lab mates, past and present. I am particularly indebted to Andy Wills, Ayash Sahu, and Ankur Khare for training, supporting, and encouraging me in the early days. I also appreciate the invaluable help of Brent Keller and Alan Jacobs inn those early days. I am very grateful to Neema Rastgar, Melissa Johnson, Brian Merritt, Bryce Williams, Jonathan Hubbard, and Selin Tosun for the fun discussions and debates, for their help, and for their encouragement. Many thanks also to Mike Manno for always being there to answer a question in the most helpful way possible. I am indebted to undergraduate students Amélie Béland, Donna Deng, Anne Hunter, and Priyanka Ketkar, working with each of whom was a great pleasure and truly a rewarding experience. I also immensely appreciate the fun, friendly, and supportive workplace created by all the other group members including Sriharsha Jayanti, Nancy Trejo, Elliot Combs, Elijah Thimsen, Joel Abrahamson, and Xin Zhang.

I would also like to thank my collaborators, Prof. Lorraine Francis, Aloysius Gunawan, Prof. André Mkhoyan, Tom Pundsack, and Prof. David Blank, for their help, advice, and contributions.

Finally, I thank my friends and my family for their faith and encouragement. I am very thankful to my parents who always supported, encouraged, and guided me. I am especially grateful to my wife, Tammy, who read my drafts, listened to my presentations, gave me instrumental advice, carried me through the lows, and celebrated the highs.

To Tammy.

Abstract

Significant reduction in greenhouse gas emission and pollution associated with the global power demand can be accomplished by supplying tens-of-terawatts of power with solar cell technologies. No one solar cell material currently on the market is poised to meet this challenge due to issues such as manufacturing cost, material shortage, or material toxicity. For this reason, there is increasing interest in efficient light-absorbing materials that are comprised of abundant and non-toxic elements for thin film solar cell. Among these materials are copper zinc tin sulfide (Cu_2ZnSnS_4, or CZTS), copper zinc tin selenide ($Cu_2ZnSnSe_4$, or CZTSe), and copper zinc tin sulfoselenide alloys [$Cu_2ZnSn(S_xSe_{1-x})_4$, or CZTSSe]. Laboratory power conversion efficiencies of CZTSSe-based solar cells have risen to almost 13% in less than three decades of research.

Meeting the terawatt challenge will also require low cost fabrication. CZTSSe thin films from annealed colloidal nanocrystal coatings is an example of solution-based methods that can reduce manufacturing costs through advantages such as high throughput, high material utilization, and low capital expenses. The film microstructure and grain size affects the solar cell performance. To realize low cost commercial production and high efficiencies of CZTSSe-based solar cells, it is necessary to understand the fundamental factors that affect crystal growth and microstructure evolution during CZTSSe annealing.

Cu_2ZnSnS_4 (CZTS) nanocrystals were synthesized via thermolysis of single-source cation and sulfur precursors copper, zinc and tin diethyldithiocarbamates. The average nanocrystal size could be tuned between 2 nm and 40 nm, by varying the synthesis temperature between 150 °C and 340 °C. The synthesis is rapid and is completed in less than 10 minutes. Characterization by X-ray diffraction, Raman spectroscopy, transmission electron microscopy and energy dispersive X-ray spectroscopy confirm that the nanocrystals are nominally stoichiometric kesterite CZTS. The ~2 nm nanocrystals synthesized at 150 °C exhibit quantum confinement, with a band gap of 1.67 eV. Larger nanocrystals have the expected bulk CZTS band gap of 1.5 eV.

Several micron thick films deposited by drop casting colloidal dispersions of ~40 nm CZTS nanocrystals were crack-free, while those cast using 5 nm nanocrystals had micron-scale cracks. We showed the applicability of these nanocrystal coatings for thin film solar cells by demonstrating a CZTS thin film solar cell using coatings annealed in a sulfur atmosphere.

We conducted a systematic study of the factors controlling crystal growth and microstructure development during sulfidation annealing of films cast from colloidal dispersions of CZTS nanocrystals. The film microstructure is controlled by concurrent normal and abnormal grain growth. At 600 °C to 800 °C and low sulfur pressures (50 Torr), abnormal CZTS grains up to 10 μm in size grow on the surface of the CZTS nanocrystal film via transport of material from the nanocrystals to the abnormal grains. Meanwhile, the nanocrystals coarsen, sinter, and undergo normal grain growth. The driving force for abnormal grain growth is the reduction in total energy associated with the high surface area nanocrystals. The eventual coarsening of the CZTS nanocrystals reduces the driving force for abnormal crystal growth. Increasing the sulfur pressure by an order of magnitude to 500 Torr accelerates both normal and abnormal crystal growth though sufficient acceleration of the former eventually reduces the latter by reducing the driving force for abnormal grain growth. For example, at high temperatures (700-800 °C) and sulfur pressures (500 Torr) normal grains quickly grow to ~500 nm which significantly reduces abnormal grain growth. The use of soda lime glass as the substrate, instead of quartz, accelerates normal grain growth. Normal grains grow to ~500 nm at lower temperatures and sulfur pressures (*i.e.*, 600 °C and 50 Torr) than those required to grow the same size grains on quartz (700 °C and 500 Torr). Moreover, carbon is removed by volatilization from films where normal crystal growth is fast.

There are significant differences in the chemistry and in the thermodynamics involved during selenization and sulfidation of CZTS colloidal nanocrystal coatings to form CZTSSe or CZTS thin films, respectively. To understand these differences, the roles of vapor pressure, annealing temperature, and heating rate in the formation of different microstructures of CZTSSe films were investigated. Selenization produced a bi-

layer microstructure where a large CZTSSe-crystal layer grew on top of a nanocrystalline carbon-rich bottom layer. Differences in the chemistry of carbon and selenium and that of carbon and sulfur account for this segregation of carbon during selenization. For example, CSe_2 and CS_2, both volatile species, may form as a result of chalcogen interactions with carbon during annealing. Unlike CS_2, however, CSe_2 may readily polymerize at room temperature and one atmosphere. Carbon segregation may be occurring only during selenization due to the formation of a Cu-Se polymer [*i.e.*, (CSe_{2-x})] within the nanocrystal film. The (CSe_{2-x}) inhibits sintering of nanocrystals in the bottom layer. Additionally, a fast heating rate results in temperature variations that lead to transient condensation of selenium on the film. This is observed only during selenization because the equilibrium vapor pressure of selenium is lower than that of sulfur. The presence of liquid selenium during sintering accelerates coarsening and densification of the normal crystal layer (no abnormal crystal layer) by liquid phase sintering. Carbon segregation does not occur where liquid selenium was present.

Table of Contents

List of Tables

List of Figures

CHAPTER 1

Introduction

This thesis is concerned with fabrication of a candidate light absorbing material for thin film photovoltaics. The material is copper zinc tin sulfide, or Cu_2ZnSnS_4, which is most commonly referred to using the acronym CZTS. In this chapter, we will summarize the market position, prospects, and technology of thin film photovoltaics and provide motivation for CZTS.

1.1 Summary of The Photovoltaic Technology in the Market

The global consumption of power in 2013 was approximately 18.6 TW and that figure is projected to rise to 27.4 TW by 2040.[1] The majority of that demand is satisfied by methods that release greenhouse gases such as CO_2 into the atmosphere, such as coal, natural gas, and liquid fuels. The dangerous outcomes of continued global warming, such as acidification of the oceans and changes in global atmospheric circulation patterns, have been outlined in recent reports from the Intergovernmental Panel on Climate Change.[2,3] The global challenge is to provide 30 TW via carbon-free renewable energy resources by the mid-21st century.[4,5] A combination of renewable energy resources, such as solar, wind, hydroelectric, geothermal, and solar fuels, should be pursued given the practical realities of different geographical conditions. Of these, power from the sun has the greatest potential due to the 600 TW of feasibly extractable power reaching the planet.[6] Since 1975, the global photovoltaic (re: solar cell) capacity has doubled approximately every 2.45 years. If this "Moore's law for solar cells" trend continues, the global terawatt challenge may be met.[7] Continuing this trend requires constant innovation, favorable governmental policies, reduction in solar cell costs, and solar cell cells made from abundant, in-expensive materials.

The commercial photovoltaic market technologies may be divided into two broad categories: crystalline silicon (c-Si) and inorganic thin film based solar cells. In 2010, c-Si and thin films represented 85-90% and 10-15% of the global annual photovoltaic market, respectively.[8–10] In the c-Si category, the market players are single crystal silicon (sc-Si) and microcrystalline silicon (mc-Si). The dominant materials in the thin film category are amorphous silicon (a-Si), cadmium telluride (CdTe) and copper indium (gallium) sulfide/selenide (CIS/CIGS). There are also emerging technologies that include dye-sensitized solar cells,[11] concentrating photovoltaics, and organic solar cells. Future market prospects include alternative thin film materials, such as CZTS, as well as novel technologies such quantum dot solar cells and perovskite materials.[12]

Although the current market share of thin film photovoltaics is small, it is poised to grow due to a number of important advantages over c-Si. Thin film materials absorb the solar spectrum more efficiently than silicon: the CdTe or CIGS layer is 1-3 um thick, whereas silicon wafers are 100-300 um thick.[5,13] As a consequence, thin film solar cell modules weigh less, which makes this technology more attractive for building-integrated photovoltaics (BIPV) than c-Si and can translate to reduced installation costs.[14] Thin film materials also have great potential for use with flexible substrates in large part because of the ability to use thin layers. With CIGS, band gap and band-edge engineering is another significant advantage as it lends flexibility in optimizing light absorption, flexibility in choosing junction/contract materials, the ability to optimize device performances with strategies such as graded heterojunctions,[15] and the potential for reaching beyond the single-junction Schockley-Quiesser limit by manipulation of the composition.[16,17] Another critical advantage that makes processing and optimization less expensive is that thin film materials are more defect-tolerant than c-Si.[18–20]

Raw material abundance as well as cost of extraction and purification are significant future challenges to the current state-of-the-art commercial solar cell technologies. The relative abundance of elements in Earth's crust is shown in Figure 1a and raw material cost for several solar cell materials is shown in Figure 1b. Although silicon is one of the most abundant elements on Earth, there are significant costs

associated with its processing due the high energy input required to produce metallurgical grade silicon from silica (SiO_2).[5,21] Silicon solar cells require thick (~100 μm) wafers to a absorb significant fraction of sunlight and the wafers must be highly pure to reduce loss of the photogenerated current through the thick wafer. Thus, an abundant element becomes an expensive solar cell material. The material cost of a-Si, as shown in Figure 1b, is very low because it can be deposited by vacuum deposition techniques rather than purification of SiO_2. The drawback of a-Si is low solar cell efficiencies, in part due to light-degradation effects.[22] In the case of CdTe, while it has seen tremendous initial market growth due to efforts of a single company, First Solar, analyses suggest that the global electricity production with CdTe is limited to below TW levels[21,23] due to limited availability of tellurium, one of the rarest elements on Earth. Additionally, cadmium is a toxic material which further adds additional layers of cost for safe processing and compliance with regulations. As a result, the material cost of CdTe, per Watt, is greater than that of c-Si.[21] CIGS realizes significant cost savings by having more abundant, less expensive, elements such as copper, gallium, and sulfur. There is fierce competition for indium, however, in the form of tin-doped indium oxide for the transparent conductive surfaces in touch screen devices. This makes the cost of CIGS vulnerable to the volatile price of indium due to rapidly increasing demand for the relatively rare material. These concerns motivate the investigation of alternative, earth-abundant, thin film solar cells materials.

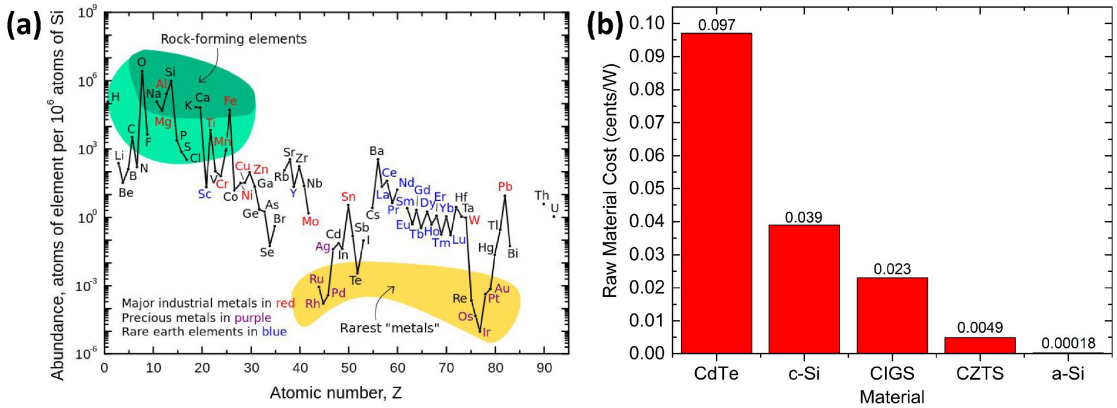

Figure 1.1 (a) Relative abundance of elements in the Earth's crust.[24,25] (b) Minimum cost of raw material extraction for select solar cell material compounds.[21] These costs do not reflect to installed costs of the photovoltaic system.

1.2 Motivation for Cu_2ZnZnS_4 (CZTS)

CZTS is a promising alternative thin film material that is based on the chalcopyrite structure of CIS but with the substitution of In for Zn and Sn, which are both abundant and environmentally benign elements. Figure 1b shows that the raw material cost of CZTS is almost a fifth of the raw cost of CIGS because the constituent elements are abundant and they are major industrial materials, as a result of which the the extraction technology for each is mature. Additionally, the extraction of raw materials for CZTS is independent of the mining demand of other materials. In contrast, for CdTe and CIGS, Cd and In are impurities in Zn ore while Te is an impurity in Cu ore.[20] CZTS is a p-type material with a direct band gap of 1.5 eV, translating to a ~30% theoretical single-junction solar cell efficiency limit,[16] and an absorption coefficient, α, that allows it to efficiently absorb light with energy greater than the bandgap ($\alpha > 10^4$ cm^{-1}).[26–28] Replacing a fraction of the sulfur with selenium allows the band gap to be tuned to as low as 1.0 eV with $Cu_2ZnSnSe_4$ and the combination of S and Se may reduce the concentration of electron recombination centers.[29] Researchers have taken advantage of lessons learned with CIGS, such as the device structure, to rapidly accelerate the success of CZTS.

Since the first report of a photovoltaic effect of CZTS appeared in 1988, the reported power conversion efficiencies (PCE) have risen to over almost 13% in just over two decades.[30,31] CZTS was pioneered with vacuum deposition techniques, such as evaporation and sputtering, but solution-based approaches have been leading the way in record efficiencies in the last few years. In Chapter 2, we will discuss the various CZTS film deposition techniques.

1.3 Thesis Organization

Meeting the terawatt challenge with CZTS-based solar cells will require low-cost manufacturing methods. In Chapter 2, we will describe common CZTS thin film deposition techniques, which may be divided into the categories of vacuum-based and solution-based. While vacuum-based methods rely on mature technologies and high-

purity, solution-based methods may offer reduced costs via high-throughput and low-material waste.

In Chapter 3, we will describe a colloidal CZTS nanocrystal synthesis technique in which the average nanocrystal size can be tuned with one simple variable (solution temperature). The reaction and growth happen within a few minutes. At 150 ^{o}C, 2 nm CZTS nanocrystals are synthesized which are smaller than the Bohr radius and have a band-gap of 1.7 eV due to quantum confinement. The nanocrystal size can be increased to an average size of ~40 nm by increasing the reaction temperature to 340 ^{o}C, without increasing growth times. Larger nanocrystals are shown to produce crack-free films via inexpensive deposition techniques, such as drop casting. The application of this CZTS nanocrystal synthesis and film deposition route is demonstrated with a CZTS thin film solar cell from sulfur-annealed CZTS nanocrystals. This chapter has been published in the RSC Journal of Materials Chemistry A: B. D. Chernomordik, A. E. Béland, N. D. Trejo, A. A. Gunawan, D. D. Deng, K. A. Mkhoyan, and E. S. Aydil, "Rapid facile synthesis of Cu_2ZnSnS_4 nanocrystals," *J. Mater. Chem. A.*, DOI: 10.1039/c4ta01658k, 2014.

Realization of inexpensive and high-efficiency solar cells requires understanding the fundamental factors that affect microstructure development in CZTS films during annealing. There have been only a few investigations of sulfidation of solution-based films to make CZTS thin films due to the high vapor pressure of sulfur, which makes it difficult to maintain a controlled sulfur atmosphere in open systems. Using a closed annealing system, the effects of annealing temperature, annealing time, sulfur pressure, and alkali metals (via soda lime glass) on crystal growth in annealed CZTS nanocrystal films will be described in Chapter 4. The microstructure was found to be the result of competition between abnormal and normal crystal growth, the relatives rates of which may be tuned by manipulation of process variables. At low sulfur pressures, abnormal crystal growth results in scattered growth of large micron-scale single-crystals of CZTS on top of a nanocrystalline floor layer. Normal crystal growth is accelerated at the expense of abnormal crystals by increasing the sulfur pressure during annealing or by

introducing alkali metals from soda lime glass. It was also found that sulfidation results in removal of carbon (via formation of volatile species). This chapter has been published in ACS Chemistry of Materials: B. D. Chernomordik, A. E. Béland, D. D. Deng, L. F. Francis, and E. S. Aydil, "Microstructure evolution and crystal growth in Cu_2ZnSnS_4 thin films formed by annealing colloidal nanocrystal coatings," *Chem. Mater.*, DOI: 10.1021/cm500791a, 2014."

Crystal growth in in nanocrystal films annealed with selenium atmosphere to make $Cu_2ZnSn(S_xSe_{1-x})_4$ (CZTSSe) thin films is discussed in Chapter 5. One issue in CZTSSe films from solution-based methods is the development of a nanocrystalline layer, which is also carbon-rich, in between the back contact and a layer of large CZTSSe grains. Investigations regarding the formation of this nanocrystalline layer have been limited. In this chapter, we elucidate the chemistry which may be responsible for the formation of the carbon-rich fine-grained layer. It is further shown that the presence of liquid selenium during the initial sintering stage accelerates normal growth. This results in formation of up to 1 μm crystals without a segregated fine-grained and carbon-rich layer. This chapter will be submitted for publication with authors B. D. Chernomordik, P. M. Ketkar, A. K. Hunter, A. E. Béland, and E. S. Aydil as "Microstructure evolution during selenization of Cu_2ZnSnS_4 colloidal nanocrystal coatings."

Several sets of preliminary data are presented in Appendix A. In particular, grain growth enhancement with gas phase delivery of sodium is a promising direction for investigation as another tuning parameter to systematically and reproducibly influence thin film microstructure without relying on impurity diffusion from the substrate. Additionally, we have found that significant normal crystal coarsening occurs during annealing without loading sulfur or selenium into the sealed annealing ampule. Moreover, no evidence of binary or ternary decomposition species were detected within the limits of XRD and Raman despite the lack of added sulfur. Instead, between 0.0014% and 0.015% of sulfur loss from the film is enough to establish a sulfur atmosphere that can stabilize the CZTS film against further decomposition.

1.4 References

1. *International Energy Outlook 2013*, U.S. Energy Information Administration Energy, U.S. Department of Energy, Washington, DC, 2013.
2. S. Solomon, D. Qin, M. Manning, Z. Chen, M. Marquis, K. B. Averyt, M. Tignor, and H. L. Miller, *Fourth Assessment Report of the Intergovernmental Panel on Climate Change*, Cambridge University Press, Cambridge, UK, 2007.
3. *Fifth Assessment Report of the Intergovernmental Panel on Climate Change*, Cambridge University Press, Cambridge, UK, 2014.
4. M. I. Hoffert, K. Caldeira, A. K. Jain, E. F. Haites, L. D. D. Harvey, S. D. Potter, M. E. Schlesinger, S. H. Schneider, R. G. Watts, T. M. L. Wigley, and D. J. Wuebbles, *Nature*, 1998, **395**, 881.
5. C. A. Wolden, J. Kurtin, J. B. Baxter, I. Repins, S. E. Shaheen, J. T. Torvik, A. A. Rockett, V. M. Fthenakis, and E. S. Aydil, *J. Vac. Sci. Technol. A*, 2011, **29**, 030801.
6. N. S. Lewis, *MRS Bull.*, 2007, **32**, 808.
7. D. J. Norris and E. S. Aydil, *Science*, 2012, **338**, 625–626.
8. S. Abermann, *Sol. Energy*, 2013, **94**, 37–70.
9. A. Jaeger-Waldau, *Joint Research Centre, PV Status Report 2010, Office for Official Publications of the European Union*, Brussels, 2010.
10. *International Energy Outlook 2010*, U.S. Energy Information Administration, U.S. Department of Energy, Washington, DC, 2010.
11. A. Hagfeldt, G. Boschloo, L. Sun, L. Kloo, and H. Pettersson, *Chem. Rev.*, 2010, **110**, 6595–6663.
12. H. J. Snaith, *J. Phys. Chem. Lett.*, 2013, **4**, 3623–3630.
13. F. Dross, K. Baert, T. Bearda, J. Deckers, V. Depauw, O. El Daif, I. Gordon, A. Gougam, J. Govaerts, S. Granata, R. Labie, X. Loozen, R. Martini, A. Masolin, B.

O'Sullivan, Y. Qiu, J. Vaes, D. Van Gestel, J. Van Hoeymissen, A. Vanleenhove, K. Van Nieuwenhuysen, S. Venkatachalam, M. Meuris, and J. Poortmans, *Prog. Photovolt: Res. Appl.*, 2012, **20**, 770–784.

14. A. Henemann, *Renew. Energy Focus*, 2008, **9**, 14–19.

15. T. Dullweber, G. Hanna, U. Rau, and H. W. Schock, *Sol. Energ. Mat. Sol. C.*, 2001, **67**, 145–150.

16. W. Shockley and H. J. Queisser, *J. Appl. Phys.*, 1961, **32**, 510–519.

17. K. Nagaich, S. Campbell, and E. Aydil, *Photovolt. Spec. Conf. (PVSC), 2011 37th IEEE*, 2011, 425–429.

18. S. Delbos, *EPJ Photovoltaics*, 2012, **3**, 35004.

19. S. Siebentritt, M. Igalson, C. Persson, and S. Lany, *Prog. Photovolt: Res. Appl.*, 2010, **18**, 390–410.

20. S. Abermann, *Sol. Energy*, 2013, **94**, 37–70.

21. C. Wadia, A. P. Alivisatos, and D. M. Kammen, *Environ. Sci. Technol.*, 2009, **43**, 2072–2077.

22. D. L. Staebler and C. R. Wronski, *Appl. Phys. Lett.*, 1977, **31**, 292–294.

23. B. A. Andersson, *Prog. Photovolt: Res. Appl.*, 2000, **8**, 61–76.

24. G. B. Haxel, J. B. Hedrick, G. J. Orris, P. H. Stauffer, and H. W. I. Hendley, *Fact Sheet 087-02: Rare Earth Elements-Critical Resources for High Technology*, U.S. Geological Survey, 2002.

25. *Abundance of elements in Earth's crust*, Wikipedia, 2014.

26. H. Katagiri, K. Jimbo, S. Yamada, T. Kamimura, W. S. Maw, T. Fukano, T. Ito, and T. Motohiro, *Appl. Phys. Express*, 2008, **1**, 041201.

27. S. Chen, X. G. Gong, A. Walsh, and S.-H. Wei, *Appl. Phys. Lett.*, 2009, **94**, 041903.

28. K. Timmo, M. Altosaar, J. Raudoja, K. Muska, M. Pilvet, M. Kauk, T. Varema, M. Danilson, O. Volobujeva, and E. Mellikov, *Sol. Energ. Mat. Sol. C.*, 2010, **94**, 1889–1892.

29. S. Chen, A. Walsh, X.-G. Gong, and S.-H. Wei, *Adv. Mater.*, 2013, **25**, 1522–1539.

30. W. Wang, M. T. Winkler, O. Gunawan, T. Gokmen, T. K. Todorov, Y. Zhu, and D. B. Mitzi, *Adv. Energy Mater.*, 2013, 10.1002/aenm.201301465.

31. K. Ito and T. Nakazawa, *Jpn. J. Appl. Phys.*, 1988, **27**, 2094–2097.

CHAPTER 2

CZTS Thin Film Deposition Techniques

In this chapter, we will discuss different methods for depositing thin films of CZTS. This chapter is divided into methods based on vacuum deposition and those based on solution deposition. It is worth noting that the CZTS-layer deposition method is one of many variables that contribute to the final device performance. The typical CZTS solar cell architecture is the same as used for CIGS solar cells: (1) molybdenum-coated soda lime glass as the back contact, (2) 1-3 μm of CZTS as the absorber layer, (3) thin (~50 nm) CdS buffer layer, (4) ~200 nm of intrinsic ZnO window layer, (5) tin-doped indium oxide as the transparent conductive layer, and (5) Ni/Al contact grid.[1] Even unreported factors, such as the quality of the deionized water used in chemical bath deposition of the CdS layer, may have significant effects on device performance.[2] Some groups introduce additional sodium doping, in addition to that diffusing from the soda lime glass, by introducing thin layers of Na_2S or NaF, for example, before depositing CZTS. One of the advantages of the presence of Na is that it leads to larger final grain sizes of CZTS during thermal treatment. Additionally, some efficiencies are reported with devices that include a MgF_2 anti-reflecting coating.

2.1 Vacuum Depositions

Vacuum deposition of thin film materials is a mature technology. Methods such as evaporation and sputtering allow for high purity, fine control of film compositions, as well as epitaxial deposition. The disadvantages of vacuum approaches are that they rely on slow deposition rates (low throughput) and low material utilization (high material waste). In this section, we will review the two most common vacuum-based techniques for depositing CZTS thin films: evaporation and sputtering. This is a non-exhaustive list

of publications or depositions methods. Methods such as pulsed laser deposition,[3] chemical vapor deposition,[4] and atomic layer deposition[5] are not reviewed here.

2.1.1 Evaporation

Deposition of CZTS thin films by evaporation initially involved deposition of Cu/Sn/Zn metal stacks followed by sulfidation in a H_2S and N_2 atmosphere at 500 ^oC.[6] Due to the volatility of zinc, however, later reports replaced Zn with ZnS to improve control over final stoichiometry.[7] Evaporation of multiple periods of Cu/SnS_2/ZnS layers, followed by sulfidation, led to smoother morphologies, due to better intermixing and increased initial sulfur content.[8] Later, co-evaporation was explored by using Cu, Zn, Sn, and S sources and it was shown that grain size increases with increasing substrate temperature between 400 and 600 ^oC.[9] Rapid deposition of a Cu-rich film by co-evaporation of ZnS, Cu, Sn, and S sources with the substrate at 550 ^oC was found to form CZTS with a CuS phase, which could be removed using a subsequent etch with KCN,[10] which was shown to preferably etch CuS, as well as SnS to a lesser extent.[11] After etching, the devices had a PCE of up to 4.1%.[10] Another successful strategy involved co-evaporation from Cu, Zn, Sn, and S sources but at low substrate temperatures (110 ^oC) followed by a quick anneal at 540 ^oC in an S atmosphere.[12] The low substrate temperatures and short annealing time helped to limit loss of material from re-evaporation. The latter method produced 6.8% efficient solar cells. The same group later increased the efficiency to 8.4% after increasing the deposition and annealing temperatures to 150 and 570 ^oC, respectively. This is currently the record efficiency for a sulfide-only CZTS device. The current record efficiency for a vacuum-deposited CZTS-based device is 9.15%, where CZTSe device deposited by co-evaporation of elemental sources, wherein Se was used instead of S. A 15 nm NaF layer was deposited before CZTS in the latter study, and a MgF_2 anti-reflective coating was used in each of the last three studies discussed above.

2.1.2 Sputtering

The first report of a CZTS device, which consisted of a CZTS-cadmium oxide heterojunction, employed argon beam sputtering from a target containing a stoichiometric

mixture of Cu-Zn-Sn-S. Later, CZTS thin films were fabricated by sputtering Cu/Zn/Sn stacks followed annealing with an S flux.[13] Adhesion to the substrate was improved by increasing the substrate temperature during sputtering. Subsequent annealing temperatures below 400 ^{o}C produced stoichiometric films, while annealing at 450 ^{o}C led to Zn-loss due to the volatility of Zn. Katagiri et. al have reported the highest efficiency CZTS solar cells via a sputtering approach. Co-sputtering of Cu, SnS, and ZnS sources followed by sulfidation in a dilute H_2S atmosphere produced 5.74%.[14] Later this was updated to 6.77% with DI water treatment, which was suggested to remove oxide phases, prior to CdS deposition.[15] Katagiri also explored the dependence of solar cell efficiency on variation in the Cu:Zn:Sn ratio and found that the best devices were Cu-poor and Zn-rich: specifically, Cu/(Sn+Zn)≈0.9 and Zn/Sn≈1.2.[16]

The ordering of metal stacking prior to sulfidation affects the quality of the final film (*e.g.*, grain size and presence or absence of impurities). In particular, Fernandes et al. found that having Cu on top reduced the loss of Zn and Sn during processing and also led to large crystallite sizes.[17] Yoo et al. further showed that poor crystallinity is observed if the Zn layer is sandwiched in between the Cu and Sn layers because the formation of Cu_2SnS_3 is a necessary intermediate step to forming Cu_2ZnSnS_4.[18] Additionally, the Cu layer should not be at the bottom to avoid the formation of voids at the back contact due to the fast out-diffusion of Cu toward the top. Another strategy is co-sputtering of a mixed layer of Cu-Zn-Sn alloys. This can be accomplished by, for example, sputtering from a single target with elemental segments[19] or from separate targets containing Cu+Zn and Cu+Sn.[20] In the former study, it was found that a short (7 min) anneal at 1.5 atm of sulfur led to better adhesion and an increase in crystals size compared to a long (40 min) anneal with 0.1 atm of sulfur. In the other study, it was shown that alkali metal impurities may be introduced by vapor phase. Grain size was improved with the introduction of Na or K but not Ca.[20]

2.2 Solution-Based Methods

The advantages of solution-based thin film deposition approaches may be: reduced capital investment, the potential for reduced operating expenses, higher throughput (high deposition rates), higher material utilization (lower material waste), and

material uniformity over large areas. It is common that some portions of the deposition stages can be done at atmospheric conditions, which also reduce operating expenses. Furthermore, it is possible to deposit other layers of the solar cell device via solution approaches, such CdS by chemical bath deposition and ZnO via colloidal nanoparticles, to avoid expensive vacuum equipment in commercial applications. There are many methods and variations that have been demonstrated to be effective for CZTS. In this section, we will attempt to categorize the methods and variations in the following way: molecular precursor solutions (including hybrid inks and slurries), colloidal nanoparticle inks, and electrodeposition. It should be noted that the division between true precursor solution and colloidal nanoparticle methods may be blurred in the case where nanoparticles may nucleate in the process deposition. We will include the latter case in the molecular precursor solution category. The colloidal nanoparticle ink method will be strictly defined as one where the colloidal nanoparticles are intentionally formed prior to deposition onto a substrate.

2.2.1 Molecular Precursor Solutions

The molecular precursor solution approach has also been called "direct solution coating." A solution of precursor molecules, or a hybrid slurry of particles and molecular precursors, is coated onto the substrate followed by thermal processing to yield the desired kesterite-phase thin film. The coating may be formed by any number of procedures that include knife blading, drop casting, dip coating, and spray coating.

One way to summarize the molecular precursor solution approach is to separate the method into its parts and steps: solvent, metal and chalcogen compounds, additional binders, coating, drying, and crystallization or phase formation step. The solvent is chosen such that it can dissolve the Cu, Zn, Sn, and chalcogen compounds with minimal impurities. The highest efficiency CZTS solar cells have been made by the IBM group using hydrazine (N_2H_4) as the solvent.[21,22] Some advantages of hydrazine are that: it is free of organics and oxygen; it effectively dissolves metal chalcogenides and elemental chalcogenides; it decomposes cleanly into N_2, NH_3, and H_2; and it prevents metal oxidation due to being a strong reducing agent.[23] The disadvantage of hydrazine is that it is highly toxic and explosive, requiring that all processing occurs in an inert atmosphere.

Moreover, restrictions on the transportation of hydrazine between countries may make global implementation difficult. A number of organic solvents are viable alternatives, which include alcohols,[24] ethylene glycol,[25] 2-methoxyethanol,[26–28] pyridine,[29] N,N,-dimethylformamide (DMF),[30] and dimethyl sulfoxide (DMSO),[31,32] Among this list, DMSO has yielded the highest efficiency device at 8%.[32,33] DMSO is a versatile solvent that can bond with a metal through the oxygen or the sulfur to form metal-organic complexes and it is capable of dissolving a wide range of organic and inorganic substances while being miscible with many organic solvents. Thiourea is typically added as the sulfur source to form the metal chalcogenides.

Sources of the metals can be chloride,[31] nitrate, acetate,[27] or iodide salts.[29] The ratios of the metal salts are adjusted to yield the desired final stoichiometry, with adjustment for possible losses of metals (Zn or Sn) to vapor in open systems. The chalcogen (S or Se) is also introduced into the solution in the form of elemental S or Se,[34] thiourea,[32,35] or thioacetamide.[25,29] Elemental chalcogens dissolve poorly in most of the solvents except hydrazine[34] and DMF.[30] Additional solutes may be added to act as complexing agent, binder, surfactants, pH stabilizers, or antioxidants. For example, monoethanolamine[27] is added to aid in complexing with and stabilizing the metal compounds. Ethyl cellulose may be added as a binder to thicken the solution for knife-blading and to help reduce cracking. The use of some additional solutes, such as 1,2-propanediol or ethyl cellulose with alcohol solutions, may cause carbon to remain in the film through annealing, resulting in a carbon-rich bottom layer at the interface with the molybdenum back contact.[24,36] Notably, metal oxide powders have also been successfully used wherein the powders were coordinated with butyldithiocarbamic acid as well as thioglycolic acid in ethanol and CS_2 acted as the source of sulfur. In the latter study, the CZTS phase was formed after sintering at only 320 ^{o}C followed by selenization at higher temperatures.[37] (This study also observed a bottom carbon-rich layer). With hydrazine, the leading devices were made by dissolving Cu and Sn chalcogenides (*e.g.*, Cu_2S and SnS) in hydrazine but the low solubility of Zn(S,Se) resulted in a slurry containing nanoparticles of Zn(S,Se)(N_2H_4).[38] More recently, the same group modified this approach to make a pure-solution in hydrazine by dissolving elemental zinc in hydrazine instead of ZnSe.[22,39] Hydrazinocarboxylic acid ($NH_2NHCOOH$) has also been used in previous

reports to dissolve zinc in hydrazine.[34] Additionally, sodium-containing species such as Na_2S or NaOH may be dispersed in the precursor solution to enhance grain growth during the subsequent annealing.[40]

These solutions are then deposited onto substrates, dried on a hot plate, and then annealed. The drying temperature (200-350 ^oC) is maximized to eliminate the solvent and limit other impurities without causing oxidation of the precursor film or the molybdenum layer. Annealing in an inert atmosphere allows the drying to occur at higher temperatures (580 ^oC), by which point crystallization and grain growth also occur.[31] Multiple thin coatings, with the drying step in between, are used to build up a thick layer by forming successive layers that are each below the critical cracking thickness. Alternatively, the film may be deposited via spray pyrolysis. With spray pyrolysis, the precursor solution is sprayed onto a heated substrate. The deposition, drying, and phase formation take place upon contact with the hot substrate. A subsequent annealing step to encourage grain growth is sometimes also performed. The solutions are similar to those described above. For example, multiple groups sprayed a solution of metal chlorides and thiourea in water onto substrates at 280-360 ^oC.[41,42]

The final step is annealing and crystal growth in a chalcogen atmosphere (S, H_2S, or Se).[24,26,27,31,32,34,43] The presence of a chalcogen vapor prevents decomposition of the kesterite phase through the sublimation of sulfur and subsequent formation of volatile SnS(Se).[44] The chalcogen atmosphere also encourages grain growth. This annealing step can be done in an open or closed system. Open systems include two-zone tube furnaces with an inert carrier gas.[24,26] Alternatively, the film and elemental selenium are placed in a graphite box with a hole. The selenium evaporates and the vapor escapes the box, but the duration of the annealing is kept shorter than the time required for all of the selenium to escape.[31,33] In the former method, it is difficult to achieve high overpressures of volatile species and in the latter method it is difficult to predict the chalcogen pressure as a function of temperature and the procedure may be susceptible to irreproducibility. In a closed system, such as a sealed quartz ampule,[20,45] desired chalcogen pressure may be achieved and an overpressure of volatile species is sustainable.

2.2.2 Colloidal Nanoparticle Inks

An attractive solution-based approach for commercially scalable CZTS thin film deposition is through colloidal nanoparticle inks. Indeed, this approach has been adopted by companies such as NanoSolar with CIGS and has been demonstrated to be commercially viable for CZTS by Solexant.[46] The advantage of this approach is that the desired phase(s) may be synthesized separately from the deposition and grain growth processes. This provides some freedom in the chemistry and conditions used to obtain the desired inorganic phases, without worrying about the effect of the latter chemistry on the substrate material(s). For example, this opens opportunities to investigate temperature-sensitive flexible substrates. Synthesis in liquid allows for higher atom diffusivities in order to overcome activation barriers to reaching the thermodynamically stable phase. In contrast, atom diffusion in the solid phase is more restricted and there is a higher risk of forming undesired decomposition species due to compositional non-uniformities. Additionally, issues such as the volatility of Zn are avoided by first making the desired CZTS phase in solution. Uniformity of composition across the entire final film is indeed a significant advantage of the nanoparticle ink method. Furthermore, the nanoparticle route may offer more flexibility in controlling the presence of additives and impurities than the precursor solution approach. This is because the removal ("washing") and/or exchange of ligands and other compounds may be performed prior to and after deposition of the CZTS-phase nanocrystals but before annealing (*i.e.*, the CZTS phase is already formed prior to annealing and other stabilizing compounds are no longer needed).

First, a colloid of the desired nanocrystal phases is synthesized. This may be CZTS, CZTSe, or a mixture of binary and/or ternary phases. Appropriate washing procedures are employed to remove unwanted impurity compounds (*e.g.*, unreacted organics) and solution-phase ligand exchange may be performed as well. The colloid is then deposited onto the substrate by similar methods as described previously for precursor solutions, such as drop casting and doctor/knife blading. This may involve deposition of multiple layers to obtain the desired thickness. In between each layer deposition, ligands may be removed to reduce dissolution of preceding layers and to reduce the concentration of organics in the final film. Lastly, the nanocrystal film is annealed at 500-600 ^{o}C in an

inert or chalcogen (S or Se) atmosphere. Annealing is done to convert the binary/ternary phases into quarternary CZT(S,Se) (if applicable), exchange sulfur for selenium in the kesterite lattice (if applicable), and encourage crystal growth.

The synthesis routes may generally be categorized as "hot-injection" or "heat-up." The heat-up method refers to gradual heating of all precursors, which may be similar to those used in the hot-injection synthesis.[47] Within the category of hot-injection, two types of syntheses should be distinguished: one that is commonly discussed in terms of classical nucleation theory where oversaturation of monomer leads to particle nucleation, and one wherein nucleation occurs upon thermolysis of precursor molecules. The majority of CZTS nanocrystal reports employ the former synthesis type. The metal precursor salts, which may be chlorides, acetates, or acetylacetonates, for example, are dissolved in a coordinating solvent which may be oleylamine, [48]oleic acid,[49] or trioctylphosphine oxide.[50] The composition of the final film is controlled through mass ratios of the metal precursors. The sulfur source is typically elemental sulfur complexed with oleylamine,[51] but other sources such as dodecanethiol may be used as well.[52] The metal precursors and sulfur source are then swiftly injected into a flask containing a coordinating solvent such as oleylamine or trioctylphosphine oxide. To make CZTSe, the metal precursors are the same but the selenium is complexed with trioctylphosphine,[53] tributylphosphine, or dodecanethiol together with oleylamine.[54] In the thermolysis approach, metal alkyl thiocarbmate complexes, such as metal diethyldithiocarbamates, may be used as sources of both the metal and the sulfur. In this synthesis route, the thiocarbamate precursors may be coordinated with oleic acid and then injected into hot oleylamine to induce decomposition of the precursors followed by nucleation and growth of CZTS.[49] (This is the approach discussed in Chapter 3.) After reaction and growth, the colloid is then washed by precipitation with an antisolvent, such as ethanol, centrifuged, and redispersed in a solvent such as toluene (repeated multiple times). The colloid may be composed of CZTS(Se) nanocrystals or a mixture of copper tin sulfide phases, ZnS, SnS, and CuS.[55]

After deposition, the films are then annealed. The highest efficiency devices, so far, from solution-based approaches have been those where sulfide nanocrystals are annealed in a selenium atmosphere to make $Cu_2ZnSn(S_xSe_{1-x})_4$ (CZTSSe) thin film.[55,56]

As discussed with molecular precursor solution routes, the annealing may be done in open or closed systems. In one method, for example, the nanocrystal film is loaded into a graphite box with selenium pellets. The box is quickly inserted into a preheated tube furnace at 500-560 ^{o}C for <40 minutes. The selenium quickly evaporates and escapes through a pinhole in the graphite box as an inert carrier gas is flown over the outside of the box. The vapor pressure inside the box is unknown but is likely near the saturated vapor pressure (~50 Torr) until the selenium is depleted, although a partial pressure gradient may exist. The resulting films typically have a bilayer structure, wherein a large grain CZTSSe layer sits atop a nanocrystalline CZTSSe layer which is also carbon-rich. The role of the carbon-rich layer is not well-understood, but it has been suggested that its thickness should be minimized to limit series resistance.[26,57,58] The entrapment of carbon is often taken for granted as the expected outcome, perhaps due to the quick formation of a "capping" large grain layer on the top,[59,60] however carbon is effectively removed via vapor during sulfidation.[45] In Chapter 5, we will discuss in more detail the possible causes for the formation of the carbon-rich layer and alternative annealing strategies to avoid this layer during annealing. Annealing in a closed system, as will be discussed in Chapter 5, offers advantages in controlling the selenium overpressure independently of temperature and limits loss of volatile species during long anneals.

Other annealing strategies include selenization of selenide (CZTSe) nanocrystals and sulfidation of sulfide (CZTS) nanocrystals. There are few reports investigating these strategies. Generally, it appears that significantly smaller grains are obtained when selenide nanocrystals are annealed with selenium or when sulfide nanocrystals are annealed with sulfur.[61–63] Systematic sulfidation of CZTS nanocrystals in a closed system is discussed in Chapter 4, and the study been published recently. We described the crystal growth in terms of a competition of abnormal crystal growth (large crystal on the surface) and normal crystal growth (nanocrystals in the bottom layer). During sulfidation, large crystals grow on the surface, similarly to the case of selenium, but the crystals do not form a continuous layer. The normal nanocrystals can be encouraged to grow, at the expense of the abnormal crystals, by increasing the sulfur pressure (e.g., 500 Torr versus 50 Torr) at elevated temperatures (e.g., 700 ^{o}C). Alternatively, alkali metal impurities from soda lime glass also accelerate normal crystal growth. Furthermore, carbon is

effectively volatilized during sulfidation without having performed any prior ligand exchange procedures. In the case of selenization of CZTS nanocrystals, it appears that the dominant growth mechanism is that of abnormal crystals while normal crystal growth is inhibited. This is discussed further in Chapter 5.

2.2.3 Electrodeposition

Electrodeposition is a solution-based alternative to vacuum deposition for depositing metal stacks of Zn, Sn, and Cu. For example, Jeon et al. used aqueous sulfate and chloride salts and trisodium citrate as a complexing agent to deposit films of Cu-Zn-Sn followed by cleaning with solvents and annealing at 400-600 ^{o}C in a tube furnace with vapor selenium carried by Ar. They obtained 8% (active area) solar cells with annealing at 550 ^{o}C.[64] Ahmed et al. also recently published a 7.3% solar cell after sulfidation of the metal stack to form large-grain CZTS thin films.[65]

2.3 References

1. J. J. Scragg, Copper Zinc Tin Sulfide Thin Films for Photovoltaics: Synthesis and Characterisation by Electrochemical Methods, Springer-Verlag, Berlin/Heidelberg, 2011.
2. V. A. Akhavan, Ph.D. Thesis, University of Texas at Austin, 2011.
3. K. Moriya, K. Tanaka, and H. Uchiki, Jpn. J. Appl. Phys., 2007, **46**, 5780–5781.
4. K. Ramasamy, M. A. Malik, and P. O'Brien, Chem. Sci., 2011, **2**, 1170–1172.
5. E. Thimsen, S. C. Riha, S. V Baryshev, A. B. F. Martinson, J. W. Elam, and M. J. Pellin, Chem. Mater., 2012, **24**, 3188–3196.
6. H. Katagiri, N. Sasaguchi, S. Hando, S. Hoshino, J. Ohashi, and T. Yokota, Sol. Energ. Mat. Sol. C., 1997, **49**, 407–414.
7. H. Katagiri, K. Saitoh, T. Washio, H. Shinohara, T. Kurumadani, and S. Miyajima, Sol. Energ. Mat. Sol. C., 2001, **65**, 141–148.
8. H. Katagiri, Thin Solid Films, 2005, **480-481**, 426–432.

9. T. Tanaka, D. Kawasaki, M. Nishio, Q. Guo, and H. Ogawa, Phys. Status Solidi C, 2006, **3**, 2844–2847.

10. B.-A. Schubert, B. Marsen, S. Cinque, T. Unold, R. Klenk, S. Schorr, and H. W. Schock, Prog. Photovolt: Res. Appl., 2011, **19**, 93–96.

11. M. Bär, B.-A. Schubert, B. Marsen, R. G. Wilks, S. Pookpanratana, M. Blum, S. Krause, T. Unold, W. Yang, L. Weinhardt, C. Heske, and H.-W. Schock, Appl. Phys. Lett., 2011, **99**, 222105.

12. K. Wang, O. Gunawan, T. Todorov, B. Shin, S. J. Chey, N. A. Bojarczuk, D. Mitzi, and S. Guha, Appl. Phys. Lett., 2010, **97**, 143508.

13. T. Tanaka, T. Nagatomo, D. Kawasaki, M. Nishio, Q. Guo, A. Wakahara, A. Yoshida, and H. Ogawa, J. Phys. Chem. Solids, 2005, **66**, 1978–1981.

14. K. Jimbo, R. Kimura, T. Kamimura, S. Yamada, W. S. Maw, H. Araki, K. Oishi, and H. Katagiri, Thin Solid Films, 2007, **515**, 5997–5999.

15. H. Katagiri, K. Jimbo, S. Yamada, T. Kamimura, W. S. Maw, T. Fukano, T. Ito, and T. Motohiro, Appl. Phys. Express, 2008, **1**, 041201.

16. H. Katagiri, K. Jimbo, M. Tahara, H. Araki, and K. Oishi, Mater. Res. Soc. Symp. Proc., 2009, **1165**, M04–01.

17. P. A. Fernandes, P. M. P. Salomé, and A. F. da Cunha, Semicond. Sci. Technol., 2009, **24**, 105013.

18. H. Yoo and J. Kim, Thin Solid Films, 2010, **518**, 6567–6572.

19. N. Momose, M. T. Htay, T. Yudasaka, S. Igarashi, T. Seki, S. Iwano, Y. Hashimoto, and K. Ito, Jpn. J. Appl. Phys., 2011, **50**, 01BG09.

20. M. Johnson, S. V. Baryshev, E. Thimsen, M. Manno, X. Zhang, I. V. Veryovkin, C. Leighton, and E. S. Aydil, Energy Environ. Sci., 2014, 10.1039/c3ee44130j.

21. T. K. Todorov, J. Tang, S. Bag, O. Gunawan, T. Gokmen, Y. Zhu, and D. B. Mitzi, Adv. Energy Mater., 2013, **3**, 34.

22. W. Wang, M. T. Winkler, O. Gunawan, T. Gokmen, T. K. Todorov, Y. Zhu, and D. B. Mitzi, Adv. Energy Mater., 2013, 10.1002/aenm.201301465.

23. T. Todorov and D. B. Mitzi, Eur. J. Inorg. Chem., 2010, **2010**, 17–28.

24. C. M. Fella, A. R. Uhl, Y. E. Romanyuk, and A. N. Tiwari, Phys. Status Solidi A, 2012, **209**, 1043–1048.

25. Y. Sun, K. Zong, H. Zheng, H. Wang, J. Liu, H. Yan, and M. Zhu, Mater. Lett., 2013, **92**, 195–197.

26. G. M. Ilari, C. M. Fella, C. Ziegler, A. R. Uhl, Y. E. Romanyuk, and A. N. Tiwari, Sol. Energ. Mat. Sol. C., 2012, **104**, 125–130.

27. K. Tanaka, M. Oonuki, N. Moritake, and H. Uchiki, Sol. Energ. Mat. Sol. C., 2009, **93**, 583–587.

28. K. Maeda, K. Tanaka, Y. Nakano, and H. Uchiki, Jpn. J. Appl. Phys., 2011, **50**, 05FB08.

29. A. Fischereder, T. Rath, W. Haas, H. Amenitsch, J. Albering, D. Meischler, S. Larissegger, M. Edler, R. Saf, F. Hofer, and G. Trimmel, Chem. Mater., 2010, **22**, 3399–3406.

30. M. Kurokawa, K. Tanaka, K. Moriya, and H. Uchiki, Jpn. J. Appl. Phys., 2012, **51**, 10NC33.

31. W. Ki and H. W. Hillhouse, Adv. Energy Mater., 2011, **1**, 732–735.

32. T. Schnabel, M. Löw, and E. Ahlswede, Sol. Energ. Mat. Sol. C., 2013, **117**, 324–328.

33. H. Xin, J. K. Katahara, I. L. Braly, and H. W. Hillhouse, Adv. Energy Mater., 2014, 10.1002/aenm.201301823.

34. W. Yang, H.-S. Duan, B. Bob, H. Zhou, B. Lei, C.-H. Chung, S.-H. Li, W. W. Hou, and Y. Yang, Adv. Mater., 2012, **24**, 6323–6329.

35. S.-N. Park, S.-J. Sung, D.-H. Son, D.-W. Kim, M. Gansukh, H. Cheong, and J.-K. Kang, RSC Adv., 2014, **4**, 9118–9125.

36. A. R. Uhl, C. Fella, A. Chirilă, M. R. Kaelin, L. Karvonen, A. Weidenkaff, C. N. Borca, D. Grolimund, Y. E. Romanyuk, and A. N. Tiwari, Prog. Photovolt: Res. Appl., 2012, **20**, 526–533.

37. G. Wang, W. Zhao, Q. Tian, L. Huang, D. Pan, Y. Cui, and S. Gao, ACS Appl. Mater. Interfaces, 2013, **5**, 10042–10047.

38. D. B. Mitzi, O. Gunawan, T. K. Todorov, K. Wang, and S. Guha, Sol. Energ. Mat. Sol. C., 2011, **95**, 1421–1436.

39. T. Todorov, H. Sugimoto, O. Gunawan, T. Gokmen, and D. B. Mitzi, IEEE J. Photovolt., 2014, **4**, 483–485.

40. Z. Su, K. Sun, Z. Han, H. Cui, F. Liu, Y. Lai, J. Li, X. Hao, Y. Liu, and M. A. Green, J. Mater. Chem. A, 2014, **2**, 500–509.

41. N. Kamoun, H. Bouzouita, and B. Rezig, Thin Solid Films, 2007, **515**, 5949–5952.

42. N. Nakayama and K. Ito, Appl. Surf. Sci., 1996, **92**, 171–175.

43. K. Maeda, K. Tanaka, Y. Fukui, and H. Uchiki, Sol. Energ. Mat. Sol. C., 2011, **95**, 2855–2860.

44. J. J. Scragg, T. Ericson, T. Kubart, M. Edoff, and C. Platzer-Björkman, Chem. Mater., 2011, **23**, 4625–4633.

45. B. D. Chernomordik, A. E. Béland, D. D. Deng, L. F. Francis, and E. S. Aydil, Chem. Mater., 2014, 10.1021/cm500791a.

46. C. Leidholm, C. Hotz, A. Breeze, C. Sunderland, and W. Ki, NREL Subcontract Rep., 2012, NREL/SR–5200–56501.

47. C. Steinhagen, M. G. Panthani, V. Akhavan, B. Goodfellow, B. Koo, and B. A. Korgel, J. Am. Chem. Soc., 2009, **131**, 12554–5.

48. Q. Guo, H. W. Hillhouse, and R. Agrawal, J. Am. Chem. Soc., 2009, **131**, 11672–11673.

49. B. D. Chernomordik, A. E. Béland, N. D. Trejo, A. A. Gunawan, D. D. Deng, K. A. Mkhoyan, and E. S. Aydil, J. Mater. Chem. A, 2014, 10.1039/C4TA01658K.

50. S. C. Riha, B. A. Parkinson, and A. L. Prieto, J. Am. Chem. Soc., 2009, **131**, 12054–12055.

51. Q. Guo, G. M. Ford, W.-C. Yang, B. C. Walker, E. A. Stach, H. W. Hillhouse, and R. Agrawal, J. Am. Chem. Soc., 2010, **132**, 17384–17386.

52. A. Singh, H. Geaney, F. Laffir, and K. M. Ryan, J. Am. Chem. Soc., 2012, **134**, 2910–2913.

53. A. Shavel, J. Arbiol, and A. Cabot, J. Am. Chem. Soc., 2010, **132**, 4514–4515.

54. Y. Liu, D. Yao, L. Shen, H. Zhang, X. Zhang, and B. Yang, J. Am. Chem. Soc., 2012, **134**, 7207–7210.

55. Y. Cao, M. S. Denny, J. V Caspar, W. E. Farneth, Q. Guo, A. S. Ionkin, L. K. Johnson, M. Lu, I. Malajovich, D. Radu, H. D. Rosenfeld, K. R. Choudhury, and W. Wu, J. Am. Chem. Soc., 2012, **134**, 15644–15647.

56. C. K. Miskin, W. C. Yang, C. J. Hages, N. J. Carter, C. S. Joglekar, E. A. Stach, and R. Agrawal, Prog. Photovolt: Res. Appl., 2014, 10.1002/pip.2472.

57. G. Wang, W. Zhao, Y. Cui, Q. Tian, S. Gao, L. Huang, and D. Pan, ACS Appl. Mater. Interfaces, 2013, **5**, 10042–10047.

58. Q. Guo, G. M. Ford, W.-C. Yang, C. J. Hages, H. W. Hillhouse, and R. Agrawal, Sol. Energ. Mat. Sol. C., 2012, **105**, 132–136.

59. R. Mainz, B. C. Walker, S. S. Schmidt, O. Zander, A. Weber, H. Rodriguez-Alvarez, J. Just, M. Klaus, R. Agrawal, and T. Unold, Phys. Chem. Chem. Phys., 2013, **15**, 18281.

60. W. Wang, S.-Y. Han, S.-J. Sung, D.-H. Kim, and C.-H. Chang, Phys. Chem. Chem. Phys., 2012, **14**, 11154–11159.

61. Q. Guo, G. M. Ford, H. W. Hillhouse, and R. Agrawal, Nano Lett., 2009, **9**, 3060–3065.

62. Q. Tian, X. Xu, L. Han, M. Tang, R. Zou, Z. Chen, M. Yu, J. Yang, and J. Hu, CrystEngComm, 2012, **14**, 3847.

63. M. Lu, Y. Cao, J. V Caspar, I. Malajovich, D. Radu, and H. D. Rosenfeld, 2011 37th IEEE Photovolt. Spec. Conf., 2011, 000402–000406.

64. J.-O. Jeon, K. D. Lee, L. Seul Oh, S.-W. Seo, D.-K. Lee, H. Kim, J.-H. Jeong, M. J. Ko, B. Kim, H. J. Son, and J. Y. Kim, ChemSusChem, 2014, **7**, 1073–1077.

65. S. Ahmed, K. B. Reuter, O. Gunawan, L. Guo, L. T. Romankiw, and H. Deligianni, Adv. Energy Mater., 2012, **2**, 253–259.

CHAPTER 3

Rapid Facile Synthesis of Cu_2ZnSnS_4 Nanocrystals

3.1 Introduction

Copper zinc tin sulfide (Cu_2ZnSnS_4 or CZTS) is an emerging material for thin film solar cells comprised of sustainable earth abundant elements.[1,2] A potentially low cost approach for making thin CZTS films relies on coating suitable substrates with a thin layer of CZTS nanocrystals from colloidal dispersions and then annealing this layer to form a polycrystalline film. Several CZTS nanocrystal synthesis methods have been reported, including solvothermal,[3,4] microwave-assisted,[5,6] and hot-injection.[7–9] Most methods require one hour (or longer) for synthesis and produce an average crystal size between ~5 and ~25 nm. CZTS nanocrystals smaller than ~3 nm in diameter exhibit quantum confinement, which introduces opportunities for band-gap tunable devices with sustainable and non-toxic materials.[10,11] On the other hand, a significant challenge for nanocrystal dispersion based thin film deposition techniques is cracking due to capillary stresses that develop during drying. These cracks are undesirable because they may lead to electrical shorts. Because the capillary forces are inversely proportional to the particle radius, increasing the particle size is one way to reduce the likelihood of crack formation. Herein, we report a rapid and facile CZTS nanocrystal synthesis using a hot-injection approach with thermally decomposable precursors wherein the average nanocrystal size can be controlled between ~2 nm and ~40 nm with one variable—temperature—and the total reaction and growth time is limited to less than 10 minutes.

3.2 Experimental

3.2.1 Materials

Oleic acid (technical grade, 90%), oleylamine (technical grade, 70%), 1-octadecene (technical grade, 90%), toluene (HPLC grade, 99.9%), sodium diethyldithiocarbamate trihydrate (ACS reagent, Sigma Aldrich), copper (II) chloride dihydrate (ACS grade, 99+%), zinc chloride (reagent grade, 98%), and tin (IV) chloride pentahydrate (98%) were purchased from Sigma-Aldrich. Reagent alcohol (histological grade, 90% ethyl alcohol, 5% methyl alcohol, 5% butyl alcohol) was purchased from Fisher Scientific. Quartz polished plates were purchased from GM Associates, Inc.

3.2.2 Precursor Synthesis Procedures

The cation and sulfur sources were copper(II) diethyldithiocarbamate, zinc(II) diethyldithiocarbamate, and tin(IV) diethyldithiocarbamate. Henceforth, these molecules are referred to as the precursors and labeled as $Cu(dedc)_2$, $Zn(dedc)_2$, and $Sn(dedc)_4$, respectively. Each of the three precursors were synthesized from their respective chloride salt (*i.e.,* copper(II) chloride, zinc chloride, or tin(IV) chloride) and sodium diethyldithiocarbamate.

For **$Cu(dedc)_2$**: 150 mL of reagent alcohol was used to dissolve 9.0 g of sodium diethyldithiocarbamate trihydrate. Separately, 4.23 g of copper(II) chloride was dissolved in 50 mL of reagent alcohol. The carbamate-containing solution was then added dropwise to the copper chloride solution while stirring constantly. The resulting black precipitate was separated via filter, washed four times with ultra-high purity deionized water to remove unwanted salts, washed twice with cold acetone to remove the water, and finally dried in a desiccator under rough vacuum.

For **$Zn(dedc)_2$**: synthesis procedure is the same as that for $Cu(dedc)_2$, except that 3.38 g of zinc chloride (in lieu of copper(II) chloride) was used.

For **$Sn(dedc)_4$**: 140 mL of reagent alcohol was used to dissolve 9.6 g of sodium diethyldithiocarbamate trihydrate. Separately, 3.0 g of tin(IV) chloride was dissolved in 50 mL of regant alcohol. Following, as with the other two precursors, the carbamate-

containing solution was added dropwise to the tin(IV) chloride solution while stirring constantly. The resulting orange precipitate was rinsed using copious amounts of deionized water followed by two rinses with ice-cold acetone. The orange precipitate powder was then dried in a desiccator with a roughing pump for at least one hour. At this point, purification by recrystallization of $Sn(dedc)_4$ is recommended because possible side reactions could form, for example, tin(II)-diethyldithiocarbamate. These impurities could affect the phase purity of the CZTS nanocrystals. To purify $Sn(dedc)_4$ by recrystallization, the orange precipitate, which was formed after dropwise mixing of the sodium diethyldithiocarbamate with tin(IV) chloride, was washed four times with ultra-high purity deionized water, twice with cold acetone, and subsequently dried in a desiccator. Following, the orange powder was dissolved in 800 mL of boiling acetone with vigorous stirring. The acetone solution was boiled until it turned cloudy (~650 mL remaining), at which point the flask was carefully removed from heat and allowed to cool to room temperature overnight. The flask was then cooled to -20 ˚C in a freezer and kept there for one day. The resulting precipitates and crystals were washed several times with ice-cold acetone and filtered to retain only the millimeter-sized reddish-orange crystals, which were dried in a desiccator under rough vacuum and stored in a freezer. Yellow-orange crystals are undesired. A photograph of the three precursor powders is shown in Figure 3.1.

Figure 3.1 Photograph of the three precursors: (black) $Cu(dedc)_2$, (white) $Zn(dedc)_2$, and (red-orange) $Sn(dedc)_4$.

3.2.3 Colloidal CZTS Nanocrystal Synthesis

The precursor powder amounts were chosen based on the desired stoichiometry. Using 54 mg of $Cu(dedc)_2$, 27.2 mg $Zn(dedc)_2$, and 53.4 mg of $Sn(dedc)_4$ yields ~30 mg of stoichiometric Cu_2ZnSnS_4 nanocrystals. Typically, $Zn(dedc)_2$ powder is sticky and care must be taken to minimize its loss during transfer to the flask. We found that adjusting $Zn(dedc)_2$ mass to 28 mg gave near stoichiometric CZTS. The three precursor powders were mixed with 4 mL of oleic acid and 1 mL of 1-octadecene. One may instead use 5 mL of oleic acid without 1-octadecene to the same effect. It is important that the oleic acid is colorless or very faint yellow. Nanocrystals larger than ~15 nm (determined by X-ray diffraction) could not be synthesized at 280 ˚C when the oleic acid, as received from the supplier, was yellow. (Oleic acid may take on a yellow color when oxidized through air exposure during storage or purification.) While stirring vigorously, the precursor mixture was heated to 60 °C, degassed at 10 mTorr for several minutes, and purged with dry nitrogen gas to remove the air from the flask. The degassing and purge steps were repeated thrice. After the last purge, the precursor mixture was heated to 140 °C under continuous flow of dry nitrogen gas. As the temperature rises, the solid precursor powders dissolve, with $Sn(dedc)_4$ being the last one to do so. All of the solids are completely dissolved within one minute of reaching 140 °C. It is important not to let the precursor solution reach 175 °C to avoid formation of binary tin sulfide precipitates (*i.e.* SnS_2) due to the premature decomposition of $Sn(dedc)_4$. The precursor solution was then cooled and held at 75 °C. Separately, 10 mL of oleylamine was also similarly degassed and purged thrice at 60 °C before heating it to the desired synthesis temperature between 150-340 °C, while stirring. The synthesis temperature determines the average nanocrystal size. The precursor mixture (itself at 75 ˚C) was then extracted via syringe and swiftly injected into the flask containing the hot oleylamine. The reaction solution immediately turned black and then vigorously bubbled and fumed for several minutes. Upon injection, the reaction solution temperature dropped by 10-15% but rose to the original oleylamine temperature within two minutes. After injection, the solution was kept on the heater for a total of ten minutes. However, growth times of several minutes to one hour produced the same result. The reaction solution was then cooled to room temperature by immersing the flask in a cold water bath. Although keeping the precursor

solution at 140 ˚C (instead of 75 ˚C) would decrease the temperature drop the solution experiences upon injection, the precursor solution was cooled to 75 °C to limit the handling of hot organics during injection.

The CZTS nanocrystals were precipitated by adding ~30 mL of reagent alcohol and centrifuging for five minutes. After discarding the supernatant, the CZTS nanocrystals were dispersed in ~1 mL toluene by sonication for several minutes after adding ~0.3 mL of neat oleic acid. The nanocrystals were then washed a second time by adding ~20 mL reagent alcohol and centrifuging for five minutes. Following, the colorless supernatant was discarded and the CZTS nanocrystals were redispersed in 1 mL toluene with 0.01 vol.% oleic acid and sonicated for one hour.

3.2.4 Discussion Regarding Addition of Oleic Acid for Dispersing Nanocrystals

The precipitation of nanocrystals via the addition of ethanol followed by centrifuging is referred to as "washing". If oleic acid (*e.g.*, 0.3 mL) is added to the dispersion before the second washing, the nanocrystals precipitate easily during centrifugation. In contrast, if oleic acid is not added prior to washing, a significant fraction of the nanocrystals remain dispersed despite aggregation as evidenced by a black and cloudy supernatant. Consequently, the yield of precipitated nanocrystals decreases drastically. We found that this observation may depend on the oleylamine supplier and the batch. For example, when one particular batch of oleylamine was used during the synthesis (Sigma Aldrich Lot No. BCBC6912), the nanocrystals could be precipitated with near 100% yield (clear supernatant) without the addition of oleic acid. The CZTS nanocrystals grown with different batches of oleylamines were indistinguishable from each other using the characterization techniques discussed in the manuscript, except in the atomic concentration of carbon in films cast from the nanocrystals as measured by EDS. Nanocrystal films have measurable amounts of carbon because of the presence oleic acid and oleylamine ligands on nanocrystal surfaces. The carbon concentration in films cast from nanocrystals synthesized using the BCBC6912 oleylamine was higher than the carbon concentration in films of nanocrystals synthesized using any other batch of oleylamine, when no oleic acid was used between washings and neat toluene was used

to disperse the nanocrystals. For example, films of nanocrystals grown at 280 °C had ~20 at.% carbon when the BCBC6912 oleylamine was used, but films of nanocrystals grown using any other oleylamine had ~11 at.% carbon. In the latter films, the addition of oleic acid between the first and second washing procedures increased the carbon concentration in the final films to ~14 at.%. The carbon concentration in films of nanocrystals was further increased to ~20 at.% by dispersing the nanocrystals in toluene that contained 0.01 vol.% oleic acid. While we have no definitive explanation for the differences between the oleylamine batches, it appears that impurities in the oleylamine may vary among batches and affect the surface chemistry of CZTS nanocrystals.

3.2.5 Film Preparation

CZTS nanocrystal dispersions (30 mg/ml) were drop cast into a volume formed by a 250 μm thick stainless steel frame clasped onto a 1 in. x 1 in. substrate (*e.g.*, quartz or molybdenum-coated soda lime glass) using binder clips. A plastic funnel, with a micropipette tip attached to its narrow end, was inverted over the film. The frame pins the drying front at the edges of the frame and the funnel slows the drying; this approach eliminated the formation of drying patterns such as "coffee rings."[12] The film was dried in a fume hood for one hour. After drying, the NC film was 2-3 μm thick. Digital photograph(s) of film preparation are included in Figure 3.2.

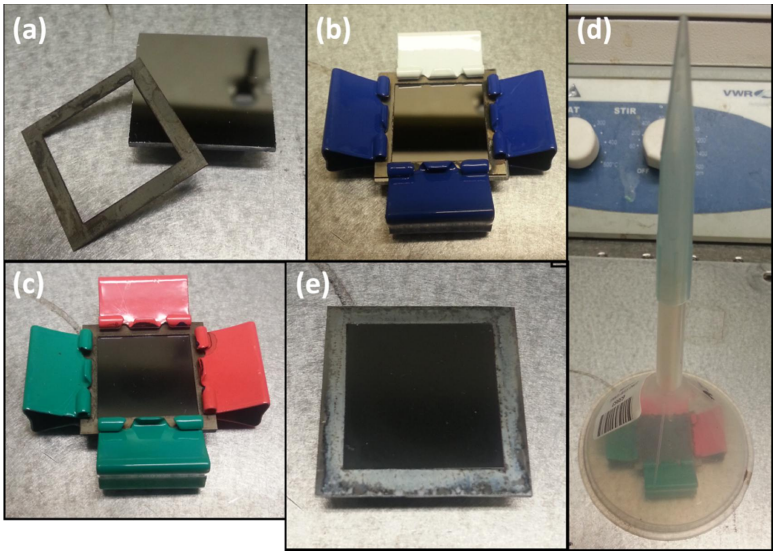

Figure 3.2 Photographs depicting various stages of the film preparation procedure. (a, b) A frame is clasped onto a substrate, such as Mo-coated quartz; using binder clips. (c) The colloidal dispersion is then drop cast inside the frame. (d) A funnel is placed over the film during drying. (e) Finally, the binder clips and frame are removed to produce a nanocrystal film on the substrate.

3.2.4 Solar Cell Preparation

CZTS nanocrystals synthesized with Cu/(Zn+Sn) and Zn/Sn ratios of 0.89 and 1.08, respectively, were drop cast onto soda lime glass (SLG) substrates coated with 400 nm thick sputtered molybdenum film. The CZTS nanocrystal films on Mo-coated SLG and 14 mg of solid sulfur were sealed in evacuated quartz ampoules. The ampoules were annealed in a furnace pre-heated to 600 ˚C. The oven was turned off after 1 hour and allowed to cool naturally before removing the ampoules.[13] This procedure is explained in further detail in Chapter 4.2.3 and Appendix B.1. For solar cells, the substrate was Mo-coated SLG. The Mo films were deposited using DC sputtering in two stages: ≈150 nm in 5 mTorr Ar with 250 W DC power applied to the target and then ≈250 nm in 1 mTorr Ar with 250 W DC power applied to the target. After annealing the CZTS films, a 185 nm CdS film was deposited on CZTS films with chemical bath deposition at 85 °C using an aqueous solution of 3 mM $CdSO_4$, 3 M NH_4OH, and 75 mM $(NH_2)_2CS$. [14] The solution was stirred continuously at 500 rpm. The substrate was placed in the chemical bath at room temperature and the entire solution was heated to 85 ^oC. The deposition time was one hour. CdS deposition was followed by RF sputtering of 100 nm thick nominally intrinsic ZnO (i-ZnO) in 5 mTorr Ar and with 200 W RF power applied to the target. The deposition time was 27 minutes (*i.e.* the deposition rate was ≈ 0.062 nm/s). Following,

the substrate was heated to 150 °C for deposition of 250 nm of tin doped indium oxide (ITO) on the i-ZnO layer using DC sputtering in 5 mTorr Ar and with 150 W DC power applied to the target. The substrate was preheated to 150 °C for 10 minutes before ITO deposition. The deposition time was 27 minutes (*i.e.* the deposition rate was ≈0.15 nm/s). Finally, 50 nm of Ni and 1 μm of Al were sputtered sequentially in 5 mTorr Ar using 250 W and 200 W of DC power, respectively. The deposition times were 5 minutes and 156 minutes for Ni and Al, respectively; *i.e.* the deposition rates were ≈0.17 nm/s and 0.11 nm/s for Ni and Al, respectively. All films were sputtered in an AJA-ATC-2000 sputtering system. The base pressure of the sputtering chamber was $\approx 2.0 \cdot 10^{-6}$ Torr and the target to substrate distance was 19 cm. The substrate holder was rotated at 10 rpm. During ITO deposition, the substrate holder was heated with tungsten-halogen infrared lamps.

3.2.5 Characterization

X-ray diffraction (XRD) from the nanocrystal film was collected using a Bruker D8 Discover equipped with a 2D Hi-Star area detector. The X-ray beam was collimated to an 800 μm spot. Raman spectra were collected using a WiTec alpha300R confocal Raman microscope equipped with a UHTS300 spectrometer and a DV401 CCD detector. An Omnichrome argon ion laser (514.5 nm) was used to illuminate the sample and the beam size was ~300 nm. Raman scattering was collected in a backscattering geometry using an 1800 lines/mm grating. The spectra resolution was ~1.3 cm^{-1}. For all measurements the laser intensity was turned low enough to prevent spectral distortion or peak shifting as a result of local heating. The elemental composition of the CZTS nanocrystals and the atomic carbon concentration were measured using a Thermo-Noran Vantage energy dispersive X-ray spectrometer (EDS) installed within a JEOL 6500 field-emission scanning electron microscope (SEM). The electron energy was 15 keV for all EDS measurements. Transmission electron microscope (TEM) images were recorded using an FEI Tecnai G2 F30 S-TEM system with a Schottky field-emission electron gun operated at 200 kV accelerating voltage.[15] The solar cells were illuminated with simulated sunlight at 100 mW/cm^2 using a 100 W Xe-arc lamp (Oriel) used in conjunction with a 0.125 m monochromator (Newport, Cornerstone 130). Two filters (Newport 81090 and 81092)

were placed in between the lamp and the monochromator to simulate an AM1.5 spectrum. The illuminated area, excluding contacts, was 0.22 cm^2. The monochromator was fitted with a 1200 groove/mm grating and a high reflectivity mirror. The mirror was selected to illuminate the solar cells with the broadband AM1.5 spectrum.[16] The current-voltage (J-V) characteristics of the solar cells were measured using a Keithley 2400 SourceMeter.

3.3 Results and Discussion

When heated separately in a neat solvent, $Cu(dedc)_2$, $Zn(dedc)_2$, and $Sn(dedc)_4$ decompose into their respective binary metal sulfides, Cu_2S, ZnS, and SnS_2, and the decomposition begins at different temperatures for each molecule: $Zn(dedc)_2$, at 240 °C, $Cu(dedc)_2$ at 220 °C, and $Sn(dedc)_4$ at 175 °C.[10] In the presence of oleylamine, however, the temperature at which metal alkyldithiocarbamate molecules decompose is reduced to less than 150 ^oC.[10,17,18] Jung *et al.*[17] proposed that oleylamine accelerates the decomposition of metal alkyldithiocarbamate complexes through coordination with the thiocarbonyl carbon of the dithiocarbamate ligand. Oleic acid, on the other hand, acts as a surface-stabilizing ligand for the nuclei. The ratio of the two molecules—the nuclei-forming oleylamine and the surface-stabilizing oleic acid—can be manipulated to affect the final particle size and shape.[17,19,20] When oleylamine and the three metal diethyldithiocarbamates are mixed in a solvent, CZTS nucleates if the local temperature is above the decomposition temperature of all three precursor molecules in presence of oleylamine (~150 ^oC).

In previously published adaptations of this synthesis approach, oleylamine was injected into a heated mixture of metal alkyldithiocarbamate molecules.[10,18] This approach was used to synthesize 2-7 nm CZTS nanocrystals by varying both the reaction temperature and the volume of oleylamine injected into the heated precursors.[10] Largest nanocrystals (7 nm) were obtained by increasing the reaction temperature (between 150 °C and 175 °C) and/or decreasing the volume of injected oleylamine (4 mL for 2 nm nanocrystals and 0.5 mL for 5 nm nanocrystals). In this approach, the maximum nanocrystal size is limited to less than 7 nm by the decomposition temperature of $Sn(dedc)_4$ (175 ^oC in absence of oleylamine): if the mixture of metal

alkyldithiocarbamate solution is heated above this temperature, SnS_2 nanocrystals are obtained in addition to CZTS. One way to eliminate this restriction is to use tin alkyldithiocarbamates with different alkyl groups.[21] For example, tin(IV) dibutyldithiocarbamate decomposes at ~280 °C.[22] However, the use of other alkyldithiocarbamate molecules increases the complexity and toxicity of the chemistry. For example, synthesis of tin(IV) dibutyldithiocarbamate requires the use of toxic dibutyltin dichloride.

Instead of the above approaches, a wider range of reaction temperatures, and therefore larger variation in CZTS nanocrystal sizes, is achieved by injecting the metal diethyldithiocarbamate solution into hot oleylamine. Upon injection, all three metal diethyldithiocarbamate complexes decompose simultaneously and form CZTS nanocrystals. The average CZTS nanocrystal size can be varied from ~2 to 40 nm by adjusting the oleylamine temperature between 150 and 340 °C, without needing to change other variables such as oleylamine volume, nanocrystal composition, or growth time.

Figure 3.3 shows the XRD from CZTS nanocrystals synthesized at 150 °C, 210 °C, 280 °C, and 340 °C (the temperature, *T*, of the solution at the time of injection). The diffraction peak widths decrease with increasing synthesis temperature because the synthesis yields larger crystals at higher temperatures. All XRD patterns match the expected diffraction pattern for kesterite CZTS (ICDD-ref 04-005-0388, also shown in Figure 1) though the width of the diffraction peaks broaden with decreasing size and several diffraction peaks begin to overlap. The diffraction peaks at 37.0° [(202)], 37.9° [(211)], and 44.9° [(105) and (213)] are clearly resolved in the largest nanocrystals and indicate the unambiguous presence of CZTS. These peaks are absent and very weak in ZnS and tetragonal Cu_2SnS_3, respectively, which otherwise have similar diffraction patterns to CZTS.[23,24] The broad peak at ~20°, which only appears for nanoparticles synthesized at $T \leq 210$ °C, is due to oleylamine and oleic acid capping ligands.[10,25] The volume fraction of the ligands is higher for small nanocrystals and diffraction from oleylamine and oleic acid become detectable. A weak shoulder at 26.9° becomes discernible in the XRD patterns from nanocrystals synthesized at $T \geq 280$ °C. The location of this shoulder matches the wurtzite CZTS (100) diffraction peak. (The wurtzite CZTS

XRD pattern was calculated based on the wurtzite ZnS (2H) crystal structure—space group $P6_3mc$—by replacing the Zn(II) with Cu(I), Zn(II), and Sn(IV).)[26] This may indicate that a minority of CZTS nanocrystals has the wurtzite crystal structure. Other wurtzite CZTS peaks overlap with kesterite CZTS diffractions. Indeed, the wurtzite CZTS phase has been observed in other CZTS nanocrystal synthesis approaches.[26–29] The wurtzite shoulder disappears after films cast from dispersions of these nanocrystals are annealed at temperatures high enough for grain growth (*e.g.*, 600 ˚C as shown in Figure 3.4). This is consistent with this peak arising from the thermodynamically less stable wurtzite CZTS phase.[30]

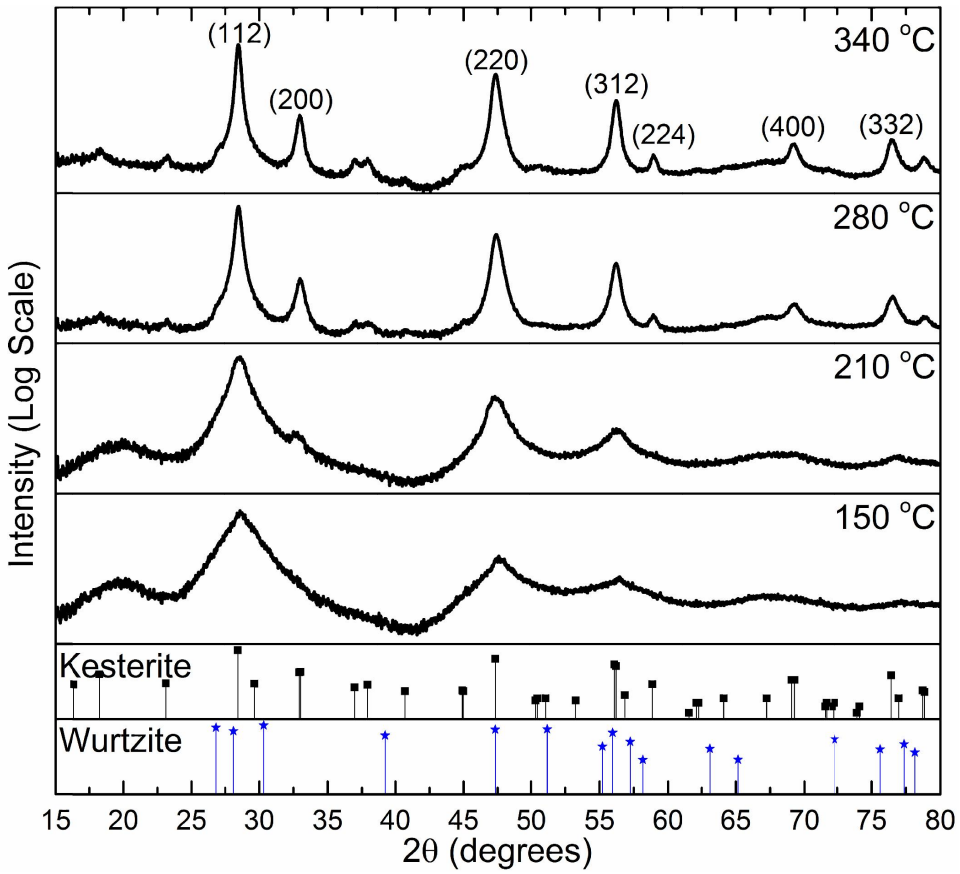

Figure 3.3 XRD from CZTS nanocrystals synthesized at 150 °C, 210 °C, 280 °C, and 340 °C. The XRD patterns match that of kesterite CZTS. A minority of nanocrystals may have the wurtzite structure.

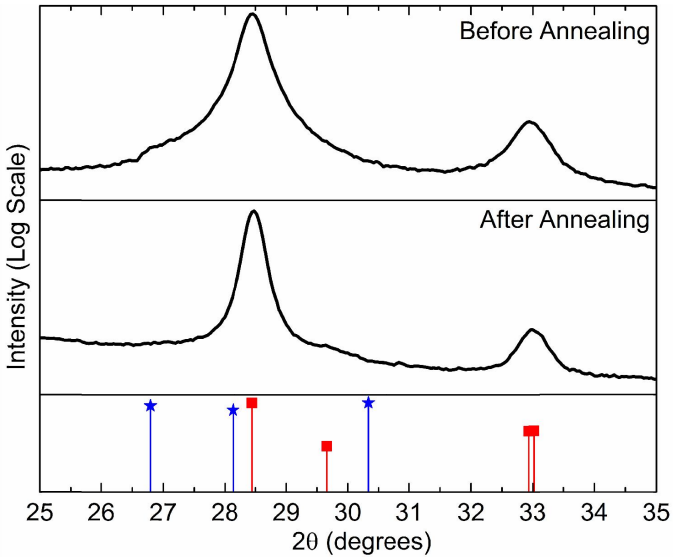

Figure 3.4 XRD patterns for a film cast from ~24 nm CZTS nanocrystals, synthesized at 280 ˚C, (a) before annealing and (b) after annealing at 600 ˚C. The red, ■, symbols represent the diffraction pattern for kesterite CZTS (ICDD-ref 04-005-0388) and the blue, ★, symbols represent the derived wurtzite CZTS pattern.[26] The sample was annealed for one hour inside a sealed quartz ampoule with ~50 Torr of sulfur vapor present.[13]

The presence of any significant amounts of ZnS, including wurtzite ZnS, and tetragonal Cu_2SnS_3 are ruled out using Raman spectroscopy. Figure 3.5 compares the Raman spectra from nanocrystals synthesized at 150 °C, 210 °C, 280 °C, and 340 °C. The nanocrystals synthesized at $T \leq 210$ °C exhibit a single Raman scattering peak centered at 337 cm^{-1}, the expected value for CZTS. The linewidths are broad due to phonon confinement in small nanocrystals, which has also been observed for other materials.[31] The larger nanocrystals grown at $T \geq 280$ °C exhibit narrower Raman scattering linewidths: the A_1 modes at 337 cm^{-1} and 287 cm^{-1} are better defined and the characteristic shoulder at 345-380 cm^{-1} (B and E modes) emerges.[24] Raman scattering corresponding to Cu_2S (475 cm^{-1}) is not present. Raman scattering from ZnS (350 cm^{-1}), and SnS_2 (315 cm^{-1}), if present, is much less than that from CZTS. Even single crystal CZTS exhibits a weak shoulder at 350 cm^{-1} and weak featureless Raman scattering between 287 cm^{-1} and 337 cm^{-1},[32] which overlaps with the expected Raman peaks of ZnS and SnS_2. The absence of SnS_2 XRD peaks indicates that SnS_2 volume fraction is below the detection limit of XRD. However, it is difficult to conclusively rule out small amounts of ZnS.

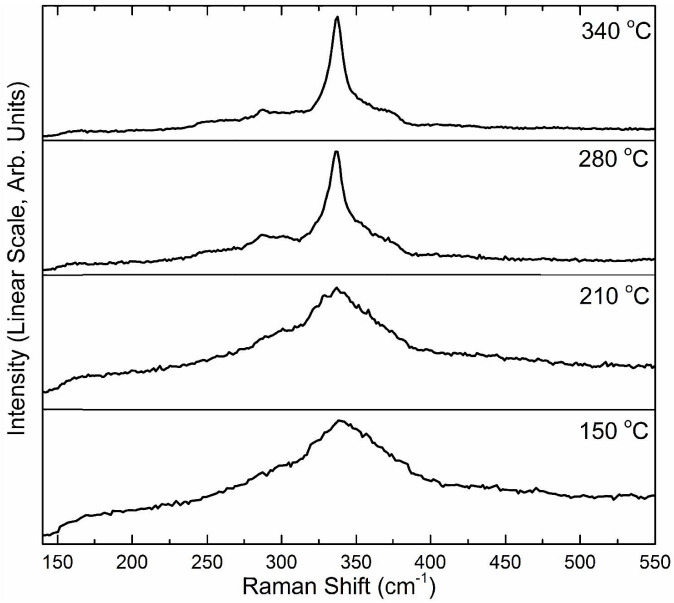

Figure 3.5 Raman spectra from nanocrystals synthesized at 150 °C, 210 °C, 280 °C, and 340 °C. The peak widths vary due to the differences in nanocrystal sizes. The strongest peak in each of the spectra is centered at 337 cm^{-1}, the expected CZTS Raman scattering wavenumber.

EDS was used to analyze the elemental stoichiometry of the nanocrystals. The precursor concentrations given in the Experimental section produced nanocrystals with 2:1:1:4 elemental ratios of Cu:Zn:Sn:S. The stoichiometry may be easily tuned (*e.g.,* slightly Cu poor or Zn rich) around stoichiometric CZTS by varying the molar ratios of precursor powders used in the synthesis. We thus conclude that the nanocrystals are nominally phase-pure CZTS, at least within the detection limits of XRD and Raman scattering.

The sizes of the nanocrystals synthesized at 150 °C, 210 °C, 280 °C and 340 °C were 2 nm, 5 nm, 24 nm, and 40 nm, respectively, as calculated from the widths of the (112) diffraction peaks (at 28.48°) using Scherrer analysis. The absorption spectrum of the nanocrystals synthesized at 150 °C suggests a CZTS nanocrystal size between 2 and 2.5 nm, consistent with the Scherrer analysis. As shown in Figure 3, the latter nanocrystals exhibit an absorption edge that is shifted to higher energies relative to that of larger nanocrystals, a shift characteristic of quantum confinement. From the Tauc plot in the Figure 3 inset, the band gap of the nanocrystals synthesized at 150 °C is estimated to be 1.67 eV. This is consistent with measurements by Khare *et al.*[10] who reported effective band gaps of 1.63 eV and 1.8 eV for 2.5 nm and 2 nm diameter nanocrystals, respectively. Thus, the average size of the nanocrystals synthesized at 150 °C is between

2 and 2.5 nm. The nanocrystals synthesized at higher temperatures are larger than the Bohr radius of CZTS (~3 nm)[3,10] and therefore have the same band gap as bulk CZTS (1.5 eV). The absorption spectrum of the nanocrystals synthesized at 210 °C is shown in Figure 3.6 as an example. The larger nanocrystals synthesized at $T \geq 240$ ˚C agglomerate and are difficult to disperse: they appear turbid and produce absorption spectra convoluted by scattering.

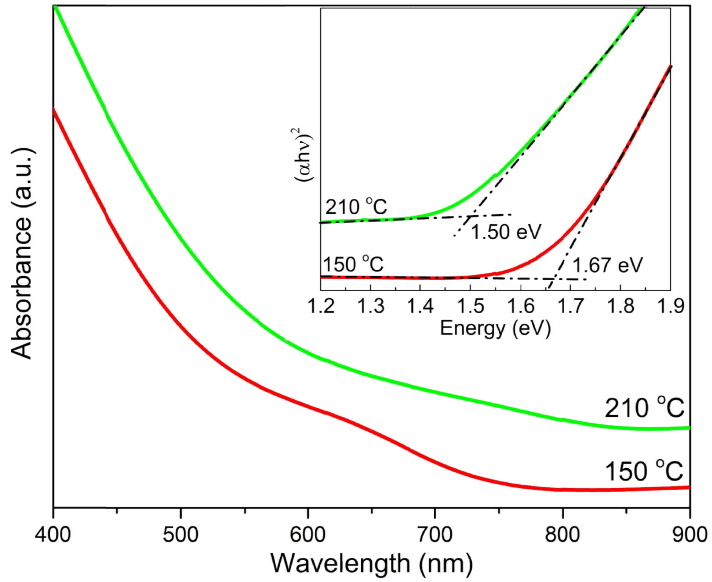

Figure 3.6 Room temperature optical absorption spectra for CZTS nanocrystal dispersions synthesized at 150 °C and 210 °C.. The inset shows the Tauc plot for the corresponding absorbance curves. The absorption edge of nanocrystals synthesized at 150 °C is blue-shifted due to quantum confinement. The spectra have been offset in y-axis for clarity. The long wavelength asymptotes correspond to the zero absorption baseline.

TEM images of nanocrystals synthesized at 280 °C are shown in Figure 3.7. The lattice spacing in the nanocrystals in Figures 3.7a and 3.7b is 3.14±0.01 Å, which corresponds to the (112) plane spacing of kesterite CZTS. The lattice spacing in the inset of Figure 3.7b is 1.92±0.01 Å, which corresponds to the (204) and (220) plane spacings. The larger nanocrystals (>15 nm, *e.g.*, Figure 3.7a) tend to be faceted and non-spherical while the smaller nanocrystals (<10 nm, *e.g.*, Figure 3.7b) tend to be spherical. For example, the nanocrystal in Figure 3.7a is 26 nm along the [112] direction, nearly the same as the crystallite size (24 nm) calculated from the width of the (112) XRD peak. Indeed, for nanocrystals synthesized at $T \geq 280$ °C, the (112) XRD peak yields the largest crystallite sizes while other XRD peaks yield smaller sizes [*e.g.*, 14 nm from (204) and

(220) planes, 15 nm from the (200) plane, and 19 nm from (312) and (116) planes for nanocrystals synthesized at 280 °C]. This variation of the crystallite size calculated from different crystal planes is consistent with the dimensions and nonspherical shapes observed with TEM: the nanocrystals are larger along [112] direction than other directions. TEM images also indicate a broad distribution of nanocrystal sizes, from 5 nm to 30 nm. (Additional TEM images are shown in Figure 3.8). The nanocrystals synthesized at 340 °C are large enough to be observed using SEM (Figure 3.7c). Similarly, there is a broad distribution of nanocrystal sizes, ranging from 10 nm to 100 nm. The average nanocrystal size in Figure 3.7c, measured by averaging the number of grains along randomly chosen lines, is 42 nm, in close agreement with the crystallite size determined from the Scherrer analysis of the XRD peaks (40 nm).

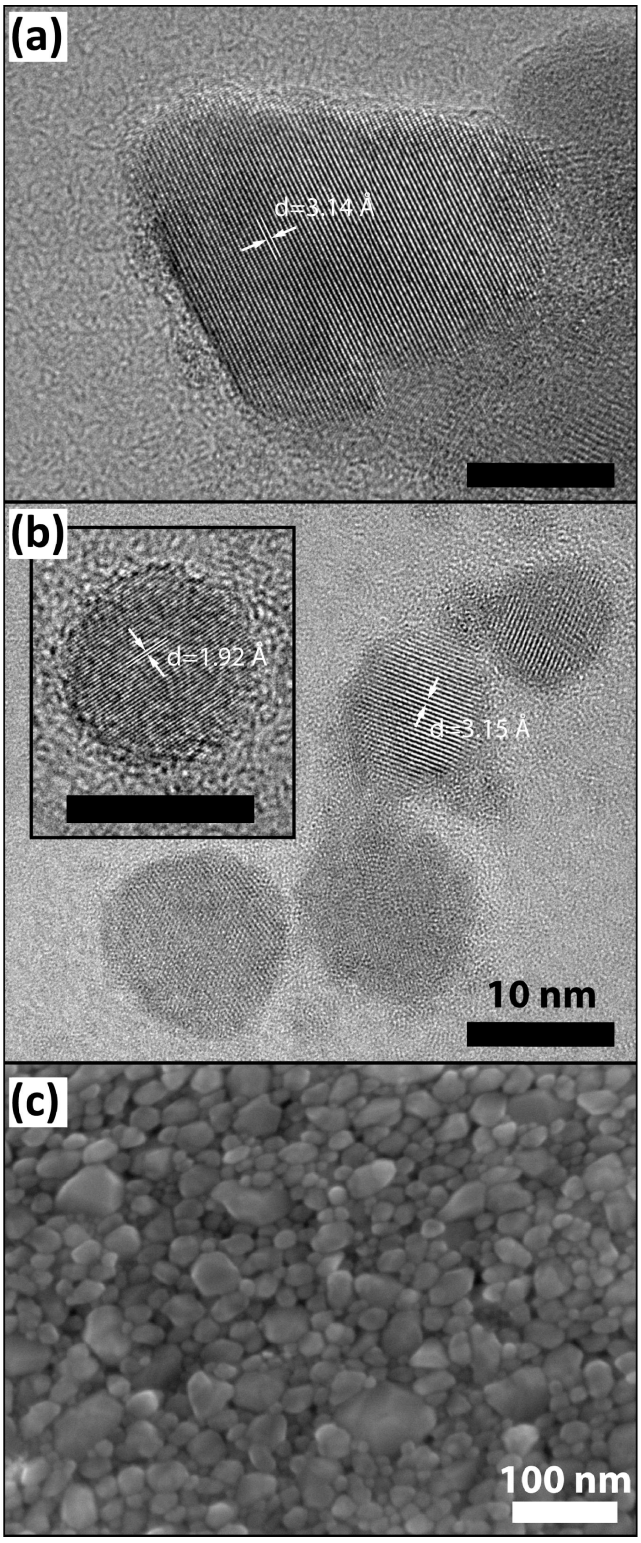

Figure 3.7 High resolution TEM images of CZTS nanocrystals synthesized at 280 °C. The nanocrystals are single-crystalline. Black scale bars in (a) and (b) are 10 nm. (c) SEM image of a film of CZTS nanocrystals synthesized at 340 °C: the average crystal size is 42 nm.

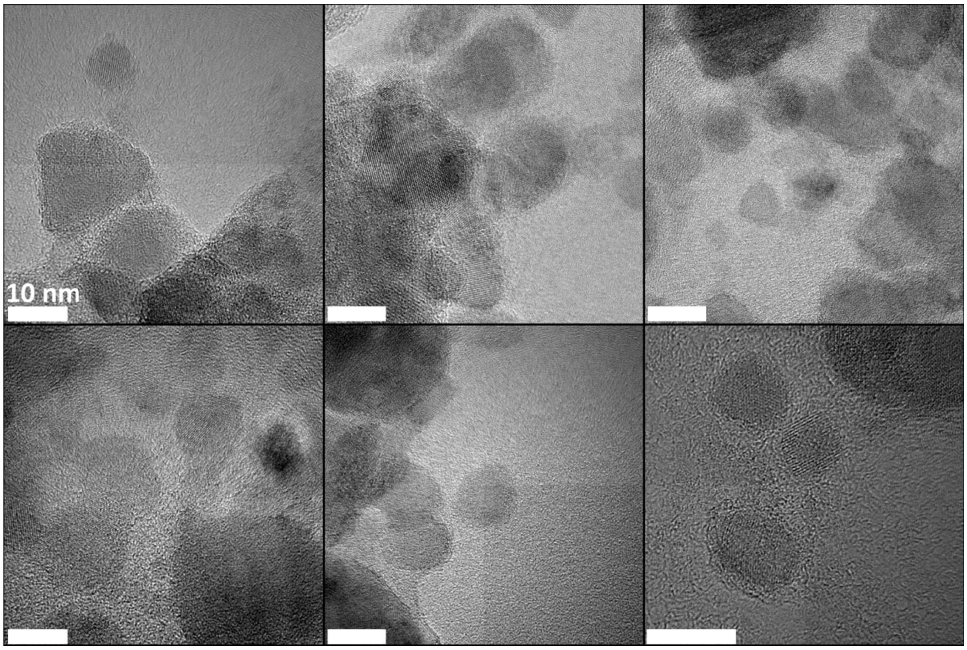

Figure 3.8 Additional TEM images of nanocrystals synthesized at 280 ˚C. All scale bars are 10 nm.

Figure 3.9 shows the average nanocrystal size as a function of the synthesis temperature. The nanocrystal size increases gradually between 150 and 210 °C but faster between 210 and 280 °C. One possible explanation for the faster growth between 210 and 280 °C is that oleic acid and oleylamine react at ~250 °C to form oleyloleamide[19] and the presence of oleyloleamide has been shown to increase the nanocrystal size in systems where the cations are coordinated with acetylacetonate.[20]

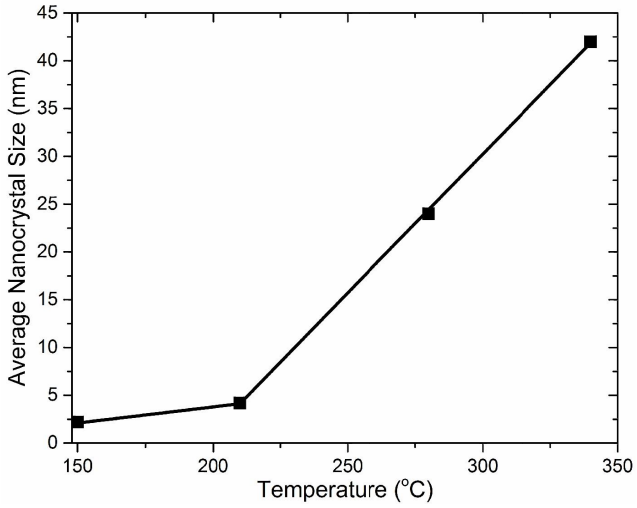

Figure 3.9 Average nanocrystal size as a function of synthesis temperature.

One application of these nanocrystals is in the synthesis of polycrystalline thin films for solar cells. Layers formed by a suitable coating method (*e.g.,* drop casting, spin coating, etc.) are annealed to form polycrystalline films with micron size grains. Cracking in nanocrystal coatings is a problem for most applications, especially for solar cells. Cracks can lead to electrical shorts between device layers and high shunt currents. Crack formation during drying of a nanocrystal film cast from a dispersion is complex and depends on many variables, such as the nanocrystal size, film thickness, solvent evaporation rate, size and coverage of ligand molecules, and the substrate.[33–37] For example, Figure 3.10a shows a film drop cast from a dispersion of 5 nm CZTS nanocrystals on a molybdenum-coated quartz substrate. After drying, micron wide cracks appear and the 2 μm thick film breaks up into ~10 μm × ~15 μm islands. The films crack because capillary pressure between the particles leads to stresses within the film during drying.[34] Cracking can be eliminated by increasing the concentration of oleic acid in the colloidal dispersion (see Figures 3.11a and 3.11b; other film deposition methods are also discussed in Figures 3.12-3.14). The oleic acid reduces cracking by acting as a compliant medium between the particles: oleic acid coronas around the nanocrystals deform and relax the stresses that may otherwise build up within the film.[38] For thin film solar cells, the nanocrystal coatings need to be annealed to promote grain growth. During annealing, a significant fraction of the ligand molecules desorb and/or thermally decomposes into volatile species.[13] (Carbon concentration in films is measured by EDS and is found to be reduced.) The removal of the organic ligands, in addition to concurrent coarsening of the nanocrystals, results in the film experiencing significant volume loss. The film shrinkage contributes to stresses that induce cracking during the annealing process (see Figure 3.11c).

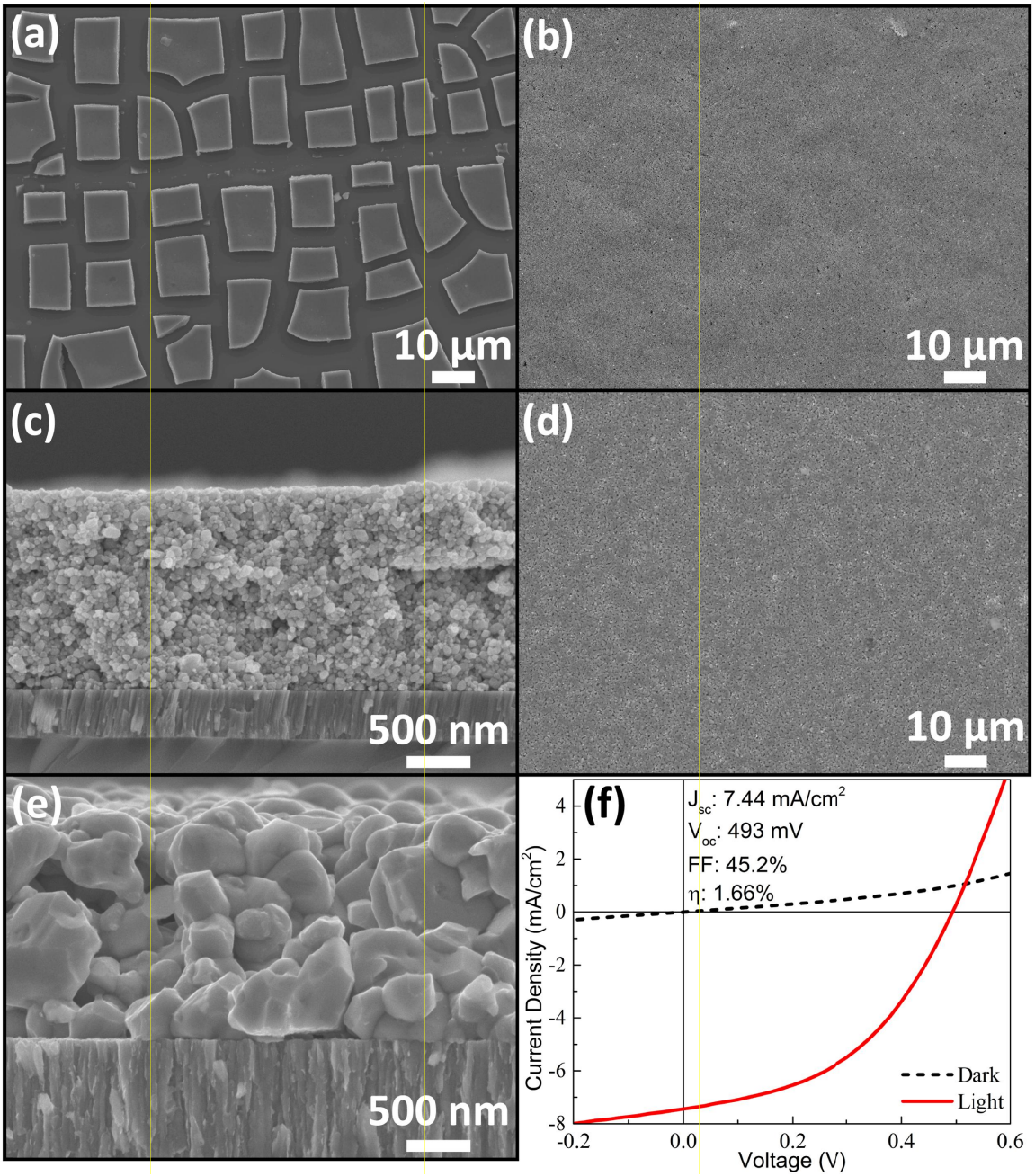

Figure 3.10 SEM images of CZTS nanocrystal films drop cast onto molybdenum-coated quartz substrates using 30 mg/mL dispersions of (a) 5 nm nanocrystals and (b) ~42 nm nanocrystals. (c) Cross-section SEM image of ~42 nm nanocrystals on molybdenum coated SLG. (d) Plan view and (e) cross-sectional SEM images after annealing a film consisting of ~42 nm nanocrystals. (f) J-V characteristics of solar cell made from the film shown in (d) & (e) under dark (dashed) and AM1.5 light (solid) conditions.

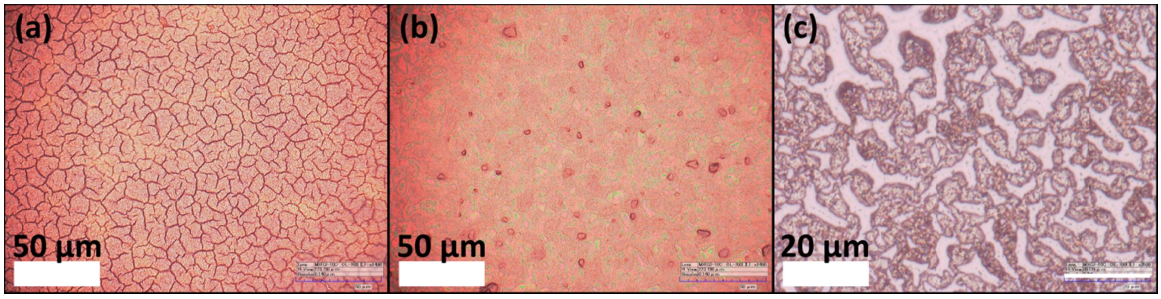

Figure 3.11 Digital optical images of (a) a cracked film drop cast from a dispersion of ~5 nm CZTS nanocrystals in toluene, (b) a film cast using the same nanocrystals but with addition of a very small amount of oleic acid and (c) the same film after annealing at 600 ˚C in 50 Torr of S vapor. During annealing, the film shrinks due to nanocrystal coarsening and sintering and due to the decomposition and volatilization of the ligands. This shrinkage causes the formation of micron-scale cracks.

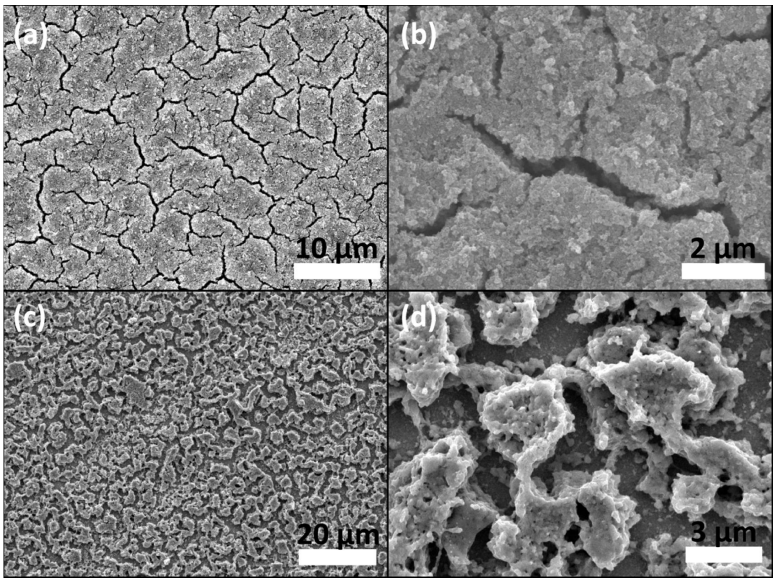

Figure 3.12 (a, b) SEMs of a film deposited from a dispersion of 5 nm CZTS nanocrystals in toluene using a dip coating procedure similar to that used in reference [39]. The film exhibits nanometer-scale cracks. (c, d) These cracks grow during annealing at 600 ˚C in 50 Torr of S vapor.

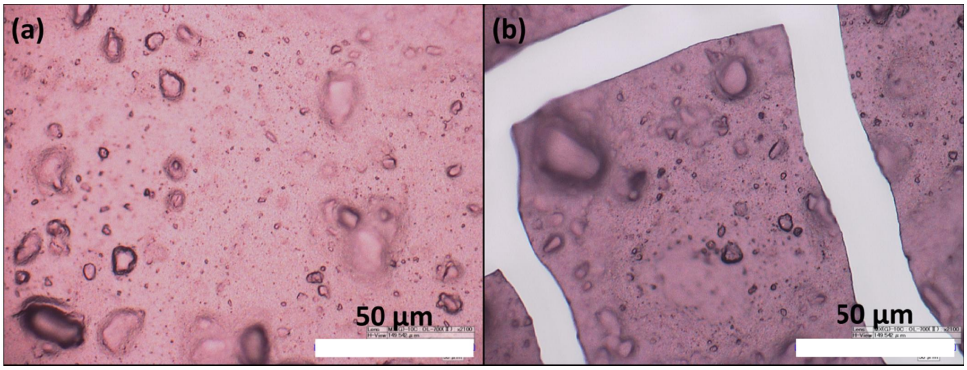

Figure 3.13 (a) Digital optical image of a film comprised of 5 nm CZTS nanocrystals and deposited using doctor blading , where the solvent was hexanethiol and the solid loading was ~400 mg/mL (similar procedure reported by Guo *et al.*[40]). (b) The film cracks, due to volume loss, after heating on the hot plate at 300 ˚C for five minutes. The bumps in the film are nanocrystal aggregates.

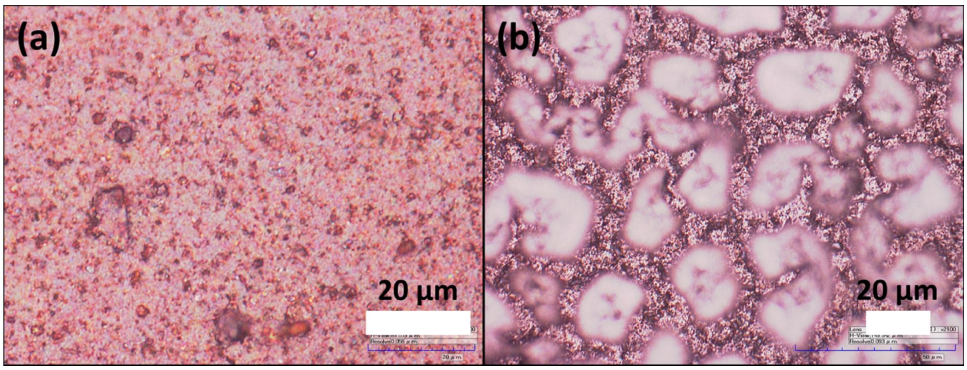

Figure 3.14 (a) Digital optical image of a film comprised of ~13 nm CZTS nanocrystals deposited using doctor blading as in Figure 3.13 but the deposition was done in two steps: two layers were deposited with drying on a hot plate at 300 ˚C for five minutes in between each layer. (b) The film in (a) after annealing at 600 ˚C in 50 Torr of S vapor. The film cracks, forming large islands at the top of the film.

Increasing the nanocrystal size prevents film cracking during drying and annealing. Crack formation is inhibited during drying because the capillary pressure is inversely proportional to nanocrystal radius. For example, Figures 6b and 6c show plan view and cross-sectional SEM images of a ~2 µm thick nanocrystal film drop cast from a dispersion of ~42 nm nanocrystals (synthesized at 340 °C). The film cast from these large nanocrystals is completely crack-free. Increasing nanocrystal size also reduces the volume loss associated with evaporation and decomposition of the organic ligands during annealing. For example, assuming close packed nanocrystals with 1 nm ligand shells, the solid volume increases from 27% to 64% when the nanocrystals size is increased from 5 nm to 40 nm (Figure 3.15). Indeed, Figure 3.10d shows that a film cast from ~42 nm nanocrystals remains crack-free even after annealing (1 hour at 600 ^{o}C on molybdenum-

coated SLG), during which the nanocrystals coarsen and sinter (Figure 3.10e). Moreover, the broad distribution of nanocrystal sizes may impart further advantages toward reduction in cracks: film shrinkage due to coarsening and densification during annealing is reduced when smaller nanocrystals fill the interstitial voids between the large nanocrystals.

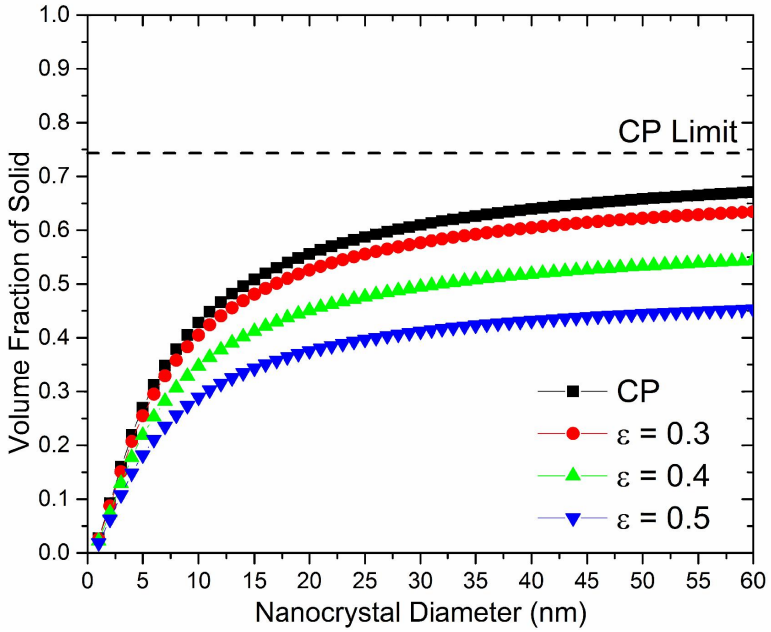

Figure 3.15 The dependence of the solid volume fraction on the nanocrystal diameter in a film comprised of nanocrystals covered with a 1 nm thick ligand shell for several different porosities (ε) down to the close packed (CP) limit (ε=0.26).

Figure 3.10f shows J-V characteristics of a 1.66% efficient solar cell made with the annealed crack-free film shown in Figures 6d and 6e. (See also Figure 3.16). The characteristics represent an unoptimized solar cell: for example, performance may be improved further by reducing the thicknesses of the CdS layer, optimizing the Cu/(Zn+Sn) and Zn/Sn ratios, and shortening the annealing time to reduce the MoS_2 thickness.

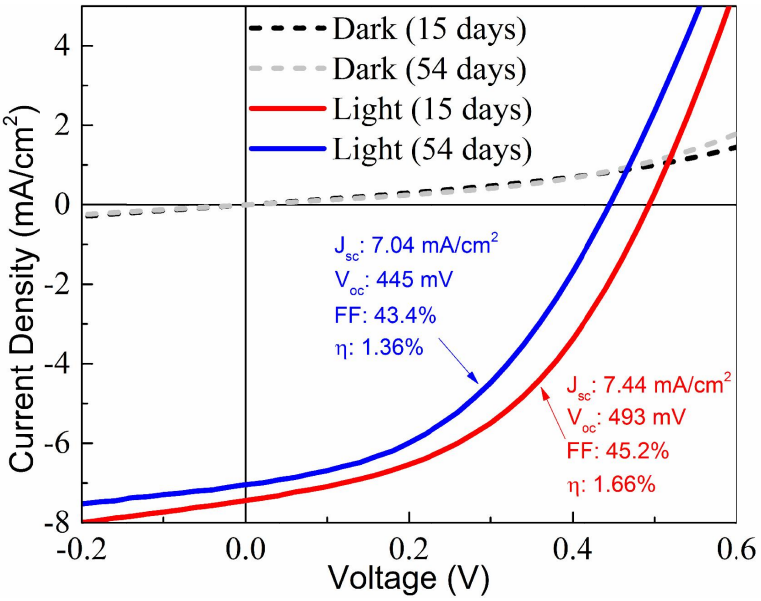

Figure 3.16 J-V curves for the solar cell device shown in Figure 3.10f for two different time periods after fabrication. The J-V characteristics in Figure 3.10f were collected 15 days after fabricating the device and the characteristics are reproduced here as the red curve. The same device was measured again a total of 54 days after fabrication and the J-V characteristics are shown in blue.

3.4 Conclusions

In summary, we describe a method for rapid (≤10 min) synthesis of 2-40 nm diameter CZTS nanocrystals by varying only the synthesis temperature between 150 ˚C and 340 ˚C. The 2 nm nanocrystals synthesized at 150 °C exhibit quantum confinement with an effective band gap of 1.67 eV. Nanocrystals synthesized at higher temperatures have a band gap of 1.5 eV. Films cast from dispersions of small (*e.g.,* 5 nm) nanocrystals exhibit cracks but these cracks are eliminated when dispersions of larger nanocrystals (*e.g.,* 40 nm) are used. The films with larger nanocrystals, which remained crack-free after annealing, were used to make a thin film solar cell.

3.5 References

1. C. A. Wolden, J. Kurtin, J. B. Baxter, I. Repins, S. E. Shaheen, J. T. Torvik, A. A. Rockett, V. M. Fthenakis, and E. S. Aydil, *J. Vac. Sci. Technol. A*, 2011, **29**, 030801.

2. S. Abermann, *Sol. Energy*, 2013, **94**, 37–70.

3. W. C. Liu, B. L. Guo, X. S. Wu, F. M. Zhang, C. L. Mak, and K. H. Wong, *J. Mater. Chem. A*, 2013, **1**, 3182–3186.

4. M. Cao and Y. Shen, *J. Cryst. Growth*, 2011, **318**, 1117–1120.

5. B. Flynn, W. Wang, C. Chang, and G. S. Herman, *Phys. Status Solidi A*, 2012, **209**, 2186–2194.

6. S. W. Shin, J. H. Han, Y. C. Park, G. L. Agawane, C. H. Jeong, J. H. Yun, a. V. Moholkar, J. Y. Lee, and J. H. Kim, *J. Mater. Chem.*, 2012, **22**, 21727–21732.

7. Q. Guo, H. W. Hillhouse, and R. Agrawal, *J. Am. Chem. Soc.*, 2009, **131**, 11672–11673.

8. K.-L. Ou, J.-C. Fan, J.-K. Chen, C.-C. Huang, L.-Y. Chen, J.-H. Ho, and J.-Y. Chang, *J. Mater. Chem.*, 2012, **22**, 14667–14673.

9. C. Zou, L. Zhang, D. Lin, Y. Yang, Q. Li, X. Xu, X. Chen, and S. Huang, *CrystEngComm*, 2011, **13**, 3310–3313.

10. A. Khare, A. W. Wills, L. M. Ammerman, D. J. Norris, and E. S. Aydil, *Chem. Commun.*, 2011, **47**, 11721–11723.

11. T. J. Pundsack, B. D. Chernomordik, A. E. Béland, E. S. Aydil, and D. A. Blank, *J. Phys. Chem. Lett.*, 2013, **4**, 2711–2714.

12. R. D. Deegan, O. Bakajin, T. F. Dupont, G. Huber, S. R. Nagel, and T. A. Witten, *Nature*, 1997, **389**, 827–829.

13. B. D. Chernomordik, A. E. Béland, D. D. Deng, L. F. Francis, and E. S. Aydil, *Chem. Mater.*, 2014, 10.1021/cm500791a.

14. B. S. Tosun, C. Pettit, S. A. Campbell, and E. S. Aydil, *ACS Appl. Mater. Interfaces*, 2012, **4**, 3676–3684.

15. M. J. Behr, K. A. Mkhoyan, and E. S. Aydil, *ACS Nano*, 2010, **4**, 5087–5094.

16. K. S. Leschkies, R. Divakar, J. Basu, E. Enache-Pommer, J. E. Boercker, C. B. Carter, U. R. Kortshagen, D. J. Norris, and E. S. Aydil, *Nano Lett.*, 2007, **7**, 1793–1798.

17. Y. K. Jung, J. Il Kim, and J.-K. Lee, *J. Am. Chem. Soc.*, 2010, **132**, 178–184.

18. D. Pan, L. An, Z. Sun, W. Hou, Y. Yang, Z. Yang, and Y. Lu, *J. Am. Chem. Soc.*, 2008, **130**, 5620–5621.

19. W. Niu, S. Wu, and S. Zhang, *J. Mater. Chem.*, 2011, **21**, 10894–10902.

20. H. Wu, Y. Yang, and Y. C. Cao, *J. Am. Chem. Soc.*, 2006, **128**, 16522–16523.

21. M. A. Malik, M. Afzaal, and P. O'Brien, *Chem. Rev.*, 2010, **110**, 4417–4446.

22. K. Ramasamy, M. A. Malik, and P. O'Brien, *Chem. Sci.*, 2011, **2**, 1170–1172.

23. A.-J. Cheng, M. Manno, A. Khare, C. Leighton, S. A. Campbell, and E. S. Aydil, *J. Vac. Sci. Technol. A*, 2011, **29**, 051203.

24. A. Khare, B. Himmetoglu, M. Johnson, D. J. Norris, M. Cococcioni, and E. S. Aydil, *J. Appl. Phys.*, 2012, **111**, 083707.

25. A. Pein, M. Baghbanzadeh, T. Rath, W. Haas, E. Maier, H. Amenitsch, F. Hofer, C. O. Kappe, and G. Trimmel, *Inorg. Chem.*, 2011, **50**, 193–200.

26. X. Lu, Z. Zhuang, Q. Peng, and Y. Li, *Chem. Commun.*, 2011, **47**, 3141–3143.

27. A. Singh, H. Geaney, F. Laffir, and K. M. Ryan, *J. Am. Chem. Soc.*, 2012, **134**, 2910–2913.

28. M. D. Regulacio, C. Ye, S. H. Lim, M. Bosman, E. Ye, S. Chen, Q.-H. Xu, and M.-Y. Han, *Chemistry*, 2012, **18**, 3127–3131.

29. M. Li, W.-H. Zhou, J. Guo, Y.-L. Zhou, Z.-L. Hou, J. Jiao, Z.-J. Zhou, Z.-L. Du, and S.-X. Wu, *J. Phys. Chem. C*, 2012, **116**, 26507–26516.

30. S. Chen, A. Walsh, Y. Luo, J.-H. Yang, X. G. Gong, and S.-H. Wei, *Phys. Rev. B*, 2010, **82**, 195203.

31. D. Bersani, P. P. Lottici, and X.-Z. Ding, *Appl. Phys. Lett.*, 1998, **72**, 73–75.

32. D. Dumcenco and Y. Huang, *Opt. Mater.*, 2013, **35**, 419–425.

33. A. F. Routh, *Rep. Prog. Phys.*, 2013, **76**, 046603.

34. W. P. Lee and A. F. Routh, *Langmuir*, 2004, **20**, 9885–9888.

35. M. S. Tirumkudulu and W. B. Russel, *Langmuir*, 2004, **20**, 2947–2961.

36. K. Singh and M. Tirumkudulu, *Phys. Rev. Lett.*, 2007, **98**, 218302.

37. M. S. Tirumkudulu and W. B. Russel, *Langmuir*, 2005, **21**, 4938–4948.

38. T. Kanai and T. Sawada, *Langmuir*, 2009, **25**, 13315–13317.

39. J. M. Luther, M. Law, Q. Song, C. L. Perkins, M. C. Beard, and A. J. Nozik, *ACS Nano*, 2008, **2**, 271–280.

40. Q. Guo, G. M. Ford, W.-C. Yang, B. C. Walker, E. A. Stach, H. W. Hillhouse, and R. Agrawal, *J. Am. Chem. Soc.*, 2010, **132**, 17384–17386.

CHAPTER 4

Microstructure Evolution and Crystal Growth In Cu_2ZnSnS_4 Thin Films Formed By Annealing Colloidal Nanocrystal Coatings

4.1 Introduction

Copper zinc tin sulfide (Cu_2ZnSnS_4, or CZTS), copper zinc tin selenide ($Cu_2ZnSnSe_4$, or CZTSe), and their alloys ($Cu_2ZnSn(S_xSe_{1-x})_4$, or CZTSSe) are candidates for environmentally sustainable light absorbing materials for thin film solar cells because they are composed of abundant and nontoxic elements.[1,2] Although the development of CZTSSe solar cells is in its early stages, efficiencies have already risen to 12.6%.[3] While most CZTSSe solar cells are fabricated using vacuum deposition techniques,[4–7] there is growing interest in safe and scalable solution-based methods for low-cost and high-throughput deposition of CZTSSe thin films.[8–11] One potentially low-cost approach is to coat the substrates with a thin film from colloidal CZTS nanocrystal dispersions (inks) to form nanocrystal films, and then anneal these films in sulfur or selenium vapor to form polycrystalline films with 1-3 micron grains. Solar cell efficiencies using this approach have already reached 7.2%[12] with CZTSSe films. However, achieving these efficiencies relied heavily on trial-and-error optimization of multiple process variables and this approach has left gaps in our understanding of the mechanisms that transform the colloidal nanocrystal coatings into polycrystalline films. Further improvements in solar cell performance will require a deeper understanding of the relationships among synthesis, structure and properties of CZTSSe films, and the performance of CZTSSe solar cells. Herein, we study the fundamental factors that govern the microstructure of polycrystalline thin films formed by annealing CZTS nanocrystal

coatings in sulfur vapor. Specifically, we systematically examine the effects of annealing temperature, annealing time, sulfur pressure, and substrate on microstructure development and grain growth in CZTS nanocrystal films.

4.2 Experimental

4.2.1 Materials

Oleic acid (technical grade, 90%), oleylamine (technical grade, 70%), 1-octadecene (technical grade, 90%), and toluene (HPLC grade, 99.9%) were purchased from Sigma-Aldrich. Copper(II), zinc(II), and tin(IV)-diethyldithiocarbamate complexes were made[11] from sodium diethyldithiocarbamate trihydrate (ACS reagent, Sigma Aldrich), copper (II) chloride dihydrate (ACS grade, 99+%), zinc chloride (reagent grade, 98%), and tin (IV) chloride pentahydrate (98%). Reagent alcohol (histological grade, 90% ethyl alcohol, 5% methyl alcohol, 5% butyl alcohol) was purchased from Fischer Scientific. Quartz polished plates and quartz tubing were purchased from GM Associates, Inc. and the soda lime float glass (SLG) substrates were purchased from Valley Design Corp. The sulfur used for annealing was purchased from Cerac, Inc (99.999%).

4.2.2 Colloidal CZTS Nanocrystal Synthesis

In a typical synthesis, 54 mg of copper-diethyldithiocarbamate, 27.2 mg of zinc-diethyldithiocarbamate, and 53.4 mg of tin- diethyldithiocarbamate were mixed in 4 mL of oleic acid and 1 mL of 1-octadecene. While stirring vigorously, the precursor mixture was heated to 60 °C, degassed to 10 mTorr, and purged with dry nitrogen gas to remove atmospheric gases from the flask. The degas-and-purge process was repeated three times. After degassing, the precursor mixture was heated to 140 °C under dry nitrogen gas until all the solids dissolved. This precursor solution was then cooled to and kept at 75 °C. Meanwhile, a separate flask with 10 mL of oleylamine was also degassed and purged in the same manner. After degassing, the oleylamine was heated to 280 °C. Following, the precursor solution was rapidly injected into the hot oleylamine, resulting in simultaneous decomposition of the three precursors and the formation of CZTS nuclei.[11] The reaction solution was kept at 280 °C for 10 min, after which it was cooled to room temperature by

immersing the flask in a cold water bath. The CZTS nanocrystals were precipitated out of the solvent by adding reagent-alcohol (in a 2:1 ratio of alcohol to reaction solution) and centrifuging. After discarding the supernatant, the nanocrystals were washed by dispersing them in toluene and precipitating them again by adding reagent alcohol and centrifuging. Finally, the CZTS nanocrystals were dispersed in toluene to form 30 mg/mL dispersions. CZTS nanocrystals were characterized using a suite of techniques including X-ray diffraction (XRD), Raman scattering, energy dispersive X-ray spectroscopy (EDS) and transmission electron microscopy (TEM). All methods confirmed that the nanocrystals are crystalline and nominally stoichiometric CZTS (see Figure 4.1). The nanocrystals were phase pure within the detection limits of XRD and Raman spectroscopy. The average nanoparticle size was ~25 nm, as calculated from the width of the (112) peak in XRD using the Scherrer equation.

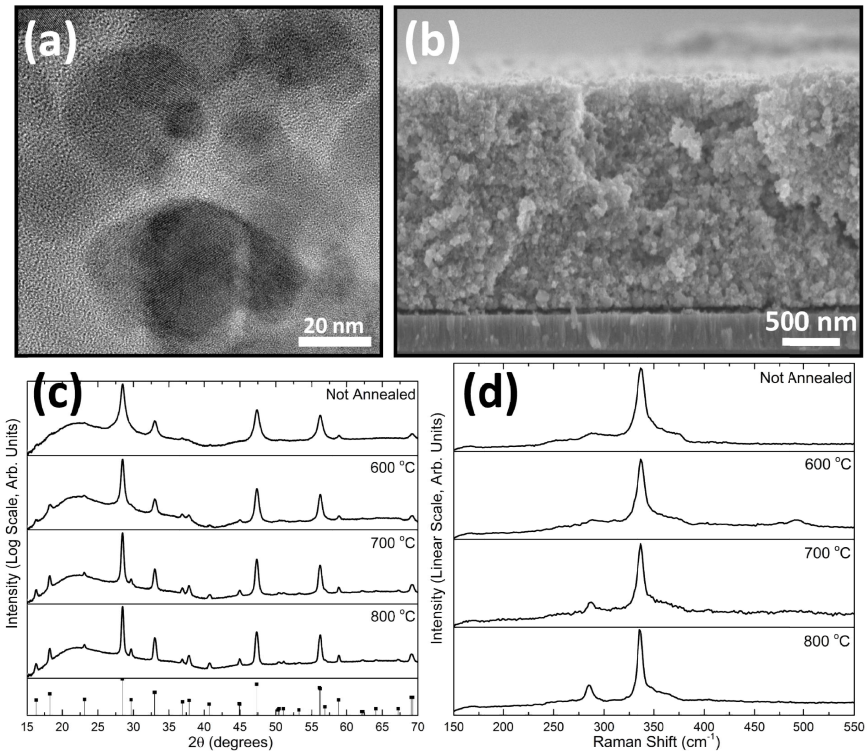

Figure 4.1 (a) TEM image of CZTS nanocrystals used for this study. (a) Cross-section SEM image of as-deposited CZTS nanocrystals before annealing. (c) XRD patterns and (d) Raman spectra of films on quartz before and after annealing at 600, 700, and 800 ˚C with 1 mg S. The nanocrystal composition, measured by EDS, was: 25 at.% Cu, 12 at.% Zn, 13 at.% Sn, and 50 at.% S.

4.2.3 Film Preparation and Annealing

Soda lime glass and quartz substrates (1 in.^{2}), with or without a thin (≈300 nm) molybdenum (Mo) layer, were coated with CZTS nanocrystal films by drop casting from a 30 mg/mL colloidal CZTS nanocrystal dispersion in toluene. The dispersion was drop cast within the volume formed by a 250 μm thick stainless steel frame clasped on top of a 1 in.^{2} substrate. After drying, the resulting NC film was 2-3 μm thick (Figure 4.1b). The substrates coated with the NC films were broken into approximately 0.8 cm by 2.5 cm pieces and placed in pre-cleaned quartz tubes (1 cm inner diameter and 10 cm long) with measured amounts of solid sulfur, evacuated to 10^{-6} Torr, and flame-sealed to produce an ampule (photographs included in Figure 4.2). The mass of sulfur placed in the tube was always less than that required to reach the thermodynamic saturation sulfur vapor pressure (> 4900 Torr at 600 °C).[13] This ensured that sulfur existed only as vapor at the sulfidation temperatures explored in this work and did not condense in the tube or on the sample. The total pressure inside the ampule at different temperatures was calculated using the ideal gas law and the published temperature-dependent sulfur vapor speciation data.[14,15] The sulfur pressure in the tube is limited by the amount of sulfur charged into the tube. To access pressures below the vapor pressure of sulfur at the desired sulfidation temperature, we limit the amount of sulfur charged to the mass that would be needed to achieve the desired pressure. Solid S (below 115 ^{o}C) and liquid S (above 115 ^{o}C) coexist with S vapor until the temperature at which all the S charged is vaporized. The pressure in the ampule is equal to the vapor pressure of sulfur until the entire S charged into the ampule becomes vapor. Thereafter (the discontinuity in the lines in Figure 4.3) only one phase exists and the sulfur pressure follows the ideal gas law. With 1 mg of sulfur sealed in the ~7.9 cm^3 tube, the pressures at 600, 700, and 800 °C were calculated to be ~36, 47, and 58 Torr, respectively. To distinguish them from experiments conducted at higher sulfur pressures (~500 torr) these three pressures are referred nominally as ~50 Torr during the discussion. For the higher sulfur pressure experiments, the mass of sulfur inside the annealing ampule was adjusted such that the sulfur pressure was approximately 500 Torr (more specifically, 500 and 470 Torr using 14 mg and 10 mg solid sulfur at 600 °C and 700 °C, respectively). Figure 4.3 illustrates the pressure in the ampule as a

function of temperature with 1 mg and with 10 mg of solid sulfur loading. The associated calculations are shown in Appendix B.1.

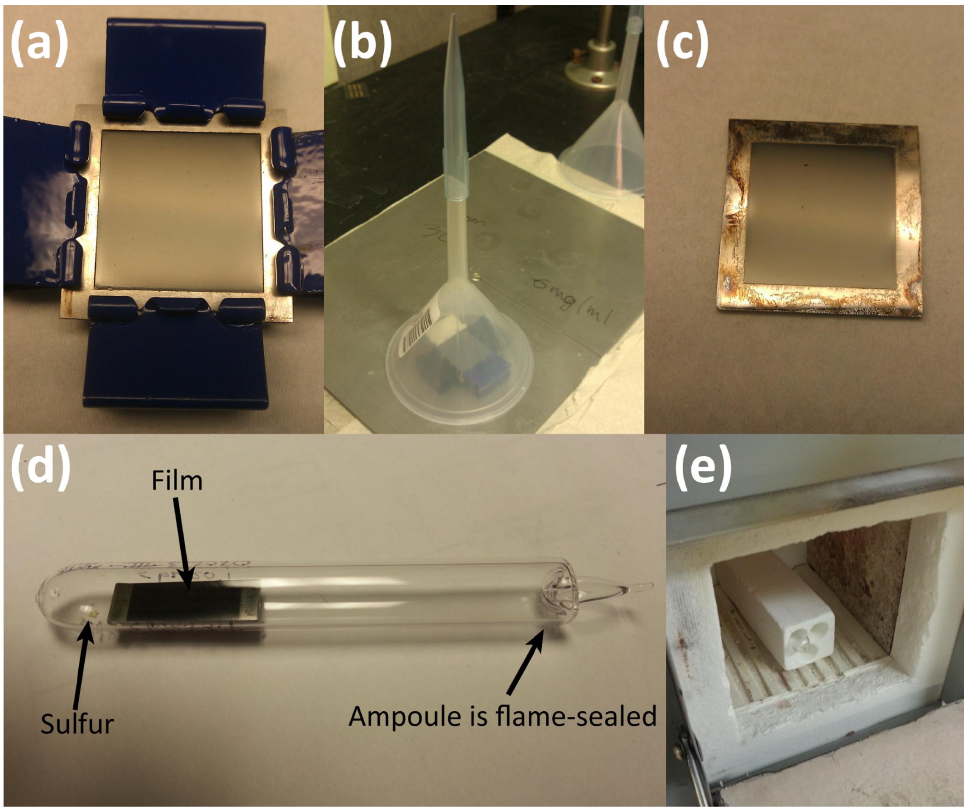

Figure 4.2 (a) A metal frame is clasped onto a 1 in.2 substrate, such as quartz or molybdenum coated quartz, using binder clips and then the nanocrystal dispersion is drop cast into the volume formed by the frame and substrate. (b) A funnel is placed over the film to slow the drying. (c) An example of the resulting film. (d) A sealed quartz ampule with the film and solid sulfur inside. The pressure inside the ampule is ~10-6 Torr. (e) An ampule inside of the ceramic block within a furnace.

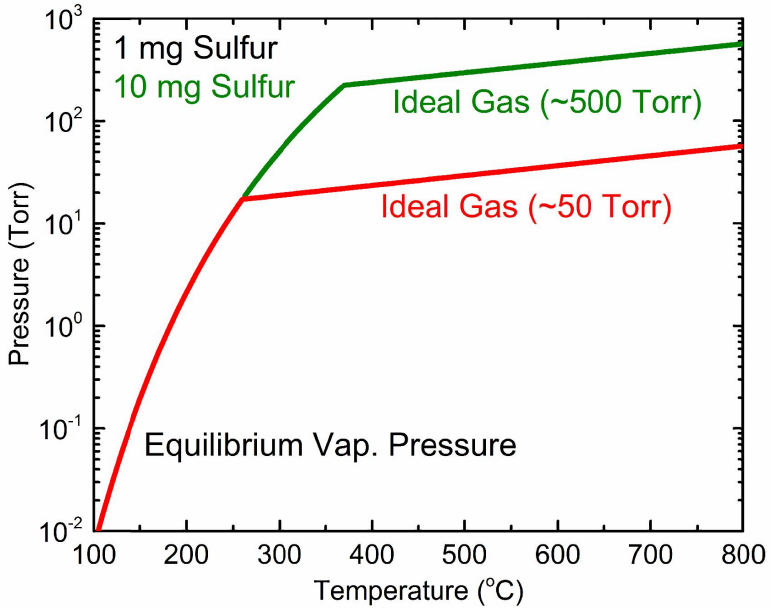

Figure 4.3 The pressure in a sealed ampule as a function of temperature for a solid S loading of 1 mg (red) and 10 mg (green). Solid S (below 115 °C) and liquid S (above 115 °C) coexist with S vapor until the temperature at which all the S charged is vaporized. The pressure in the ampule is equal to the vapor pressure of sulfur until the entire S charged into the ampule becomes vapor. Thereafter (the discontinuity in the lines) only one phase exists and the sulfur pressure follows the ideal gas law. This temperature depends on the amount of S charged. All the sulfur vaporizes at 260 °C and at 370 °C for the cases of 1 mg S and 10 mg S, respectively.

Meanwhile, an alumina block, with pre-drilled slots for the annealing ampules (Figure 4.2e), was placed in a Barnstead Thermolyne 1400 benchtop furnace and the furnace was pre-heated to the desired annealing temperature for at least six hours. The ampules loaded with the CZTS films and the sulfur, were quickly inserted into the hot alumina block and the oven was closed. After the desired annealing time had passed, the oven was turned off and allowed to cool naturally. In a typical cooling period, the oven temperature decreased to 50% of the annealing temperature in 3-4 hours. The ampules were inserted into the block such that approximately 1 cm of the length of the tube stuck out. During the slow cooling step, the sulfur condensed on this cooler end of the annealing ampule and not on the sample.

4.2.4 Characterization

XRD from the films was collected using a Bruker D8 Discover system with a Hi-Star 2D area detector. Raman spectra were collected using the Witec Alpha300R confocal Raman microscope equipped with an Omnichrome Ar ion laser (514.5 nm, ~300

nm beam spot size), a UHTS300 spectrometer and a DV401 CCD detector. The scattered radiation was collected and dispersed with an 1800 lines/mm grating, resulting in 0.02 cm^{-1} spectral resolution. The microstructure and elemental composition of the films were examined using a JEOL 6500 field-emission scanning electron microscope (SEM) equipped with a Thermo-Noran Vantage energy dispersive X-ray spectrometer. The electron energy was 15 keV for both imaging and EDS measurements. Optical transmission through the CZTS films was measured using a Cary 5000UV-Vis-NIR spectrophotomer in the dual beam mode. The transmission spectrum of the substrate (SLG or quartz) was used as the baseline.

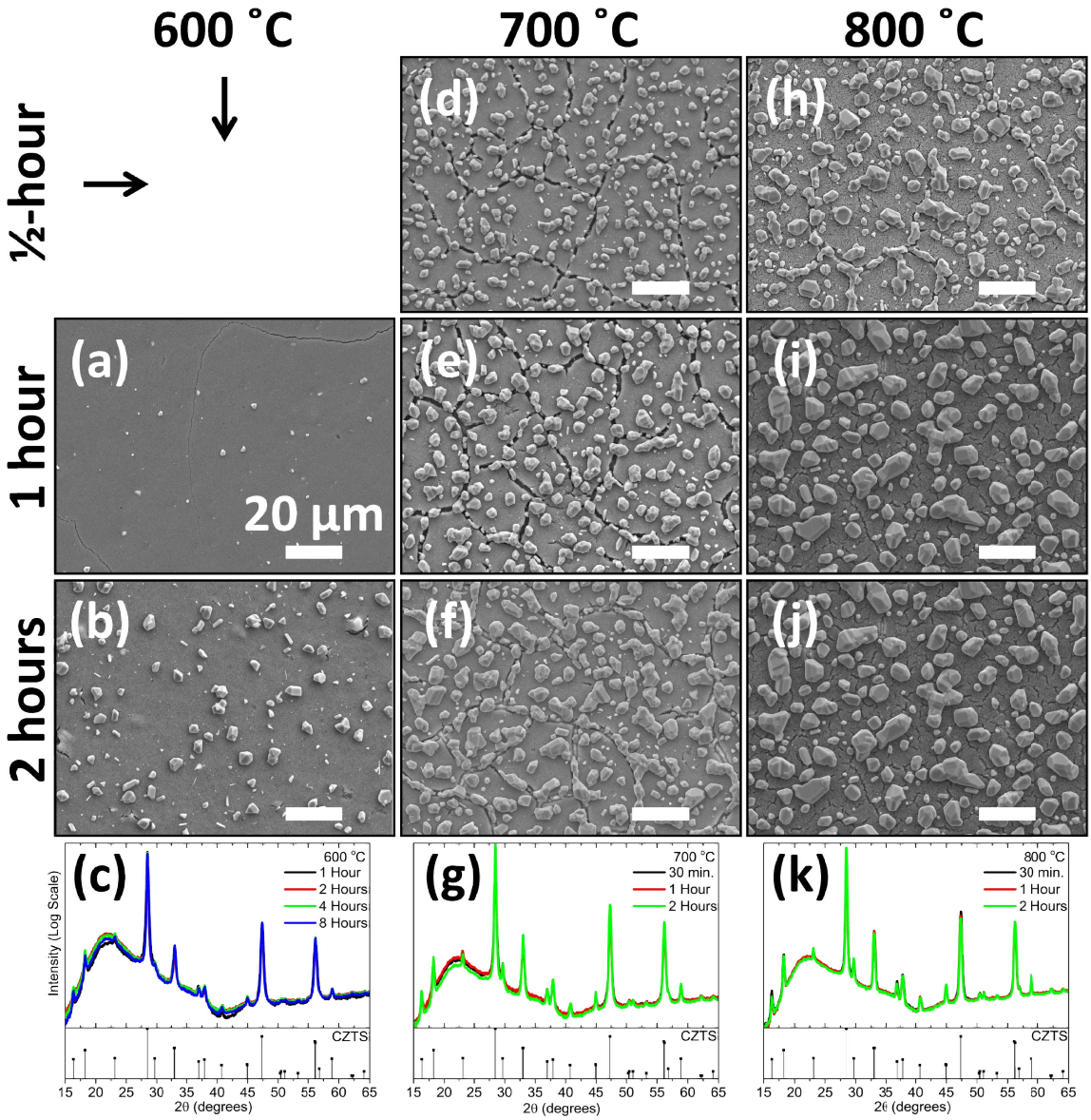

Figure 4.4 Plan view SEM images of CZTS nanocrystal films after annealing at (a-b) 600 °C, (d-f) 700 °C, (h-j) and 800 °C for 30 minutes, 1 hour, and 2 hours in ~50 Torr of sulfur. All films shown were deposited and annealed on fused quartz. XRD patterns for all films annealed at (c) 600 °C, (g) 700 °C, (k) and 800 °C. All scale bars are 20 µm.

4.3 Results and discussion

4.3.1 Annealing Temperature and Annealing Time Dependence of Film Microstructure

Figures 4.4, 4.5 and 4.6 show, respectively, low magnification plan view, high magnification plan view, and cross sectional SEM images of CZTS nanocrystal films

annealed at 600, 700, and 800 °C for ½-hour, one hour, and two hours under ~50 Torr of sulfur vapor. These SEM images show 1-10 micron CZTS grains on top of a layer that is comprised of nanocrystals. Hereafter, this nanocrystal layer is referred to as the floor layer. In the plan view images (Figures 4.4 and 4.5), the nanocrystalline floor layer forms the background while the larger faceted crystals sit on top of this layer. Figure 4.4 c,g and k show that the XRD from all the films match to those expected from CZTS. (See also Figure 4.1 for comparison with nanocrystal films before annealing.) Indeed, detailed characterization of the nanocrystalline floor layer and the large crystals on the top with XRD and Raman spectroscopy showed that they are both CZTS (*vide infra*). The cross-sectional images in Figure 4.6 show that the nanocrystals within the floor layer are larger than the starting colloidal nanocrystals. These images also show that 1-10 micron grains sit on top the nanocrystal floor. These large grains are not emanating from the substrate. This observation suggests that the larger crystals nucleate and grow at the film-vapor interface. Here, nucleation refers to the beginning of abnormal crystal growth, wherein an individual nanocrystal at the top of the film may act as a nucleation point or a new nucleation point may form to initiate abnormal crystal growth. In addition to the film surface, we observe large crystals decorating the interior of stress-induced cracks in the nanocrystal film. See Figure 4.7.

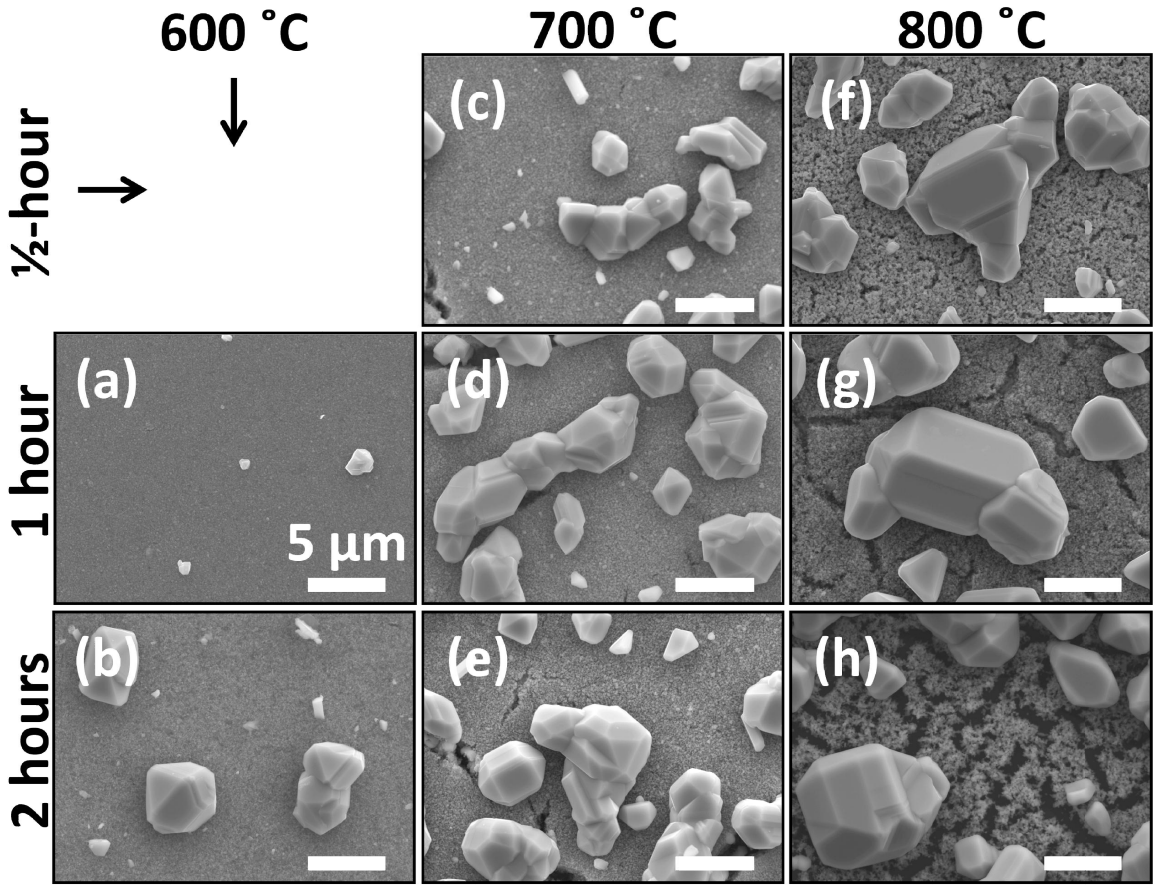

Figure 4.5 Higher magnification plan view SEM images of the films shown in Figure 4.4 (*i.e.*, CZTS nanocrystal films after annealing at (a-b) 600 °C, (c-e) 700 °C, (f-h) and 800 °C for 30 minutes, 1 hour, and 2 hours). All scale bars are 5 µm.

The bimodal size distribution in Figures 4.4-4.6 is reminiscent of abnormal crystal growth encountered during thin film crystallization and grain growth.[16,17] During normal grain growth, the grain size distribution remains monomodal as the average grain size increases. During abnormal grain growth, on the other hand, some fraction of the grains grows faster than others, producing a bimodal distribution. When there is a bimodal distribution, the smaller and larger grain populations are referred to as the normal grains and abnormal grains, respectively. During grain growth, the average sizes of both the normal and abnormal grain populations increase and in both populations large grains grow larger while the smaller ones are annihilated. Classical grain growth in dense thin films occurs via grain boundary motion.[18] While it may be more appropriate to refer to the growth of the large crystals in Figures 4.4-4.6 as abnormal *crystal* growth, we adopt

the terminology of abnormal *grain* growth for continuity of the discussion with that of normal grain growth.

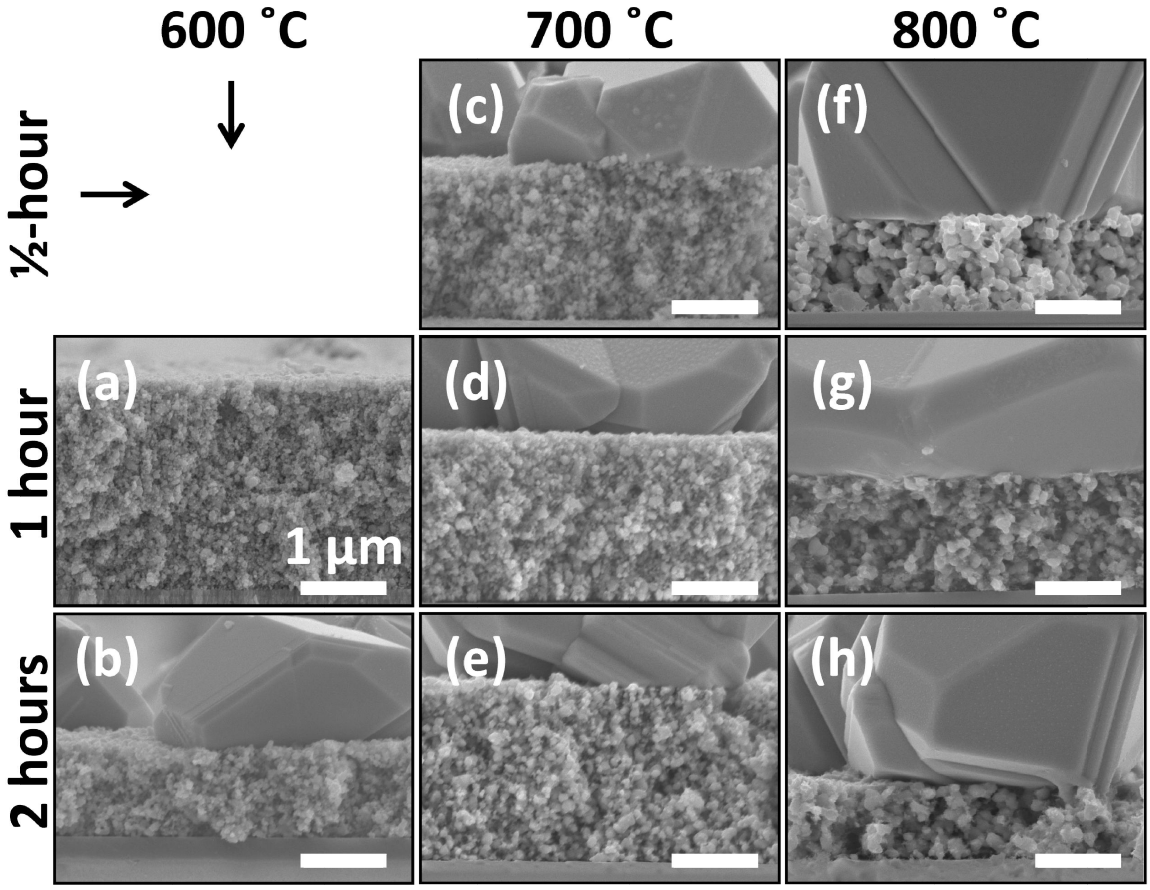

Figure 4.6 Cross-sectional SEM images of the films shown in Figures 4.4 and 4.6 (*i.e.*, CZTS nanocrystal films after annealing at (a-b) 600 °C, (c-e) 700 °C, (f-h) and 800 °C for 30 minutes, 1 hour, and 2 hours). All scale bars are 1 µm.

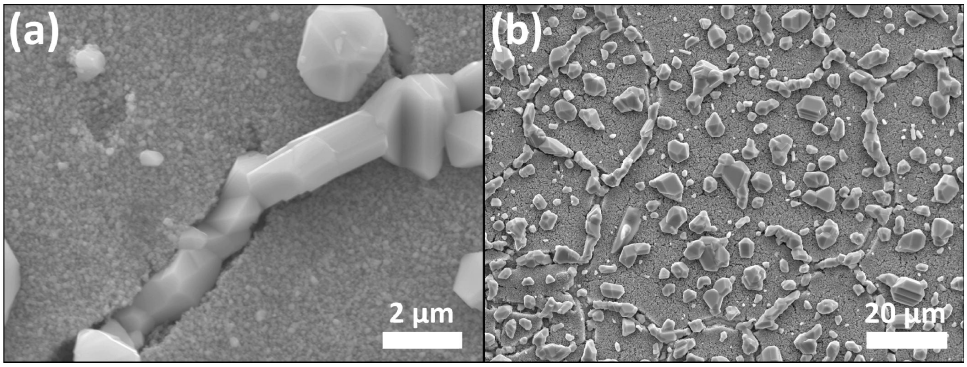

Figure 4.7 SEM images of annealed films showing abnormal CZTS crystals decorating preexisting cracks in the film (*i.e,*. stress-induced cracks that formed during the nanocrystal film deposition). These cracks form when the nanocrystal film is too thick and can be reduced by either decreasing the film thickness or by increasing the nanocrystal size. The film in (a) was annealed at 700 ˚C for 30 minutes and the film in (b) was annealed at 800 ˚C for 30 minutes.

These two competing mechanisms, normal and abnormal grain growth, control the film microstructure. Figures 4.4-4.6 clearly show that both normal and abnormal crystal growth take place during annealing of colloidal nanocrystal films in sulfur vapor. Hereafter, the large crystals on the surface are referred to as abnormal grains or abnormal crystals and the grains in the floor layer are referred to as the normal grains. For a given annealing time period (rows in Figures 4.4-4.6), the abnormal grain size, *d*, increases with annealing temperature. For a given annealing temperature (columns in Figures 4.4-4.6), the abnormal grains grow as a function of time. The average abnormal grain sizes were extracted from these SEMs and are plotted in Figure 4.8a as a function of growth time. The initial growth rate is rapid but then slows down significantly. The driving force for the initial fast growth of abnormal crystals appears to be the large surface area (and therefore total energy) associated with the colloidal nanocrystals. As the nanocrystals coarsen and begin to form necks, this large driving force is reduced and the abnormal crystal growth slows. Interparticle necks are clearly visible in Figure 4.6 at later stages of growth (*e.g.*, after 1 to 2 hours) especially in films annealed at 800 °C.

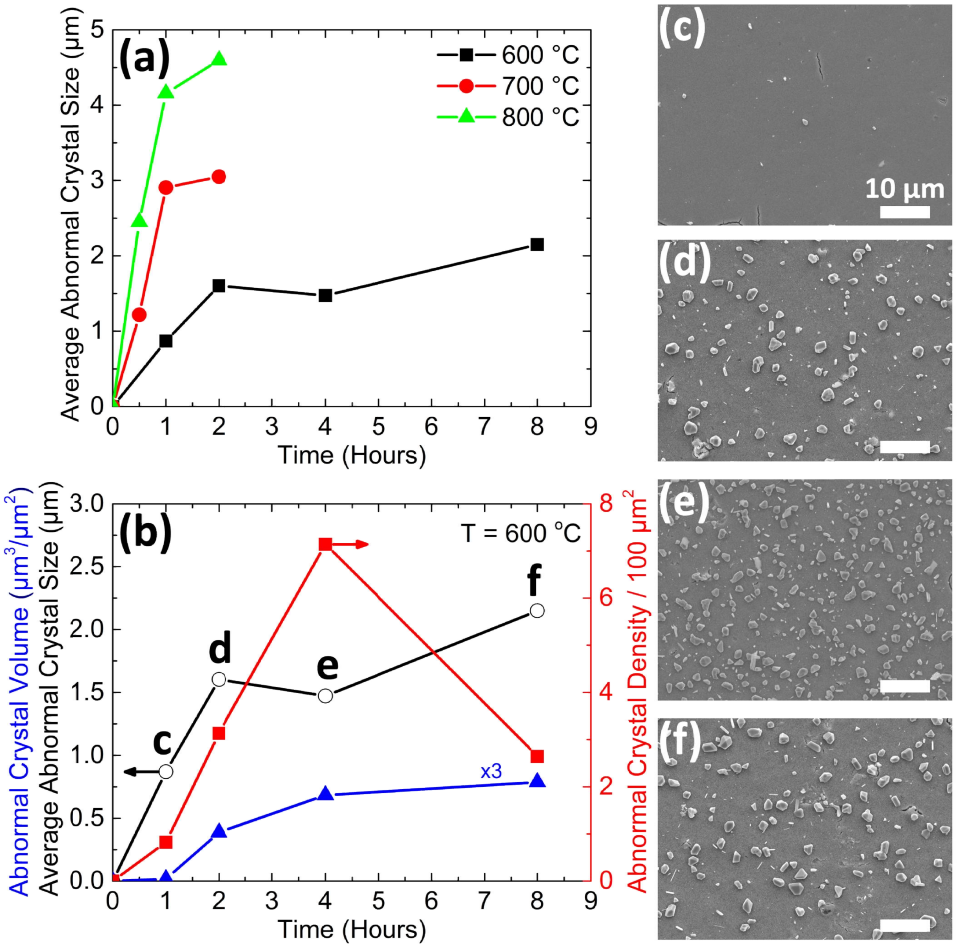

Figure 4.8 (a) Average abnormal crystal size as function of annealing time for films annealed at 600 °C, 700 °C, and 800 °C in ~50 Torr sulfur. (b) Average abnormal crystal size, average abnormal crystal density (crystals/100 µm^2), and average abnormal crystal volume (µm^3/µm^2) for films annealed at 600 °C as function of annealing time. (c-f) Plan view SEM images corresponding to the films annealed at 600 °C for 1, 2, 4, and 8 hours, respectively.

These annealing experiments were also repeated with nanocrystal films cast on Mo-coated (300 nm) quartz substrates. The CZTS film microstructures were identical to those on bare quartz, although the molybdenum layer peeled off the quartz in some cases (see Supporting Information Figures 4.9 and 4.10).

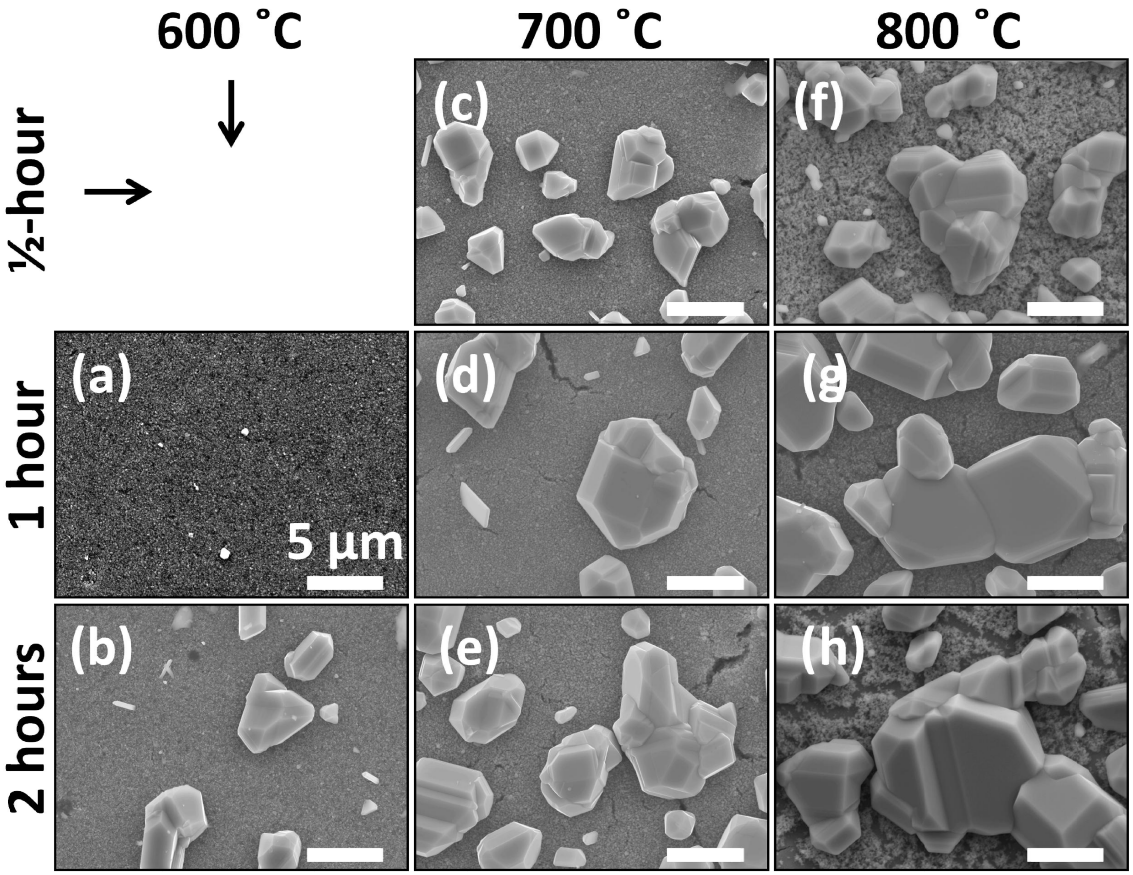

Figure 4.9 Plan view SEM images of the CZTS nanocrystal films, which were deposited on molybdenum-coated quartz (~300 nm of Mo), after annealing at (a-b) 600 °C, (c-e) 700 °C, (f-h) and 800 °C for 30 minutes, 1 hour, and 2 hours) in ~50 Torr of sulfur. All scale bars are 5 µm. The films are identical to those deposited on bare-quartz and annealed with the same conditions (*i.e.*, compare to Figure 2), except that the molybdenum layer delaminated from the quartz under some conditions (see Figure S5).

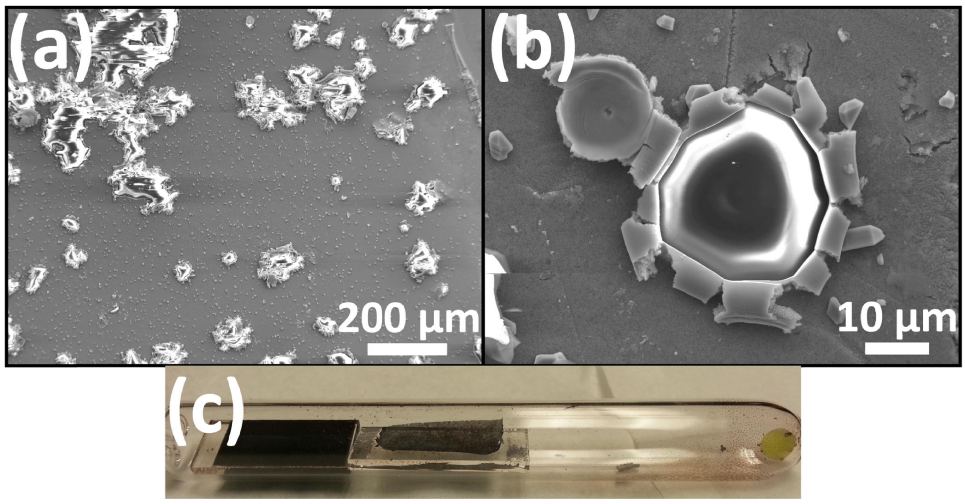

Figure 4.10 SEM images of CZTS films deposited on molybdenum-coated quartz and annealed at 600 ˚C for (a) 2 hours and (b) 4 hours in 50 Torr of sulfur. The molybdenum layer, together with the CZTS coating on top of it, delaminated from the quartz substrate under these conditions. Delamination occurred for films annealed for longer than 1 hour, at temperatures above 700 ˚C, or in ~500 Torr of sulfur (*e.g.*, image (c) shows that the film that had a molybdenum layer, on the right, delaminated after annealing at 600 ˚C with ~500 Torr of sulfur).

The temporal evolution of the size (d), number density (*N, i.e.,* grains/µm^2) of the abnormal grains and the quantity $N \times d^3$ *(i.e.,* µm^3/µm^2) gives insight into the microstructure development during annealing. (The quantity $N \times d^3$ is used as a measure of the abnormal grain volume per unit area.) These properties are plotted in Figure 4.8b as a function of growth time for films annealed at 600 °C. The dependence of the abnormal grain number density on annealing time is not monotonic. The abnormal grain density initially increases, reaches a maximum and then decreases. The initial rapid increase in abnormal grain density is driven by annihilation of high surface area, and therefore high total surface energy, nanocrystals via abnormal grain growth. The growth of large abnormal grains decreases the contribution of surfaces to the overall free energy of the film. Increasing grain density suggests that nucleation of abnormal grains continues to take place several hours into annealing and occurs on similar time scale as the growth.

Material from the nanocrystals is transported, likely through diffusion along the grain boundaries and the nanocrystal surfaces. There are two pieces of evidence that the source of material for abnormal crystal growth is the nanocrystals. First, as abnormal grains grow larger the floor thickness decreases (Figure 4.11). Second, cracks appear in the floor, which is most clearly evident in Figures 4.5f-h. For example, after 2 hours of

annealing at 800 °C, the nanocrystals in the floor layer have almost entirely been consumed such that the substrate beneath is visible. At the same time, the abnormal grains have grown as large as ~10 μm. Vapor phase transport is another possible mechanism that can move material from the floor to the abnormal grains. While SnS, Sn and Zn have significant vapor pressures at 600-800 °C, to our knowledge, there are no volatile Cu compounds that can transport Cu.[19,20] We believe that at least one of the cations (*e.g.,* Cu) must be transported by solid-state diffusion. If all cations were transported via vapor, and that the abnormal grains grew by a chemical vapor transport mechanism, we would see CZTS crystals on the quartz ampule walls. A careful examination of the broken ampules does not show any metal sulfides. This observation also rules out Zn vapor transport and we conclude that Zn is also incorporating into the abnormal grains via solid-state diffusion. We think that Sn may be the only cation that can be incorporated to the abnormal grains by vapor transport, most likely in the form of SnS.

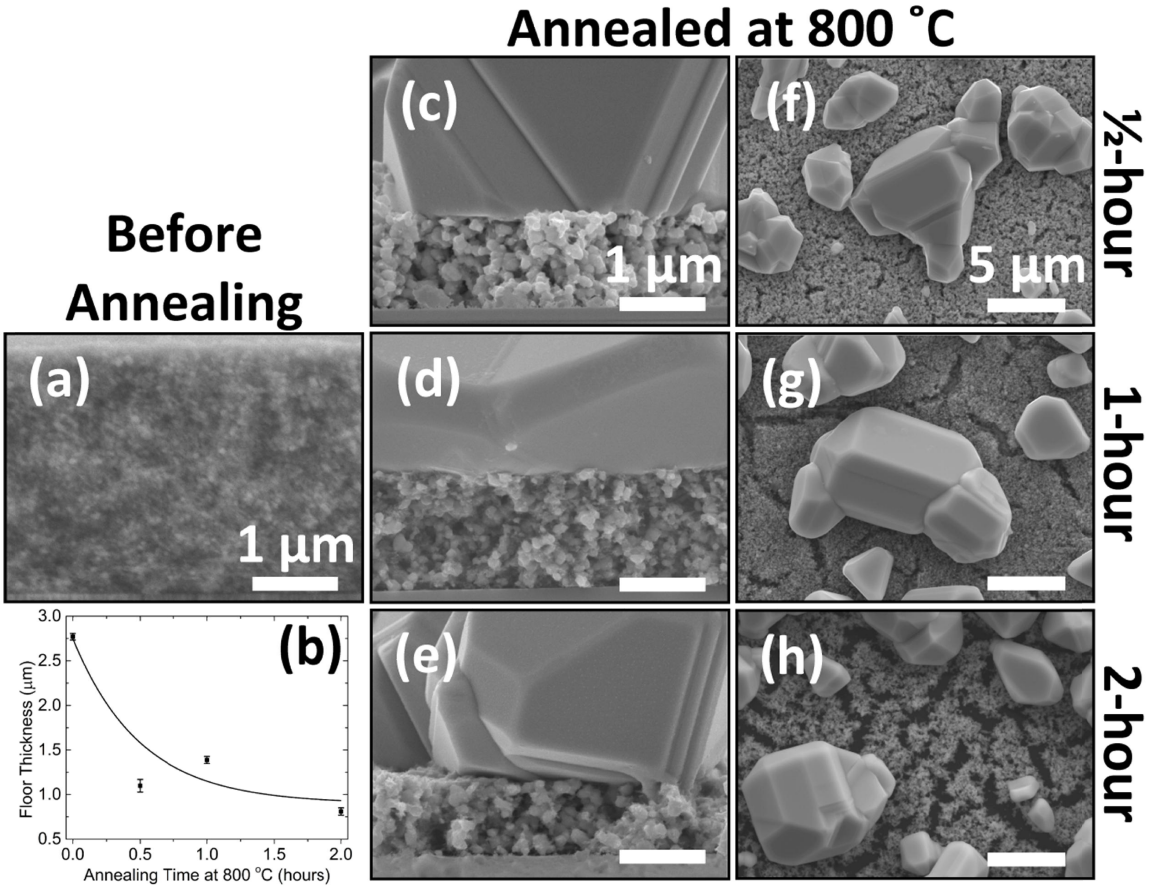

Figure 4.11 (a) Cross-section SEM images of CZTS nanocrystal films (a) before annealing and after annealing at 800 °C for (c) 30 minutes, (d) 1 hour, and (e) 2 hours. (b) Nanocrystal floor layer thickness versus annealing time, where t=0 represents the as-deposited film before annealing. Plan-view SEM images of the annealed films in (c), (d), and (e), are shown in (f), (g), and (h), respectively. The widening of voids that form in the floor layer is another piece of evidence that the material for abnormal grain growth is coming from the floor layer.

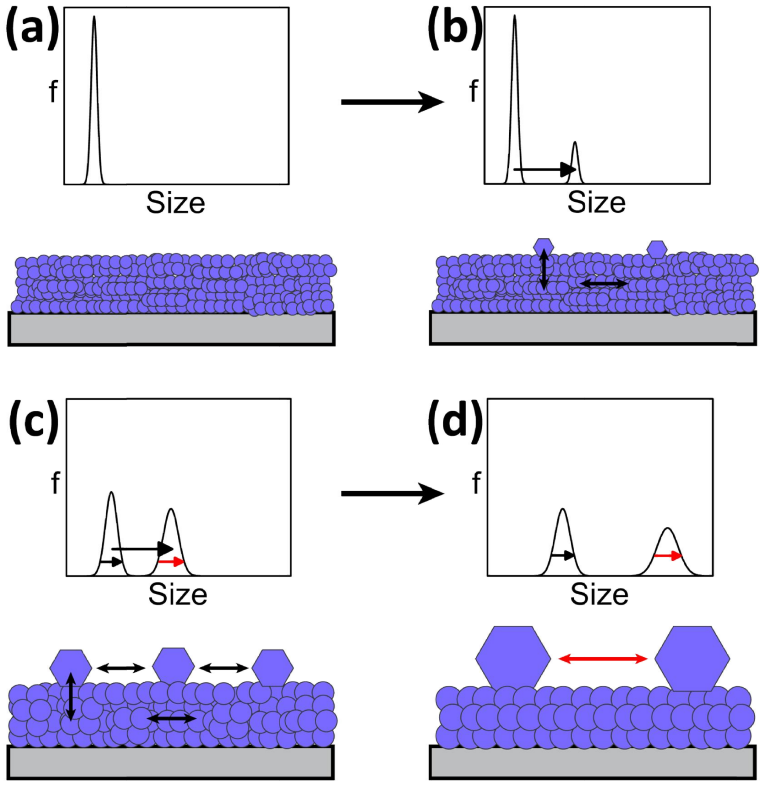

Figure 4.12 An illustration of the stages of microstructure development during the annealing of CZTS films. The top panels show the crystal size distribution, *f*, while the bottom panels illustrate the microstructure development and material transport (arrows). (a) Initial condition at t=0 with 25 nm nanocrystals. (b) Nucleation of abnormal crystals and development of a bimodal crystal size distribution. (c) Abnormal crystal growth at the expense of normal grains. (d) Abnormal and normal grain coarsening.

During the later stages of annealing, as shown in Figures 4.8b and 4.8f, the abnormal grain density decreases such that its product with the grain volume remains constant (*e.g.*, $N \times d^3$ = constant). This suggests that the material flux to the abnormal grains is reduced significantly after some time period (*e.g.,* after the grain density has reached a maximum) and the abnormal grains coarsen with time such that the total amount of material in the abnormal grains remains constant. These stages of microstructure evolution are illustrated in Figure 4.12. Abnormal grains nucleate and then grow to produce a bimodal crystal size distribution. Meanwhile the nanocrystals also coarsen and sinter. This reduces the nanocrystal surface area and both the thermodynamic driving force and the surface paths available for cation diffusion from the normal crystals to the abnormal crystals. Consequently, the abnormal grain growth slows. However, abnormal grain coarsening continues via material transport from the small abnormal

grains to the large ones. As a result, large abnormal grains grow larger while the smaller ones are annihilated. This reduces the abnormal grain density.

The presence of abnormal crystal growth in nanocrystal film annealing has important implications for producing thin films for solar cells via this approach. While abnormal crystal growth can lead to large grains, which are desirable for solar cells, it can also lead to grains much larger than the initial film thickness and, consequently, to voids in between the grains. The latter are undesirable because they can result in short circuiting between the solar cell's electrical contacts.

Earlier we asserted that both the floor and the abnormal grains are CZTS. This is an important issue, which we addressed using XRD and Raman microscopy. First, the XRD patterns from all the annealed films are consistent with CZTS and match ICDD-ref 04-005-0388 as shown in the bottom row of Figure 4.4 (c,g and k). Within the detection limits of XRD there were no other impurity phases present in the films. Diffraction peaks at 37.0° [(202)], 37.9° [(211)], and 44.9° [(105) and (213)] indicate the unambiguous presence of CZTS.[6] These diffractions are absent and very weak in ZnS and tetragonal Cu_2SnS_3, respectively. The presence of any significant amounts of ZnS and tetragonal Cu_2SnS_3 are ruled out using Raman spectroscopy. Importantly, two-dimensional XRD images show that diffraction spots from large abnormal grains are coincident with the diffraction rings from the nanocrystals that make up the floor (see Figure 4.13). This suggests that both the abnormal and normal grains are CZTS. The conclusive evidence comes from Raman imaging. Figure 4.14 compares the Raman spectra collected from the floor layer and the abnormal grains for films annealed at 600 °C, 700 °C and 800 °C. In all cases, both the floor layer and the large abnormal crystals on the surface exhibit the two strong characteristic CZTS Raman peaks at 337 cm^{-1} and 286-287 cm^{-1}.[11,21] A very weak peak at 495 cm^{-1} appears only in the floor layer of the films annealed at 600 °C, where the grains are very small and the internal surface area is high. Based on the Raman spectra of elemental sulfur allotropes we believe that this Raman peak is associated with sulfur on the surface of the nanocrystals.[15,22] As expected, the Raman peaks for the large (1-10 μm) crystals are sharper than the Raman peaks from the floor, which is comprised of 10-100 nm nanocrystals. Moreover, the elemental composition of the annealed films,

measured using EDS, matches that of the starting colloidal nanocrystal films, which, within the accuracy of the EDS measurements, were stoichiometric. Spatially resolved EDS also indicates that the CZTS stoichiometry of the floor layer and large abnormal grains are the same, though we detect carbon in the floor but not on the abnormal grains. Thus, all the characterization methods indicate that the films are nominally phase-pure stoichiometric CZTS and that there are no differences between the nanocrystals in the floor layer and the large abnormal grains except their size and morphology.

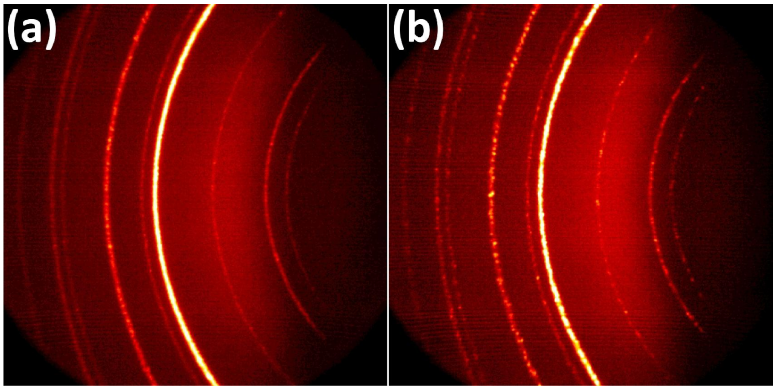

Figure 4.13 2D XRD images of CZTS films annealed for 2 hours at (a) 700 ˚C and (b) 800 ˚C in ~50 Torr S. The diffraction rings from the nanocrystalline floor layer are decorated with spots, which originate from the large abnormal crystals.

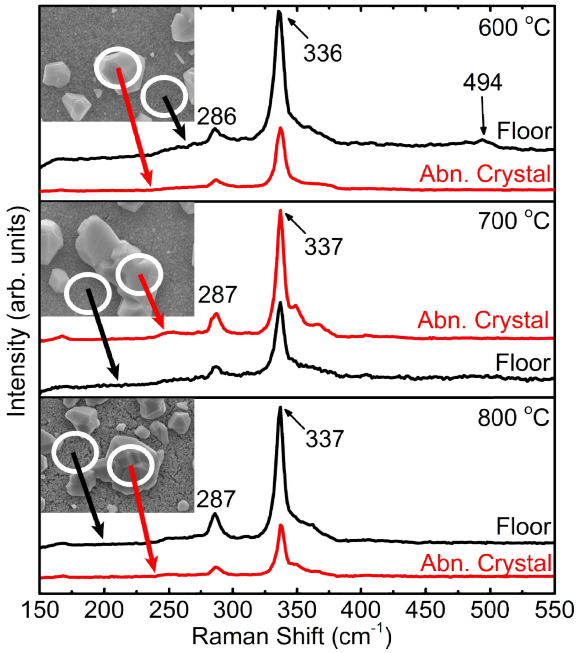

Figure 4.14 Raman spectra of the CZTS nanocrystal (normal grains) floor layer (black) and the CZTS abnormal crystals (red) for films annealed at 600 °C (top panel), 700 °C (middle panel), and 800 °C (bottom panel). The circles in the inset SEM images are ~3 µm in diameter.

4.3.2 Raman Scattering From Individual CZTS Microcrystals

On some films, the abnormal grains are large enough to excite and collect Raman scattering from individual facets. Spectra collected from individual facets explain some of the subtle features of the Raman spectra collected from an ensemble of CZTS grains. For example, the Raman spectra from the collection of abnormal grains in Figure 4.14b shows, in addition to the scattering at 337 cm^{-1} and 287 cm^{-1}, four additional peaks at 168 cm^{-1}, 251 cm^{-1}, 349 cm^{-1} and 366 cm^{-1}. The latter two peaks form the broad ~345-380 shoulder commonly observed in Raman spectra from films of CZTS, such as in the other spectra of Figure 4.14. When Raman scattering is collected from individual facets of a single very large crystal (*e.g.,* > 3 μm), each facet exhibits one of two types of spectra, nominally labeled "configuration 1" and "configuration 2." Raman spectra in configurations 1 and 2 are shown in Figure 4.15, as well as Supporting Information Figure 4.16, and appear to correspond to the combinations of A + B(TO) and A + B(LO) phonon modes of kesterite CZTS, respectively.[21,23] The signature peaks of the A mode, 338 cm^{-1} and 287 cm^{-1}, which are due to the anion lattice vibrations, are present in both spectra. In configuration 1, an intense and sharp (6 cm^{-1} FWHM) scattering is detected at 372 cm^{-1}. In configuration 2, there is no peak at 372 cm^{-1} but a new peak at 352 cm^{-1} appears. In contrast, the scattering at 352 cm^{-1} is completely absent from the spectra collected in configuration 1. Based on DFT calculations we assign these peaks at 352 cm^{-1} and 372 cm^{-1} to the B(TO) and B(LO) modes of kesterite CZTS, respectively.[21,23] Furthermore, the peak at 168 cm^{-1} is present in both configurations, as predicted for B(TO) and B(LO) modes.[21,23] Unfortunately, we do not know the orientations of the facets. However, comparing our spectra with the those from Dumcenco *et al.*[24] who studied polarization dependent Raman scattering from millimeter size single crystals, we infer that these two sets of phonon mode combinations may be observed from (100), (001) and (110) CZTS planes. Specifically, A+B(TO) modes are observed from (100) and (110) planes, whereas the A+B(LO) modes are observed from the (001) planes.

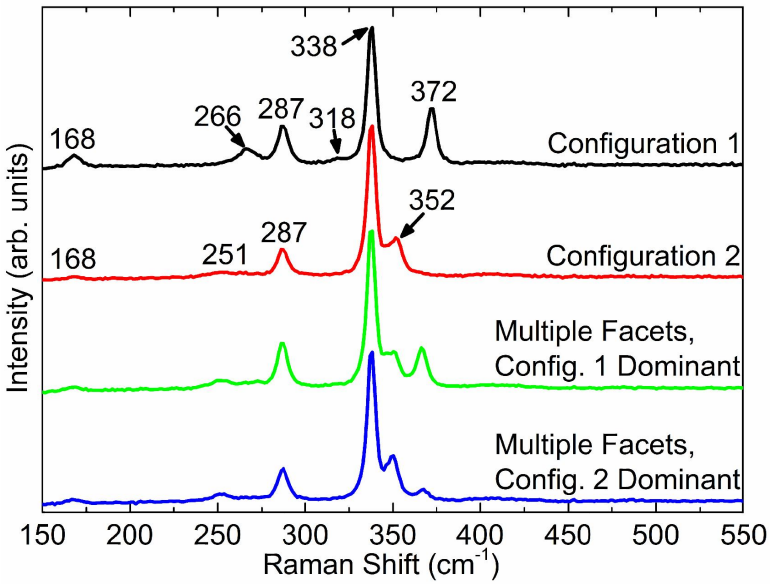

Figure 4.15 Raman spectra from individual facets of large (≥3 μm) abnormal crystals, collected using confocal Raman microscopy, produce one of two spectra, labelled configuration 1 and configuration 2. When Raman scattering is collected from an area including multiple facets, the resulting spectra reflect a combination of spectra labeled configuration 1 and configuration 2.

When the laser illuminates multiple crystal facets, the resulting Raman spectrum is a convolution of configuration 1 and configuration 2 spectra. For example, two additional Raman spectra are shown in Figure 4.15 where several crystal facets were illuminated. When Raman scattering is collected from a polycrystalline ensemble of abnormal grains, the spectra exhibit a combination of these modes. The relative intensities of the peaks are determined by the relative areas of the (100), (001) and (110) planes that are illuminated by the laser. For example, we show Raman spectra from two clusters of abnormal grains, one with a preponderance of (100) and (110) planes, where A+B(TO) modes dominate the spectra (*i.e.,* configuration 2), and another with a preponderance of (001) planes, where A+B(LO) modes dominate the spectra (*i.e.,* configuration 1).

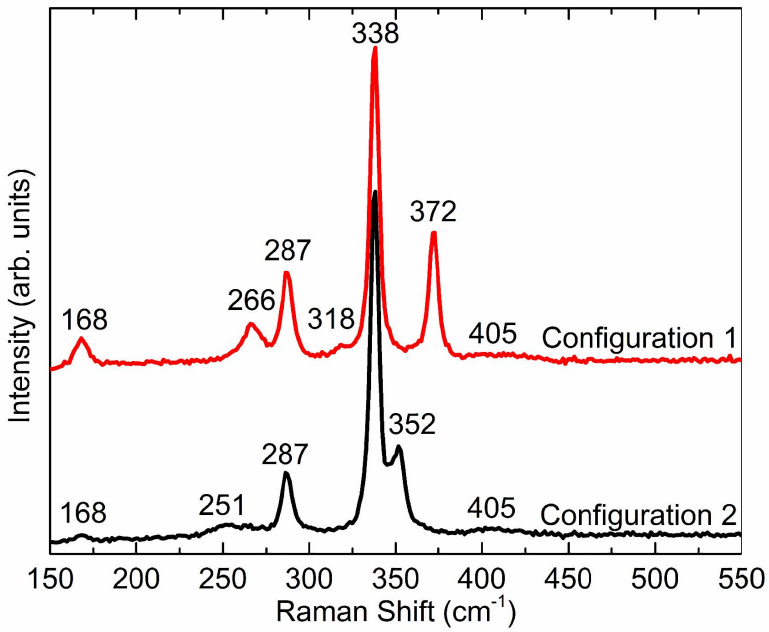

Figure 4.16 Raman spectra from facets of single CZTS crystals that are ≥ 3 μm in size.

The presence of (100), (001), and (110) planes on the surfaces of millimeter-scale single crystals of CZTS, grown by Dumcenco *et al.*,[24] suggests that these are thermodynamically stable, low energy facets of CZTS. Therefore, the observation of large facets of (100), (001), and (110) planes in Raman spectra of abnormal grains is consistent with the driving force for abnormal grain growth being the reduction in free surface energy of the system by the elimination of high energy surfaces in the nanocrystalline floor layer.

4.3.3 What Happens To the Carbon In the Ligands?

The carbon concentration in the films before and after annealing in sulfur is different. Before annealing, the films contain approximately 20-25 at.% carbon because the nanocrystals are covered with oleic acid and oleylamine ligands.[25] After annealing, the carbon concentration in the floor layer is reduced to 10-15%. Unlike the selenization experiments reported in literature,[26–28] where the carbon segregates into distinct layers between the CZTSe and the substrate, the carbon in our CZTS films appear to be distributed uniformly within the film. The oleic acid and oleylamine ligands adsorbed on nanocrystal surfaces may (i) evaporate, (ii) thermally decompose or (iii) react with sulfur. Both thermal decomposition and reactions with sulfur can produce volatile species, such

as low molecular weight hydrocarbons, CS_2, COS, H_2S, *etc.*, and remove carbon from the film. (COS may form due to the carboxylic acid group of oleic acid.) Indeed, during the first 15 minutes of annealing, a brown film deposits on the cold end of the quartz ampule. Elemental analysis of this brown film reveals predominantly carbon, with trace amounts of sulfur. The brown film eventually disappears. This suggests that the ligands on the nanocrystals decompose and the decomposition products condense as carbonaceous residue on the colder regions of the ampule. The color of the residue suggests that it is not oleylamine or oleic acid since these molecules are colorless. Subsequently, this carbonaceous residue may react with sulfur to form products such as CS_2 and COS, which are colorless vapors even at room temperature. Indeed, a faint but sulfurous odor is detectable when the ampule is broken suggesting the presence of volatile sulfur-containing species such as COS. In Appendix B.2, we calculate that there is almost two orders of magnitude more sulfur in the vapor inside the annealing ampule than necessary to convert all carbon in the films into CS_2. Therefore, it is likely that the carbon remaining in the film after annealing is due to the formation of non-volatile species as the result of thermal decomposition and/or reaction with sulfur vapor.

4.3.4 Effect of Sulfur Pressure

Increasing sulfur pressure in the annealing ampule accelerates CZTS crystal growth. CZTS nanocrystal films were annealed at 600 °C and 700 °C for one hour at 500 Torr, an order of magnitude higher than the sulfur pressure used for experiments discussed earlier. Figure 4.17 shows a side-by-side comparison of the microstructures of CZTS films annealed at ~50 Torr and at ~500 Torr for each of the annealing temperatures. At 600 °C, increasing the sulfur pressure from 50 Torr to 500 Torr increased the average abnormal crystal size, from 0.9 μm to 1.5 μm, and the abnormal grain density, from 0.8 grain/100 μm^2 to 5 grains/μm^2. The normal grains also grow faster at 500 Torr than at 50 Torr. The average normal grain size calculated from the full width at half maximum of the (112) XRD peak increased from 45 nm, for films annealed at 50 Torr, to beyond the instrumental limit of ~65 nm, for films annealed at 500 Torr. Cross-sectional SEM images also support that the normal grain size increased (Figure 4.17f and Figure 4.18). The XRD patterns and Raman spectra of the abnormal and the

normal grains match those expected from CZTS[21] (Figure 4.19). At 600 °C increasing the sulfur pressure appears to enhance both abnormal and normal grain growth rates.

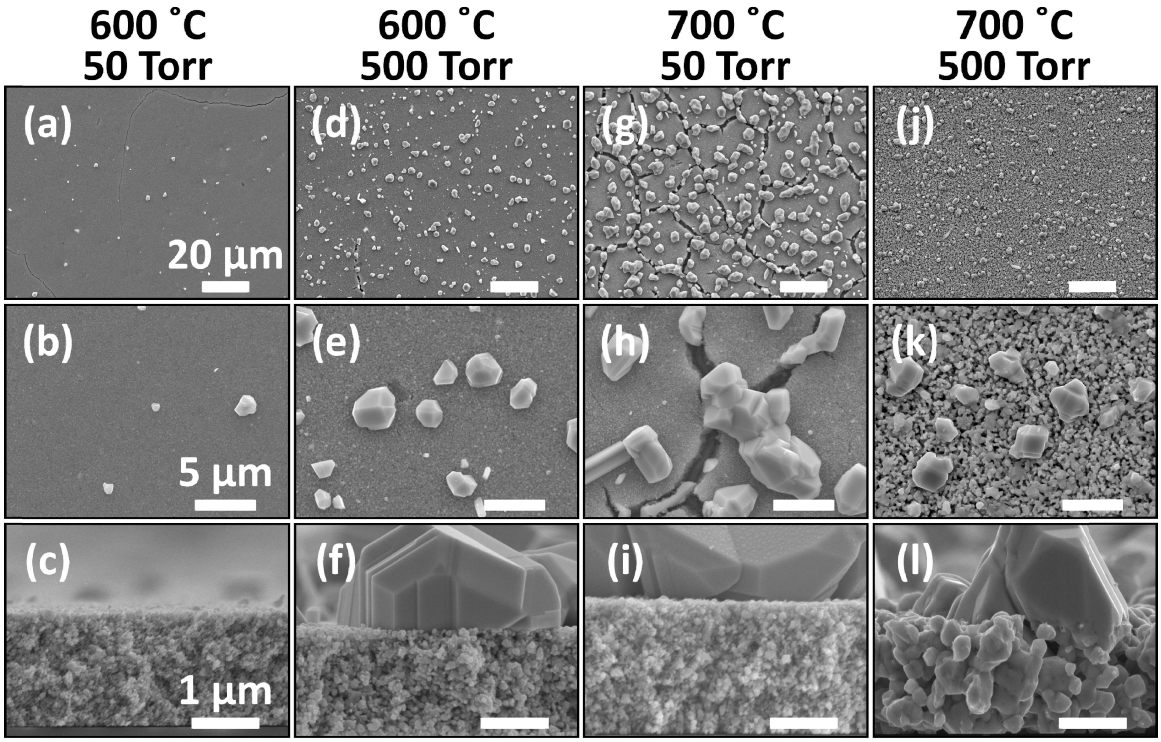

Figure 4.17 Plan view and cross-sectional SEM images comparing films annealed at low sulfur pressure (~50 Torr, a-c & g-i) and high sulfur pressure (~500 Torr, d-f & j-l) at 600 °C (a-f) and 700 °C (g-l). At both temperatures, increasing sulfur pressure accelerates crystal growth but the enhancement is more pronounced at 700 °C. All films shown in this figure were deposited on fused quartz and annealed for one hour. The scale bar lengths for all SEM images within each row are identical and given in the leftmost SEM image.

Normal and abnormal crystal growth are coupled, however. Abnormal grain growth is driven by the reduction in total energy associated with the smaller normal grain surfaces. Accelerating the normal grain growth can slow the abnormal crystal growth because this driving force is reduced. Indeed, at 700 °C, increasing the sulfur pressure increases the normal grain size significantly, from an average of 60 nm to ~400 nm, while the abnormal crystal size decreases from an average of 2.9 µm to 1.6 µm. The abnormal grain density at 500 Torr remains the same as that at 50 Torr. With rapid normal crystal growth becoming favorable throughout the film, annealing at 500 Torr and700 °C results in abnormal grains that appear to nucleate and grow from within the

nanocrystal layer (Figures 4.17j-l) rather than "float" above this layer as shown in the SEMs of films annealed at 50 Torr and 700 °C (Figures 4.17g-i).

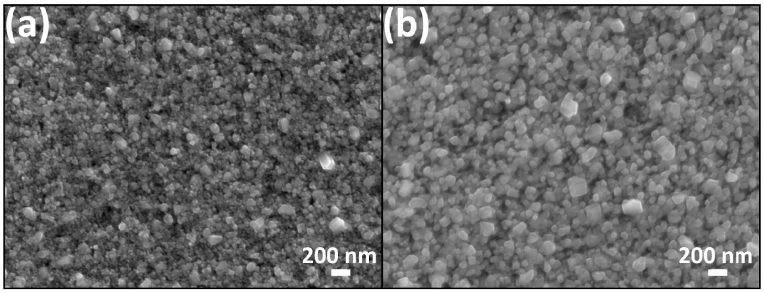

Figure 4.18 High magnification SEM images comparing the normal grain sizes in films annealed at 600 ˚C for one hour in (a) ~50 Torr S and (b) ~500 Torr S. The grains are larger in (b) the film annealed at 500 Torr of sulfur.

The mechanism by which sulfur enhances grain growth is difficult to isolate. There are two possibilities. Sulfur either increases the thermodynamic driving force for grain growth or accelerates the kinetics. For example, increasing the sulfur vapor pressure may remove carbon from the nanocrystal surfaces more effectively by forming volatile species such as CS_2 and COS. Solutes such as carbon are known to pin grain boundaries and inhibit grain growth.[29–31] Thus, removal of carbon can enhance grain growth. Indeed, EDS analysis of the films annealed at ~500 Torr shows lower carbon concentration than the films annealed at ~50 Torr, which would be consistent with faster carbon removal as a result of increased sulfur pressure. However, if we assume that the carbon resides primarily at grain surfaces, and since the total surface area of the large grains produced at ~500 Torr is smaller than that of the smaller grains produced at ~50 Torr, one would expect to see lower carbon concentration in the films with larger grains. Therefore, it is not certain whether the lower carbon concentration, as measured by EDS, indicates that carbon removal is the cause or the effect of enhanced grain growth in films annealed in ~500 Torr of sulfur. While removal of carbon may enhance grain growth during annealing of films cast from nanocrystal dispersions, it may not be the only mechanism.

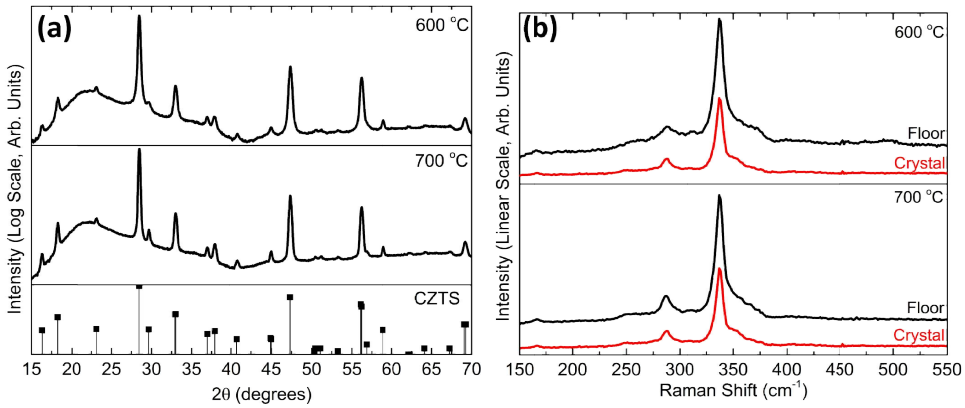

Figure 4.19 (a) XRD of CZTS films annealed in ~500 Torr of sulfur for one hour at 600 ˚C (top) and at 700 ˚C (bottom). (b) Raman spectra from the said films: the red lines are spectra collected from abnormal crystals and the black lines are spectra collected from the floor layer. The strongest two peaks in the Raman spectra are at 337 cm^{-1} and 287 cm^{-1}.

Another possibility is that increased sulfur pressure enhances the diffusion rate of the anion or the cation that limits the grain growth. For example, in sintering of oxides oxygen anion diffusion typically limits the grain growth.[32–34] A similar situation may exist in CZTS where the sulfur diffusion limits the grain growth. Indeed, it has been shown in sulfide compounds such as ZnS, Cu_2S, CdS and Ag_2S that sulfur diffusion is slower than that of the cations.[35–37] The CZTS unit cell is virtually identical in structure and in size to two ZnS unit cells stacked on top of each other. Thus, we expect sulfur to be the slowest diffusing species in CZTS as well. In that case, the availability of sulfur from the vapor phase would increase the sulfur transport rates. Indeed, the sulfur in the vapor is in a dynamic equilibrium with the sulfur in the CZTS grains: this is implied by successful conversion of CZTS to CZTSSe when CZTS nanocrystals are exposed to selenium vapor.[8,26] Therefore, increasing sulfur pressure may enhance coarsening and grain growth by accelerating solid diffusion of sulfur, the rate limiting species.

Moreover, during sintering of some oxides, such as Cr_2O_3, an increase in oxygen partial pressure enhances sintering by evaporation/condensation processes at the expense of densification.[38] This results in neck growth and coarsening but porous microstructures, such as that shown in Figure 4.17l. It appears that similar sulfur pressure-dependent evaporation/condensation processes can be important in CZTS microstructure development during annealing in presence of high sulfur vapor pressure.

The above mechanisms, for enhancement of crystal growth by sulfur vapor, can explain the reason for abnormal crystal nucleation and growth at the top surface of the nanocrystal floor layer. The top surface of the floor layer sees a higher sulfur vapor concentration, at least initially. During the initial stages of annealing, abnormal crystals may nucleate on the top surface of the floor because carbon would be removed from these locations first. Similarly, the acceleration of solid diffusion or evaporation/condensation processes would occur at these top surfaces first. A combination of these processes may also be responsible for the enhanced grain growth.

4.3.5 Effect of the Substrate

Under otherwise identical conditions, CZTS films annealed on SLG had larger normal grains than the films annealed on quartz or Mo-coated quartz. Figure 4.20 compares the SEMs of CZTS films annealed on SLG to those annealed on quartz at 600 °C for two different sulfur vapor pressures. Even at 600 °C and 50 Torr, there is a significant difference between films annealed on SLG and those annealed on quartz. The film on SLG is a homogenous, dense layer of 200-500 nm (250 nm average size) normal grains with occasional (~2 grains/100 μm^2) abnormal grains (~1 μm in size on average) embedded within these 200-500 nm normal grains (see Supporting Information Figure 4.21 for additional SEMs). Figure 4.22 shows XRD patterns and Raman spectra, which are consistent with that of CZTS, for the films annealed on SLG The carbon concentration in the film is reduced from 20-25%, before annealing, to 10%, after annealing. Thus, some of the carbon is removed from the films during annealing and the remaining carbon does not appear to inhibit grain growth on SLG. It is well known that Na diffusion from SLG into copper indium gallium selenide (CIGS) films enhances grain growth.[39–43] Recently, impurities, in particular Na and K, from SLG have been shown to diffuse into CZTS and enhance grain growth in this material as well.[44] Other experiments where Na-free substrates were coated with Na-containing compounds, such as NaF, confirm the role of Na in improving the grain size in CIGS and CZTS films.[45–47] Thus, we attribute the enhanced normal grain growth during annealing of nanocrystal coatings to impurities from SLG. Several hypotheses to explain enhanced grain growth have been proposed[48–51] though the precise mechanism is still not known.

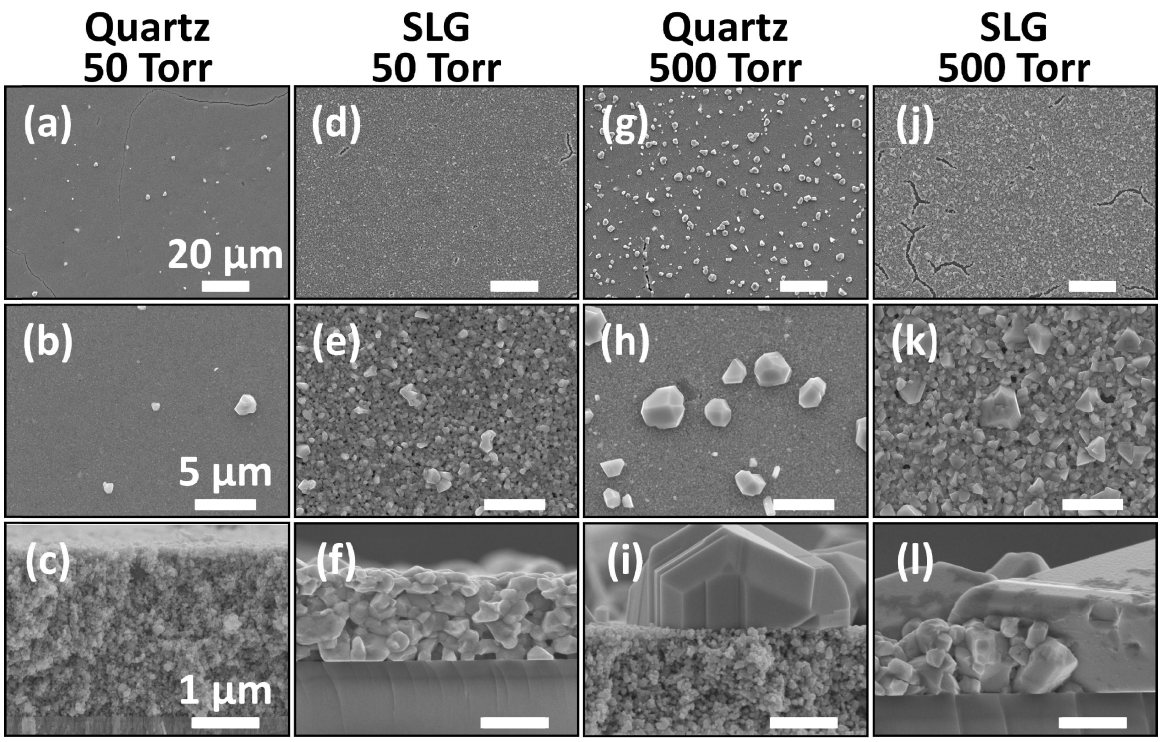

Figure 4.20 Plan view and cross-sectional SEM images of CZTS films annealed on fused quartz (a-c & g-i) and on soda lime glass (d-f & j-l) at low sulfur pressure (~50 Torr, a-f) and high sulfur pressure (~500 Torr, g-l). Substrate impurities from soda lime glass accelerate normal crystal growth. All films shown in this figure were annealed at 600 °C for one hour. The scale bar lengths for all SEM images within each row are identical and given in the leftmost SEM image.

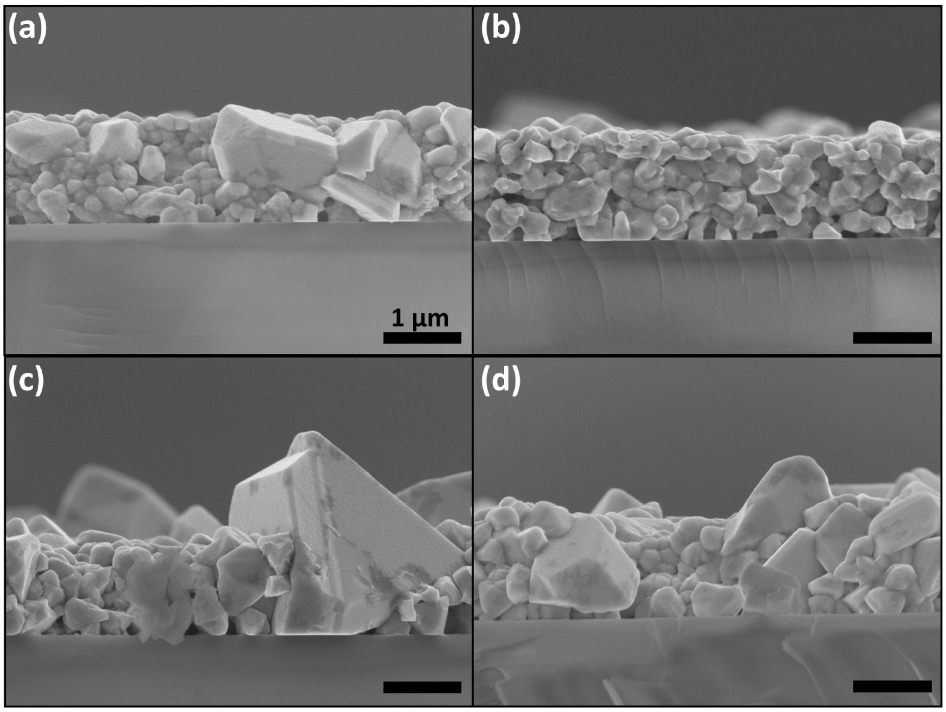

Figure 4.21 SEM images of CZTS films deposited on SLG and annealed for one hour at 600 ˚C in (a & b) ~50 Torr and (c & d) ~500 Torr of sulfur. All scale bars are 1 μm.

The combination of increased sulfur pressure and substrate impurities enhances both normal and abnormal grain growth. After annealing at 600 °C with 500 Torr of sulfur, the average normal and abnormal grain sizes on SLG were 350 nm and 2 μm, respectively. In contrast the average normal and abnormal grains on quartz, at the same temperature and sulfur pressure, were ~65 nm and 1.5 μm, respectively. Same size grains grow at lower temperatures on SLG than on quartz. On quartz, both high sulfur pressure (500 Torr) and high temperatures (700 °C) are necessary to grow normal grains that are several hundreds of nanometers in size. In contrast, similar size (≥300 nm) grains can grow on SLG at lower temperatures (600 °C) and sulfur pressure (50 Torr). Thus, impurities reduce both the temperature and sulfur pressure required to grow large grains.

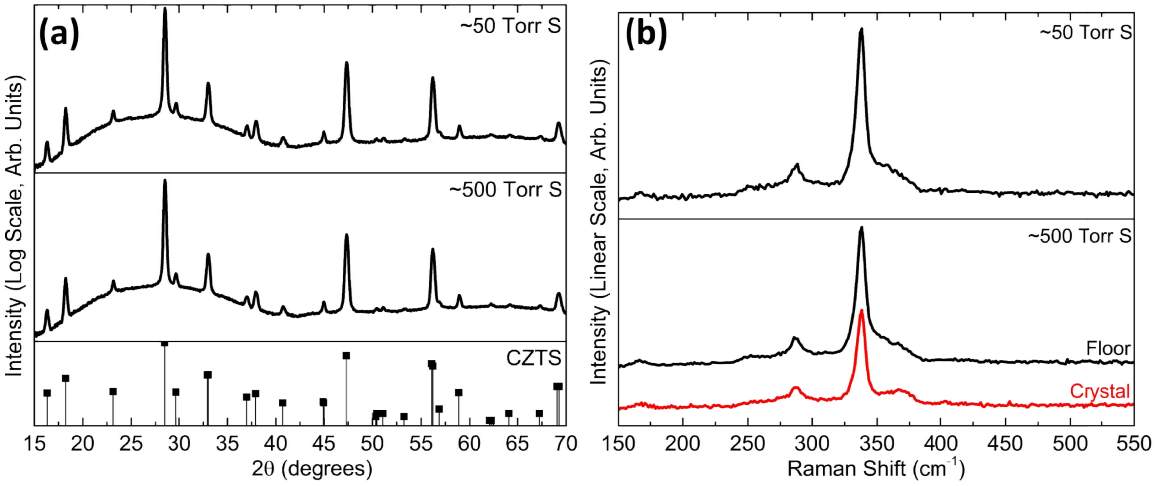

Figure 4.22 (a) XRD and (b) Raman spectra from CZTS films deposited on SLG and then annealed at 600 °C for one hour in ~50 Torr and ~500 Torr of sulfur. Both data sets are consistent with CZTS. The two strongest peaks in all Raman spectra are at 338 cm^{-1} and 288 cm^{-1}.

4.4 Conclusions

In summary, we show the effects of varying the annealing temperature, time, and sulfur vapor pressure on the microstructure of CZTS nanocrystal films cast on fused quartz, an impurity-free substrate, and SLG, which contains metals (*i.e.*, Na and K) that are impurities with respect to CZTS. Two competing mechanisms influence the film microstructure: normal grain growth and abnormal grain (more appropriately, *crystal*) growth. The nanocrystals in the film undergo normal grain growth to several hundred nanometers while large single-crystal CZTS grains grow rapidly on the film surface, up to 10 microns in size. These large abnormal CZTS crystals grow by transport of material from the nanocrystal layer. The abnormal grain growth is driven by the surface area and total energy difference between the nanocrystals and the large abnormal crystals. Increasing annealing time eventually leads to a reduction of this driving force as the nanocrystals coarsen. Increasing the sulfur pressure significantly enhances grain growth. The introduction of impurities via the use of SLG substrates accelerates normal grain growth at lower temperatures (600 °C) than necessary to grow similar size grains on quartz (700 °C). While the film morphology affects light scattering, all films absorb strongly above ≈1.5 eV, the band gap of CZTS (Figure 4.23). We are currently making solar cells to understand the effect of microstructure on the electronic properties relevant to solar cells.

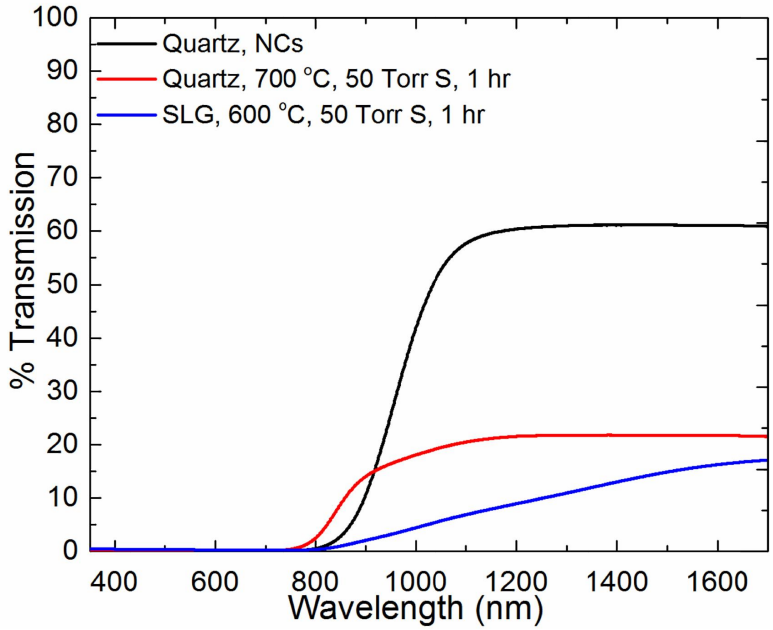

Figure 4.23 Optical transmission for three types of films: (1) an as-deposited nanocrystal film (black), (2) a film with large abnormal crystals on quartz (red) and (3) a film on SLG with normal grain sizes (blue), on the order of one micron. All films show decrease in transmission at around ≈800 nm consistent with absorption onset above ≈1.5 eV, the band gap of CZTS. Data is uncorrected for reflection and transmission. The transmission loss at long wavelengths (below the band gap energy) is due to reflection and scattering.

4.5 References

1. K. Ito and T. Nakazawa, *Jpn. J. Appl. Phys.*, 1988, **27**, 2094–2097.

2. C. A. Wolden, J. Kurtin, J. B. Baxter, I. Repins, S. E. Shaheen, J. T. Torvik, A. A. Rockett, V. M. Fthenakis, and E. S. Aydil, *J. Vac. Sci. Technol. A*, 2011, **29**, 030801.

3. W. Wang, M. T. Winkler, O. Gunawan, T. Gokmen, T. K. Todorov, Y. Zhu, and D. B. Mitzi, *Adv. Energy Mater.*, 2013, 10.1002/aenm.201301465.

4. K. Wang, O. Gunawan, T. Todorov, B. Shin, S. J. Chey, N. A. Bojarczuk, D. Mitzi, and S. Guha, *Appl. Phys. Lett.*, 2010, **97**, 143508.

5. I. Repins, C. Beall, N. Vora, C. DeHart, D. Kuciauskas, P. Dippo, B. To, J. Mann, W.-C. Hsu, A. Goodrich, and R. Noufi, *Sol. Energ. Mat. Sol. C.*, 2012, **101**, 154–159.

6. A.-J. Cheng, M. Manno, A. Khare, C. Leighton, S. A. Campbell, and E. S. Aydil, *J. Vac. Sci. Technol. A*, 2011, **29**, 051203.

7. H. Katagiri, N. Sasaguchi, S. Hando, S. Hoshino, J. Ohashi, and T. Yokota, *Sol. Energ. Mat. Sol. C.*, 1997, **49**, 407–414.

8. H. W. Hillhouse and M. C. Beard, *Curr. Opin. Colloid Interface Sci.*, 2009, **14**, 245–259.

9. V. A. Akhavan, B. W. Goodfellow, M. G. Panthani, C. Steinhagen, T. B. Harvey, C. J. Stolle, and B. A. Korgel, *J. Solid State Chem.*, 2012, **189**, 2–12.

10. Q. Guo, H. W. Hillhouse, and R. Agrawal, *J. Am. Chem. Soc.*, 2009, **131**, 11672–11673.

11. A. Khare, A. W. Wills, L. M. Ammerman, D. J. Norris, and E. S. Aydil, *Chem. Commun.*, 2011, **47**, 11721–11723.

12. Q. Guo, G. M. Ford, W.-C. Yang, B. C. Walker, E. A. Stach, H. W. Hillhouse, and R. Agrawal, *J. Am. Chem. Soc.*, 2010, **132**, 17384–17386.

13. D.-Y. Peng and J. Zhao, *J. Chem. Thermodyn.*, 2001, **33**, 1121–1131.

14. H. Rau, T. R. N. Kutty, and J. R. F. Guedes De Carvalho, *J. Chem. Thermodyn.*, 1973, **5**, 833–844.

15. B. Meyer, *Chem. Rev.*, 1976, **76**, 367–388.

16. C. V. Thompson, *J. Appl. Phys.*, 1985, **58**, 763–772.

17. C. V Thompson, *Annu. Rev. Mater. Sci.*, 1990, **20**, 245–268.

18. M. W. Barsoum, in *Fundamentals of Ceramics*, Taylor & Francis, Boca Raton, Florida, 2002, pp. 302–355.

19. C. L. Yaws, P. Narasimhan K., and C. Gabbula, *Yaws' Handbook of Antoine Coefficients for Vapor Pressure*, Knovel, 2nd edn., 2009.

20. D. J. Chakrabarti and D. E. Laughlin, *Bull. Alloy Phase Diagrams*, 1983, **4**, 254–271.

21. A. Khare, B. Himmetoglu, M. Johnson, D. J. Norris, M. Cococcioni, and E. S. Aydil, *J. Appl. Phys.*, 2012, **111**, 083707.

22. X. Zhang, M. Manno, A. Baruth, M. Johnson, E. S. Aydil, and C. Leighton, *ACS Nano*, 2013, **7**, 2781–2789.

23. T. Gürel, C. Sevik, and T. Çağın, *Phys. Rev. B*, 2011, **84**, 205201.

24. D. Dumcenco and Y. Huang, *Opt. Mater.*, 2013, **35**, 419–425.

25. B. S. Tosun, B. D. Chernomordik, A. Gunawan, B. Williams, K. A. Mkhoyan, L. F. Francis, and E. S. Aydil, *Chem. Commun.*, 2013, **49**, 3549–3551.

26. R. Mainz, B. C. Walker, S. S. Schmidt, O. Zander, A. Weber, H. Rodriguez-Alvarez, J. Just, M. Klaus, R. Agrawal, and T. Unold, *Phys. Chem. Chem. Phys.*, 2013, **15**, 18281.

27. Q. Guo, G. M. Ford, W.-C. Yang, C. J. Hages, H. W. Hillhouse, and R. Agrawal, *Sol. Energ. Mat. Sol. C.*, 2012, **105**, 132–136.

28. C. M. Fella, A. R. Uhl, Y. E. Romanyuk, and A. N. Tiwari, *Phys. Status Solidi A*, 2012, **209**, 1043–1048.

29. F. Liu and R. Kirchheim, *J. Cryst. Growth*, 2004, **264**, 385–391.

30. F. Humphreys and M. Hatherly, in *Recrystallization and Related Annealing Phenomena*, ed. D. Sleeman, Elsevier Ltd, Oxford, Kidlington, UK, 2nd edn., 2004, pp. 368–378.

31. F. Inam, H. Yan, T. Peijs, and M. J. Reece, *Compos. Sci. Technol.*, 2010, **70**, 947–952.

32. W. J. Moore and E. L. Williams, *Discuss. Faraday Soc.*, 1959, **28**, 86–93.

33. W. C. Hagel, P. J. Jorgensen, and D. S. Tomalin, *J. Am. Ceram. Soc.*, 1966, **49**, 23–26.

34. C. Ting and H. Lu, *J. Am. Ceram. Soc.*, 1999, **82**, 841–848.

35. T. Bansagi, E. A. Secco, O. K. Srivastava, and R. R. Martin, *Can. J. Chem.*, 1968, **46**, 2881–2886.

36. C. E. Birchenall, in *Geochemical Transport and Kinetics*, eds. A. W. Hofmann, B. J. Giletti, H. S. J. Yoder, and R. A. Yund, Carnegie Institution of Washington, 1974, pp. 53–59.

37. D. A. Stevenson, in *Atomic Diffusion in Semiconductors*, ed. D. Shaw, Springer US, Boston, MA, 1973, pp. 431–541.

38. M. N. Rahaman, in *Ceramic Processing and Sintering*, ed. M. N. Rahaman, CRC Press, New York, 2nd edn., 2003, pp. 800–815.

39. S.-H. Wei, S. B. Zhang, and A. Zunger, *J. Appl. Phys.*, 1999, **85**, 7214–7218.

40. D. Schmid, M. Ruckh, and H. Schock, *Sol. Energ. Mat. Sol. C.*, 1996, **41-42**, 281–294.

41. D. Braunger, D. Hariskos, G. Bilger, U. Rau, and H. W. Schock, *Thin Solid Films*, 2000, **361-362**, 161–166.

42. A. Rockett, J. S. Britt, T. Gillespie, C. Marshall, M. M. Al Jassim, and F. Hasoon, *Thin Solid Films*, 2000, **372**, 212–217.

43. T. Prabhakar and N. Jampana, *Sol. Energ. Mat. Sol. C.*, 2011, **95**, 1001–1004.

44. M. Johnson, S. V. Baryshev, E. Thimsen, M. Manno, X. Zhang, I. V. Veryovkin, C. Leighton, and E. S. Aydil, *Energy Environ. Sci.*, 2014, 10.1039/c3ee44130j.

45. K. Granath, M. Bodegård, and L. Stolt, *Sol. Energ. Mat. Sol. C.*, 2000, **60**, 279–293.

46. D. Rudmann, G. Bilger, M. Kaelin, F.-J. Haug, H. Zogg, and A. N. Tiwari, *Thin Solid Films*, 2003, **431-432**, 37–40.

47. W. M. Hlaing Oo, J. L. Johnson, A. Bhatia, E. A. Lund, M. M. Nowell, and M. A. Scarpulla, *J. Electron. Mater.*, 2011, **40**, 2214–2221.

48. L. Kronik, D. Cahen, and H. W. Schock, *Adv. Mater.*, 1998, **10**, 31–36.

49. D. W. Niles, K. Ramanathan, F. Hasoon, R. Noufi, B. J. Tielsch, and J. E. Fulghum, *J. Vac. Sci. Technol. A*, 1997, **15**, 3044–3049.

50. A. Rockett, *Thin Solid Films*, 2000, **362**, 330–337.

51. D. Rudmann, Ph.D. Thesis, Swiss Federal Institute of Technology (ETH) Zürich, 2004.

CHAPTER 5

Microstructure Evolution During Selenization of Cu_2ZnSnS_4 Colloidal Nanocrystal Coatings

5.1 Introduction

Great progress has been made in the power conversion efficiencies (PCEs) of solar cells based on copper zinc tin sulfoselenide [$Cu_2ZnSn(S_xSe_{1-x})_4$, or CZTSSe] within a short period of time: from a 2.67% CZTS solar cell in 2001[1] to a 12.6% CZTSSe solar cell in 2013.[2] PCE is a critical solar cell figure of merit to determine market-readiness of a photovoltaic technology. An equally, if not more, important economic figure of merit is cost in the cost of manufacturing: this cost includes both the capital cost to set up a manufacturing plant and the operating costs. Using vacuum deposition 7-9.2% efficient solar cells have been demonstrated.[3,4] However, vacuum-based manufacturing methods are expensive. Significant obstacles to lowering capital and operating costs of vacuum deposition methods are low throughput (low growth rates) and low material utilization (high material waste). Solution-based approaches are compelling alternatives because they have the potential for high throughput at low cost, although material-related capital and operating expenses will vary with each method. As discussed in Chapter 2, some solution-based methods are referred to as sol-gel,[5] electrodeposition,[6] colloidal nanocrystals,[7,8] alcohol slurry,[9] hydrazine slurry,[2] and molecular-ink.[10,11] The absorber films for the highest PCE solar cells have been synthesized using slurries of metalorganic precursors in hydrazine, but this approach has the significant drawback of relying on a highly toxic and dangerous solvent that may translate to high capital and operating expenses as well as safety concerns.

In the approach where films are deposited from colloidal dispersions of CZTS nanocrystals, the material synthesis and the deposition are separated into two steps: the thermodynamically stable CZTS nanocrystals are formed before deposition onto a substrate. The deposited nanocrystal coatings contain organic ligands. In Chapter 2, we showed that that carbon can be volatilized and removed from the film during sulfidation to form CZTS thin films.[12] However, more research efforts have been directed toward selenization of nanocrystal films to form CZTSSe because the lower vapor pressure of selenium is more amenable to open-system annealing techniques and because CZTSSe[2] and CZTSe[3] solar cells have been outperforming those based on CZTS.[13] The reasons for the latter empirical observations are not clear but they may be related to changes in the buffer-absorber layer band edge offset[14] (*i.e.*, cliff versus spike) or to decreasing concentration of electron recombination centers with the addition of selenium.[15] When coatings from CZTS nanocrystals are annealed in selenium to form polycrystalline CZTSSe films, a carbon rich layer forms at the interface between the CZTS film and the substrate.[16] This bilayer microstructure is a consequence of the segregation of carbon to the region between the CZTS grains and the substrate instead of desorbing from the surface as volatile products such as CSe_2. The carbon originates from the ligands decorating the nanocrystal surfaces in the dispersion. This carbon segregation and the resulting bilayer microstructure have also been observed in other solution based film synthesis approaches where carbon containing ligands or precursors were present.[17,18]

Continued improvements in the solar cell performance and cost reduction, require a fundamental understanding of the factors that must be balanced to obtain a film morphology that provides charge carrier transport across the film with minimal scattering and trapping at the grain boundaries. Amidst the understandable rush to make incremental improvements to the CZTSSe solar cell PCE benchmark, systematic exploration of the key process variables that control microstructure development in CZTSSe thin films during selenization of CZTS nanocrystals has been neglected. Herein, we use isothermal annealing of CZTS nanocrystal coatings in a closed system to investigate the roles of selenium vapor pressure, annealing temperature, and heating rate in the formation of polycrystalline CZTSSe thin films. The closed system annealing approach provides a well-defined and reproducible annealing environment with known

selenium vapor pressure and temperature, eliminating complications such as Sn-loss and unknown transients in the selenium vapor pressure. We show that under some selenization conditions, CZTS nanocrystals selenize, grow, sinter, and densify without the formation of a carbon-rich layer between the CZTSSe film and the substrate. Our experiments suggest that the carbon-rich layer formation between the CZTSSe film and the substrate is due to the tendency of CSe_2 to polymerize and not due to trapping of carbon by the growing grains as has been suggested previously.[16,19,20]

5.2 Experimental

The colloidal CZTS nanocrystal dispersions were prepared using the synthesis methods discussed in detail in Chapter 3. In summary, stoichiometric CZTS nanocrystals were synthesized by dissolving copper, zinc, and tin-diethyldithiocarbamate precursor powders in oleic acid at 140 ^{o}C. After dissolution, the precursor mixture was then injected into a separate flask containing oleylamine heated to 280 ^{o}C. After growth for 10 minutes, the reaction solution was cooled and the nanocrystals were crashed by adding ethanol followed by centrifugation. After two washing steps, the particles were finally dispersed in toluene to a concentration of 30 mg/mL. The nanocrystals were then drop cast onto blank quartz substrates. We focus on quartz substrates as a proxy for alternative substrates and back contacts, such as flexible metal foils, which allow for a wider range of processing temperatures than Mo-coated soda lime glass (SLG). Using quartz also simplifies the system by eliminating the role alkali-metal impurities. However, select experiments were also conducted using SLG as the substrate to demonstrate that some microstructures could be reproduced on SLG as well as on quartz. The nanocrystals were ~25 nm in diameter as calculated from the width of the (112) X-ray diffraction peak using the Scherrer equation.

The annealing procedure is discussed in detail in Chapter 4. In summary, the CZTS nanocrystal-coated quartz substrates were placed inside of a quartz tube with a predetermined mass of selenium. The calculation of selenium vapor pressure inside the ampule is discussed below and also in Appendix B.1. The tube was evacuated to ~10^{-6} Torr and flame-sealed to produce a sealed ampule. The film is then annealed in one of two ways hereafter referred to as the slow-ramping method and the hot loading method.

In the slow-ramping method, the ampule is inserted into a cavity in an alumina block placed inside the furnace. Initially, the furnace, alumina block, and the ampule are at room temperature. The furnace is then turned on and the temperatures is increased at 6 ^{o}C/min to the desired annealing temperature set point (*i.e.*, 600 or 700 ^{o}C in the experiments described herein). After one hour at the final temperature, the oven is turned off and the furnace, alumina block, and ampule are allowed to cool naturally. (The furnace temperature decreases ~350 ^{o}C in 1.5 hours; the temperature profile of the furnace is shown in Figure 5.1.) In the hot loading method, the furnace and the alumina block are preheated to the desired annealing temperature (*i.e.*, 600 or 700 ^{o}C) for at least six hours. After preheating, the furnace door is opened, the ampule is quickly inserted into the alumina block and the furnace door is closed. After 1 hour, the furnace is turned off and the furnace, alumina block, and ampule are allowed to cool naturally. When the ampule is inserted into the alumina lock, ~1 cm of the ampule protrudes from the alumina block. This end cools faster than the rest of the ampule that is in touch with the alumina block. Consequently, selenium condenses on this "cold end" instead of on the sample during the natural cooling stage. The films were characterized using the methods discussed in Chapters 3 and 4.

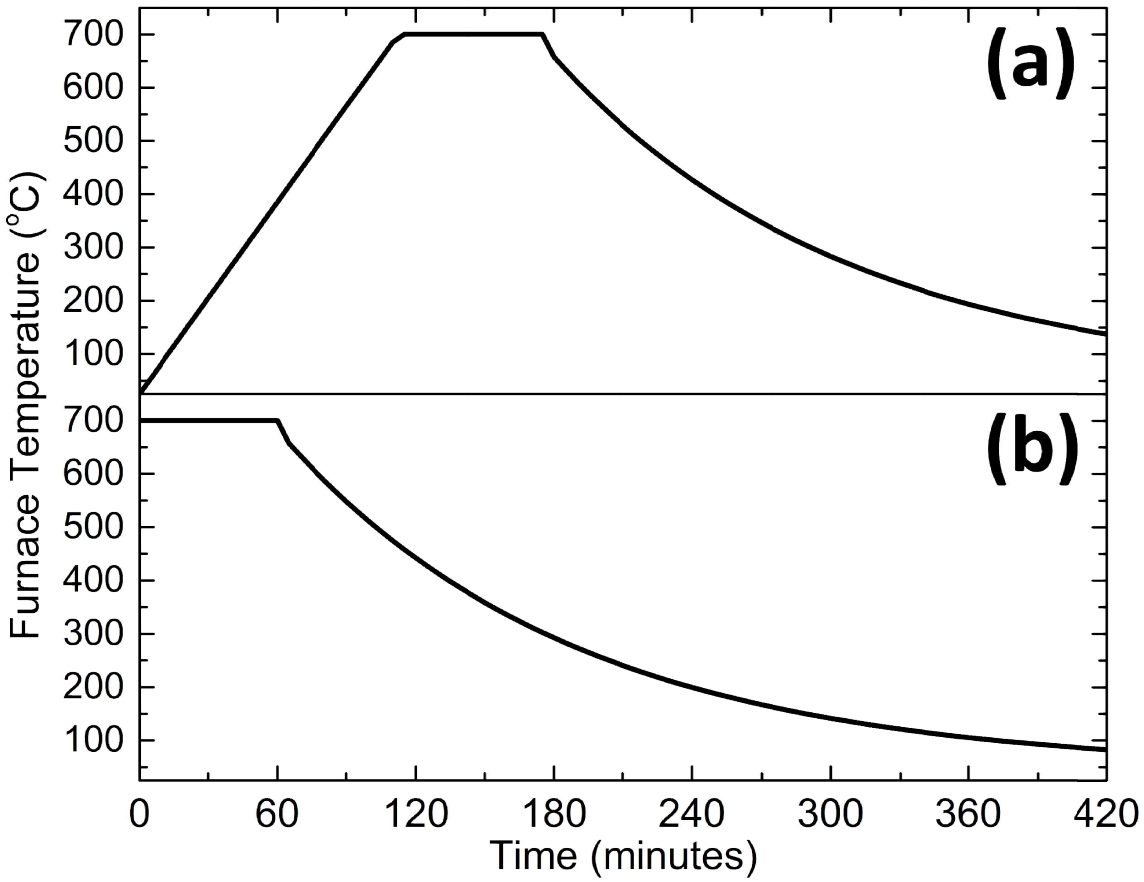

Figure 5.1 Furnace temperature as a function of time for 1 hour annealing at 700 °C using (a) the slow-ramping method and (b) the hot loading method. In the slow-ramping, the furnace is heated at 6 °C/min until the annealing temperature set point is reached (*i.e.*, 700 °C).

5.3 Results

CZTS nanocrystal coatings can be transformed into polycrystalline CZTS films by annealing in sulfur.[12] During this transformation, the nanocrystals grow, sinter and densify to form a polycrystalline CZTS film with grain sizes ranging from several hundreds of nanometers to microns depending on the annealing conditions. When the same CZTS nanocrystal coatings are annealed with selenium vapor, selenium exchanges with the sulfur in the CZTS film during growth and sintering of the crystals. Thus, CZTSSe thin films can be made by annealing CZTS nanocrystals in selenium vapor.[21] There is a significant difference between the sulfur and selenium vapor pressures and their temperature dependence. This difference has important consequences for annealing, particularly in microstructure development. Figures 5.2a and 5.2b show the sulfur and selenium pressures, respectively, in a sealed quartz ampule during annealing as a function

of temperature. Within a closed isothermal system, as the temperature increases, the chalcogen pressure over the annealed film can be determined using the equilibrium vapor pressure curve (the black lines in Figures 5.2a and 5.2b). This continues until the mass of the chalcogen needed to sustain the saturation vapor pressure exceeds the mass charged into the ampule. We denote the temperature at which this condition is reached as T^*. At temperatures lower than T^*, chalcogen liquid and vapor coexist in equilibrium in the ampule. At temperatures greater than T^*, all of the liquid has been converted into vapor and the pressure can be calculated from the ideal gas law. The temperature at which the chalcogen goes from two phases into a single vapor phase increases with increasing chalcogen mass charged into the ampule. The different color curves in Figure 5.2a and 5.2b correspond to the chalcogen pressure in the ampule during annealing at a given temperature. Temperature-dependent speciation, as reported by Rau et al.,[22,23] is taken into account in the calculations (see Appendix B.1 for details of the calculations). Entering the single-phase regime ($T > T^*$) is an advantage of the closed system annealing, because the annealing temperature and chalcogen pressure can be varied independently from each other by changing the amount of chalcogen charged into the ampule. For example, 1 mg of sulfur and 2 mg of selenium produce ~50 Torr of sulfur and selenium, respectively, at 600 °C. The equilibrium vapor pressure of sulfur is greater than that of selenium at any given temperature. In particular, with 1 mg of sulfur, the transition from liquid and vapor coexistence to a single vapor phase (at $T = T_S^*$) occurs at ~260 °C. In contrast, this transition ($T = T_{Se}^*$) is at ~480 °C with 2 mg of selenium. Thus, when sintering and coarsening of the nanocrystals begins at ~350 °C (see Appendix A.1), selenium liquid and vapor coexist in the ampule. The consequence of this will be discussed later in this chapter.

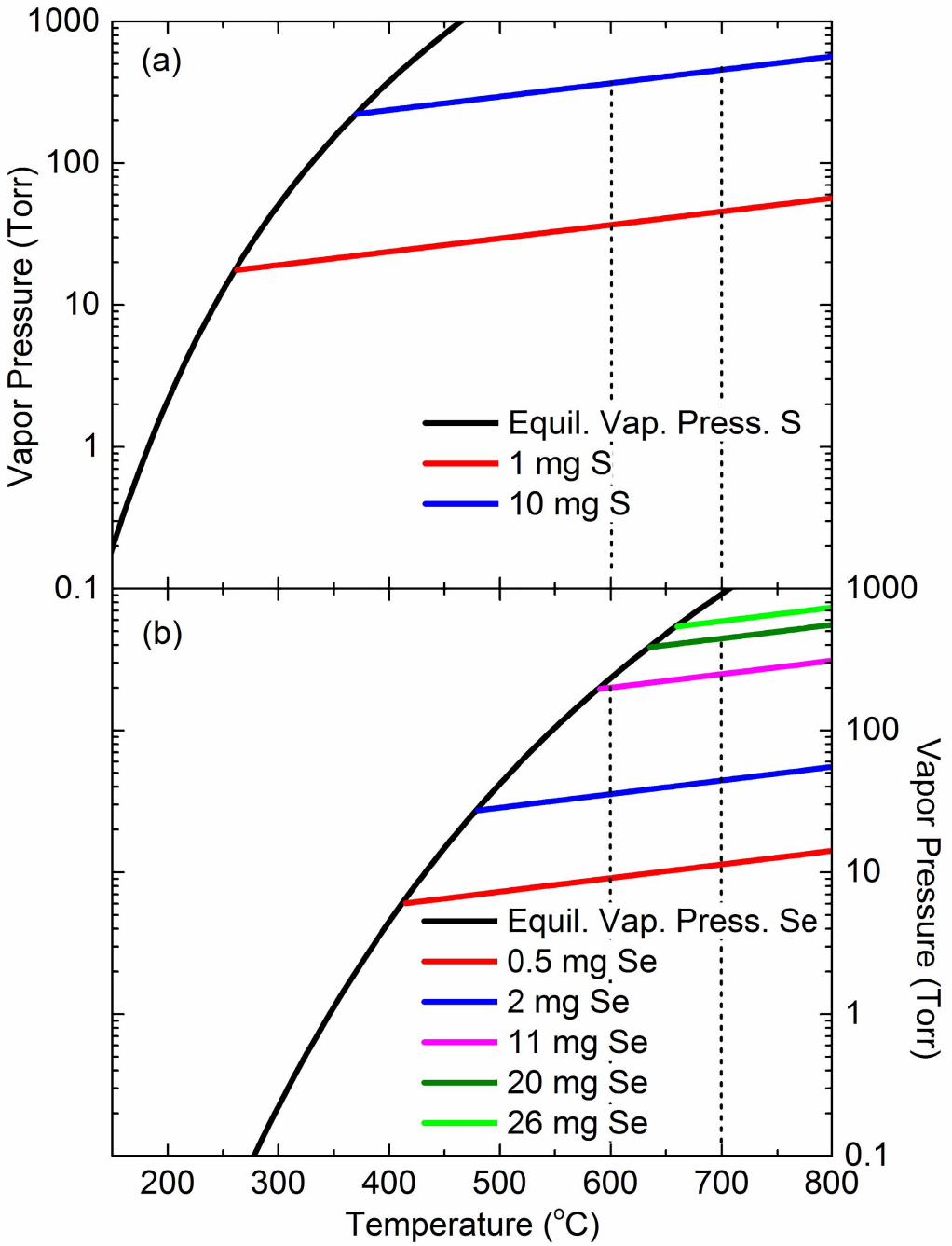

Figure 5.2 Vapor pressures of sulfur (a) and selenium (b) inside of the sealed quartz ampule as a function of temperature for different values of the chalcogen mass charged into the ampule. In both (a) and (b), the black curves are the equilibrium vapor pressure of sulfur or selenium, respectively. The pressure in the ampule follows the different color curves depending on the chalcogen mass charged into the ampule. The temperature dependence of the colored curves is calculated from the known ampule volume and the mass charged into the ampule using the ideal gas law. For a given mass of sulfur or selenium, the pressure in the ampule first follows the equilibrium vapor pressure curve (black) and then continues on the colored curve corresponding to the mass charged into the ampule. Below the temperature where the colored lines intersect the black curve, the chalcogen liquid and vapor coexist. Above that temperature, the chalcogen is all gas.

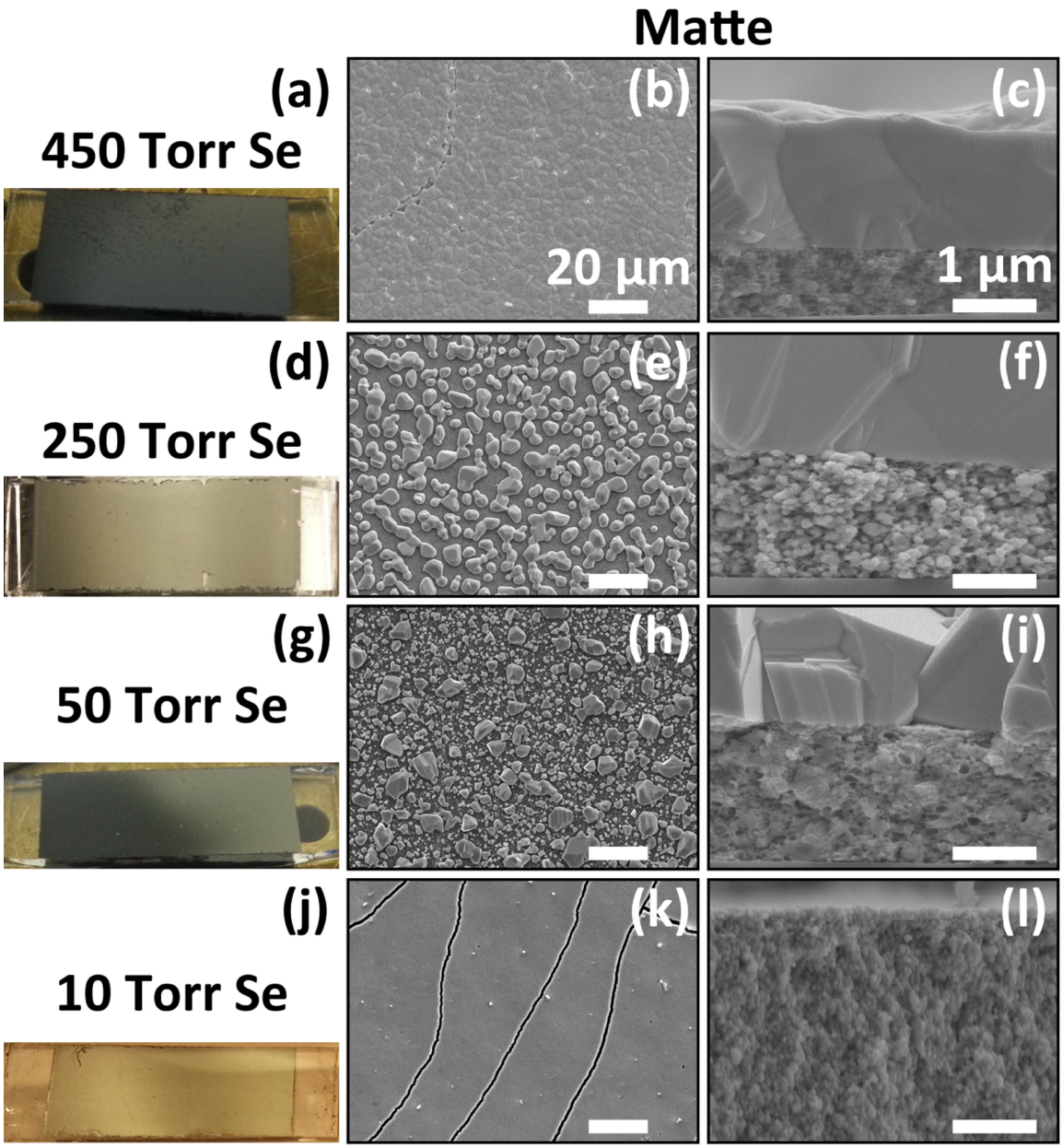

Figure 5.3 Digital photographs, plan view SEM images, and cross-sectional SEM images comparing films annealed at 700 °C with different selenium pressures for 1 hour using the slow ramping method. The selenium pressures in the ampule were (a-c) 450 Torr, (d-f) 250 Torr, (g-i) 50 Torr, and (j-l) 10 Torr. All films were on fused quartz substrates. The scale bars in the plan view images (b, e, h, k) and in the cross-sectional images (c, f, i, l) are 20 µm and 1 µm, respectively.

5.3.1 Annealing via the Slow Ramping Method

Figure 5.3 shows digital photographs and SEM images of nanocrystal coatings after they were annealed for 1 hour at 700 ^{o}C using the slow ramp heating method (see Figure 5.1a for time-temperature profile) with 450 Torr (Figures 5.3a-5.3c), 250 Torr

(Figures 5.3d-5.3f), 50 Torr (Figures 5.3g-5.3i), and 10 Torr (Figures 5.3j-5.3l) of selenium. These films will be referred to as 450s, 250s, 50s, and 10s, where "s" denotes the slow ramp annealing method and the number preceding the "s" is the selenium pressure during annealing. SEM images of the coatings annealed at selenium pressure > 50 Torr show micron-sized CZTSSe crystals (1-8 μm) on top of a layer comprised of much smaller nanocrystals (<100 nm) of CZTSSe. Hereafter, we will refer to this nanocrystalline layer as the floor layer. The crystal size distribution is clearly bimodal. The micron-size grains on the nanocrystalline layer scatter visible light and the films appear matte to the naked-eye. Thus, we will refer to this microstructure as "matte." This is in contrast to the shiny appearance of a smoother microstructure that will be discussed later. A bimodal distribution of grain size in thin films is characteristic of abnormal grain growth, which is driven by the system's tendency to reduce the very large surface area, and the corresponding very large total energy, of the starting colloidal nanocrystal coating. The overall energy of the system is reduced by nucleation and growth of abnormal grains, which consume the smaller normal grains.[24] For a convenient discussion of the features of the microstructure, we adopt the terminology from the grain growth literature and refer to the micron-scale large crystals that are on top of the floor layer as abnormal crystals (or grains) and refer to the nanocrystals in the floor layer as normal crystals (or grains). The photographs, in Figure 5.3, show that the films appear uniform except for the occasional cracking in the pre-annealing nanocrystal coating and occasional dust particles.

Abnormal crystals growth is observed only when the selenium pressure exceeds 10 Torr during annealing. In the 10s film, except for a few crystals <100 nm, we do not observe any abnormal crystals on the floor layer: the light contrast particles visible in Figure 5.3k are silica dust particles, presumed to deposit on the film while breaking the ampule. Furthermore, the normal crystals in the floor layer of the 10s film exhibit very little growth: the width of the (112) XRD peak (Figure 5.4) decreases only slightly and a Scherrer analysis shows that the average grain size increased from ~40 nm to ~55 nm. The abnormal crystals are clearly visible in films 50s and 250s and the average abnormal crystal size increases from ~0.90 μm to ~3.68 μm when the selenium pressure is increased from 50 to 250 Torr. The smaller abnormal grains (~1 μm) observed in 50s

have decreased in areal density when the annealing is conducted in 250 Torr of selenium (*i.e.*, film 250s). With annealing at higher selenium pressures, the normal crystals grow larger: normal crystals are larger in film 250s than in film 50s. The floor layer is thinner in film 250s than in film 50s because material from the floor layer is consumed by the abnormal crystals. As the selenium pressure is increased higher to 450 Torr (film 450s), the nanocrystal coating transforms into a continuous layer of ~1 μm to ~10 μm abnormal CZTSSe crystals (average ~4.00 μm) above the floor layer. This microstructure is similar to that reported in the literature when colloidal CZTS nanocrystals are placed in an unsealed graphite box and annealed in selenium vapor at 550-600 ^{o}C.[25] The grain sizes may be larger here because the annealing is done at 700 ^{o}C. On the other hand, this microstructure is significantly different from that obtained when CZTS nanocrystal coatings are annealed in ~500 Torr of sulfur at 700 ^{o}C: when the CZTS coatings are annealed with sulfur, the normal grains grow much larger (~100-500 nm) which in turn suppresses, but does not completely eliminate, abnormal crystal growth. The resulting microstructure is a floor layer comprised of 100-500 nm normal grains with sparse (~1-2 grains/100 μm^2) ~1-3 μm abnormal grains on top of this floor layer. In contrast, when annealing is done using selenium at nearly the same pressure, the abnormal grain growth dominates and the microstructure is a continuous layer of abnormal grains on top of a much thinner floor with smaller ~120 nm normal grains.

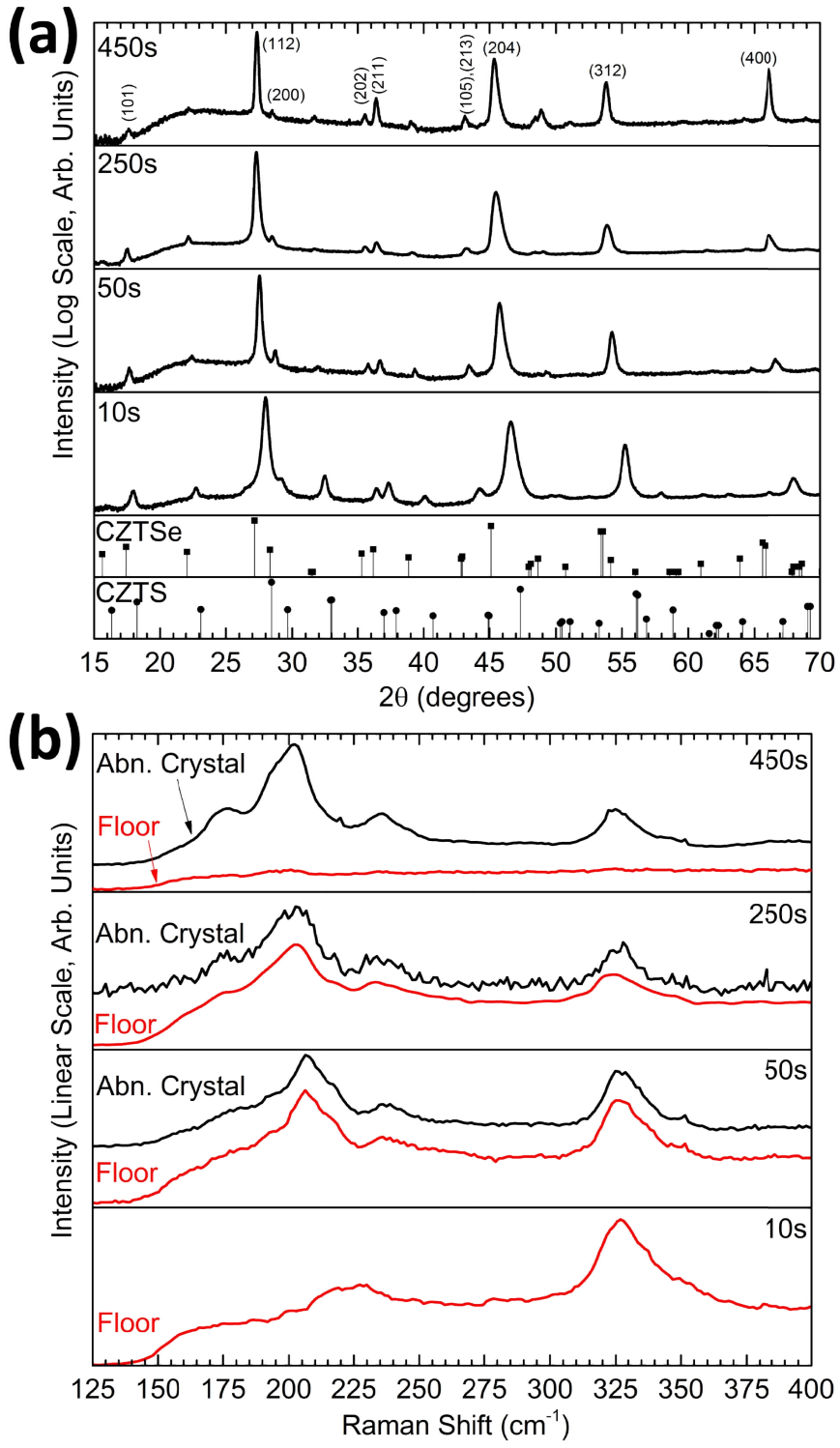

Figure 5.4 (a) XRD patterns and (b) Raman spectra of CZTSSe films annealed at 700 °C for 1 hour in different selenium pressures using the slow ramping method. The selenium pressures were 450 Torr (film "450s"), 250 Torr (film "250s"), 50 Torr (film "50s"), and 10 Torr (film "10s"). The letter "s" in the sample aliases denotes the slow ramp annealing method. The black and red spectra labeled "Abn. Crystal" and "Floor" refer to Raman collected from the abnormal crystals and the floor layers, respectively, in the films annealed at the four different pressures.

Table 5.1 Elemental compositions (%) of the different regions of films annealed at 700 °C for 1 hour using the slow ramp heating method. The values in columns for Cu%, Zn%, Sn%, S%, and Se% sum to 100%. The relative concentration of carbon, shown within the bold column boundaries, was quantified on the basis of all elements present in the coating: $\frac{C\%}{C\%+Cu\%+Zn\%+Sn\%+S\%+Se\%} \cdot 100\%$. The right-most column shows the relative concentration of selenium on the basis of both chalcogens: $\frac{Se\%}{S\%+Se\%} \cdot 100\%$.

Se Pressure (Torr) at 700 °C	Location	Cu %	Zn %	Sn %	S %	Se %	C %	Se/(S+Se) %
450	Matte, Abnormal Crystal	23	11	10	5	51		90
	Matte, Floor	8	3	4	7	78	70	90
250	Matte, Abnormal Crystal	23	12	13	8	44		85
	Matte, Floor	21	12	11	14	42	30	75
50	Matte, Abnormal Crystal	24	12	12	12	40		75
	Matte, Floor	21	11	10	14	44	20	75
10	Matte, Floor	24	11	13	32	20	20	40

Figures 5.4a, 5.4b, and Table 5.1 show the XRD patterns, Raman spectra, and elemental composition, respectively, of the films annealed at 700 °C using the slow ramp heating method. (For comparison with an unannealed CZTS nanocrystal film, please refer to Figure 4.1 in Chapter 4.) In the 10s film, despite very little crystal growth, approximately 38% of the sulfur in the film was replaced by selenium, according to EDS. (The cation composition is approximately stoichiometric within the accuracy of the EDS). Consistent with this observation, the XRD peaks are shifted to smaller 2θ values indicating an expansion of the lattice upon partial selenium substitution. Assuming Vagard's law, the (112) peak shift, from 28.4° to 28.0°, translates to ~33% selenium substitution, which is in reasonable agreement with the composition determined using EDS (38%).

Raman spectra of CZTS exhibit a strong peak at 338 cm^{-1} (A mode) and weaker peaks at 288 cm^{-1} and 348-380 cm^{-1} (shoulder).[12,26–28] In contrast, Raman spectra of CZTSe exhibit a strong peak at 196 cm^{-1} (A mode) with weaker peaks at 174 cm^{-1}, 233 cm^{-1}, and 244 cm^{-1}.[26,29,30] These modes are associated with sulfur (338 cm^{-1}) and selenium (196 cm^{-1}) vibrations. When some of the sulfur is replaced by selenium in CZTS, the Raman spectrum exhibits modes of both CZTS and CZTSSe with two intense peaks, one close to the 338 cm^{-1} mode of CZTS and another close to the 196 cm^{-1} mode of CZTSe. However, the peaks appear shifted depending on the S-to-Se ratio in the films. In

particular, the 338 cm^{-1} mode shifts to lower wavenumbers with increasing selenium substitution, whereas the 196 cm^{-1} mode shifts to higher wavenumbers with increasing sulfur.[29,31,32] Moreover, the peaks broaden which is attributed to anion disorder, *i.e.,* to random distributions of sulfur and selenium in the FCC sublattice.[29,31,32] The Raman spectrum of film 10s (Figure 5.4b) has a strong peak at 328 cm^{-1} and another broad feature that is composed of peaks at 219 cm^{-1} and 227 cm^{-1}. These peak locations are consistent with Raman spectra in the literature where the selenium concentrations are ~30% in the CZTSSe alloys.[29,31,32] When the selenium pressure is increased from 10 Torr to 50 Torr, the selenium substitution during annealing increases sharply from 38% to ~77% (in both the floor and abnormal crystals). Increasing the selenium pressure further to 250 Torr increases the selenium content of the abnormal crystals only marginally to 85%. We detect a small difference in the selenium composition between the abnormal crystals and the floor layer: the selenium substitution for sulfur is 75% in the floor layer. This difference is not surprising because the abnormal grains are growing on the surface where selenium can easily access these crystals while the penetration of selenium into and concurrent removal of sulfur from the floor layer may be slower because of transport limitations into the film. In film 450s, 92% of the sulfur is replaced with selenium in the abnormal crystals and the floor layer The XRD pattern of the 450s sample matches that of CZTSe, except for a small 0.1° shift in the (112) peak, which is at 27.3° instead of 27.2°. Again, this small shift is consistent with Vagard's law and 92% selenium substitution. The Raman spectrum of the abnormal crystal layer in the 450s sample exhibits the A modes of CZTS and CZTSe at approximately 325 cm^{-1} and 202 cm^{-1}, respectively, in agreement with calculations and experimentally measured CZTSSe films with high selenium substitution.[31,32] Raman scattering from the floor layer in sample 450s is weak due to the high concentration of carbon (~68%) in the floor layer.

Each of the four XRD patterns in Figure 5.4a exhibit the characteristic (101), (202), (211), (105), and (213) diffraction peaks of tetragonal CZTSSe, but shifted consistent with Vagard's law and the degree of selenium.[16,33,34] Secondary phases, such as $Cu_{2-x}(S,Se)$ and $Sn(S,Se)_2$, if present in the sampled volumes, were below the XRD detection limit in all films patterns. However, SEM imaging and EDS elemental analysis (Figure 5.5a) of the 450s film occasionally showed hexagonal CuSe platelets, which

protruded out of CZTSSe abnormal crystals. The 250s film (Figure 5.5b) occasionally showed Zn-rich crystals (*e.g.*, %Zn / (%Cu + %Sn) ≈ 3) growing out of the CZTSSe abnormal crystals. No secondary phases were observed in the 50s and 10s films by SEM/EDS. The XRD patterns of cubic ZnS, or ZnSe, and tetragonal Cu_2SnS_3, or Cu_2SnSe_3, are indistinguishable in XRD tetragonal CZTS, or CZTSe. In Raman, no large peaks were detected from these and other secondary phase. As noted earlier, the Raman spectra (Figure 5.4b) exhibit shifting of peak locations, depending on the S-to-Se ratio in the films, as well as peak broadening due to the anion disorder in the lattice. So, scattering from very small amounts of ZnS (350 cm^{-1}),[35] ZnSe (250 cm^{-1}),[30,36] SnS_2 (315 cm^{-1}),[37,38] SnS (192 cm^{-1}),[37,39] $SnSe_2$ (185 cm^{-1}),[40] $Cu_{2-x}Se$ (260 cm^{-1}),[41,42] Cu_3SnS_4 (318 cm^{-1}),[43] tetragonal Cu_2SnS_3 (336 cm^{-1}), cubic Cu_2SnS_3 (303 & 355 cm^{-1}),[43] and cubic Cu_2SnSe_3 (180 cm^{-1})[43] cannot be ruled out. The peaks for $Cu_{2-x}S$ (475 cm^{1})[44,45] and SnSe (130 & 150 cm^{-1})[39,46] are absent in all spectra.

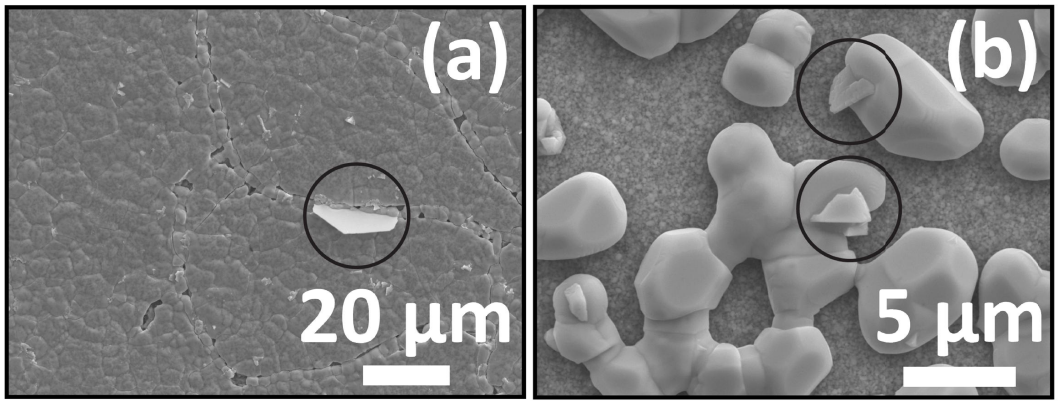

Figure 5.5 SEM images of binary phases (circled) of (a) Cu(S,Se) and (b) Zn(S,Se) protruding out of the large abnormal CZTSSe grains in the 450s and 250s films, respectively.

5.3.2 Annealing via the Hot Loading Method

Figure 5.6 shows digital camera photographs and SEM images of films annealed at 700 ^{o}C for 1 hour using the hot loading method (refer to Figure 5.1b for furnace temperature as a function of time). Each row in Figure 5.6 shows images for a different selenium pressure at 700 ^{o}C: 450 Torr (a-e), 250 Torr (f-j), 50 Torr (k-o), and 10 Torr (p-r). These films will be called 450h, 250h, 50h, and 10h, where "h" refers to the hot load annealing method. Unlike the uniform appearance of films obtained with slow ramp annealing, visual inspection of the films annealed using hot loading method shows two

distinct regions: a region with a matte/rough appearance and a region with a shiny/smooth appearance. These regions are identified with “m” and “s” in the digital photographs. The matte region microstructure in each of the hot loaded films is similar to the microstructure of the films obtained when the coatings are annealed using the slow ramp annealing method (Figure 5.3).

The matte regions have a bimodal distribution of crystal sizes while the smooth have a single crystal size distribution. The matte microstructure is composed of micron-scale abnormal CZTSSe crystals on top of a CZTSSe floor layer containing nanocrystalline normal grains. In the matte region, the average size of the abnormal crystals increases with increasing selenium pressure, up to as large as ~ 10um at 450 Torr of selenium, while the normal grain sizes increase in size slower, up to only ~120 nm at 450 Torr of selenium. In the smooth regions, this behavior is reversed: there is no abnormal crystal growth but the normal grains grow larger with increasing selenium pressure, eventually becoming as large as 1 μm at 450 Torr. With both annealing strategies (hot loading and slow ramping), the films annealed in 10 Torr of selenium (films 10s and 10h) exhibit only <100 nm abnormal crystals and very little normal grain growth (increasing to ~55 nm from ~40 nm).

Table 2 shows the elemental compositions, measured by EDS, of the coatings that were annealed using the hot loading method. Like in the coatings annealed using the slow ramping method, the carbon concentration in the floor layer of the matte region rises sharply, from ~24% to ~51%, when the selenium pressure is increased from 250 Torr to 450 Torr. In contrast, the relative carbon concentrations in the smooth regions of all the films were ~20% or less. In smooth regions, there is no segregation and accumulation of carbon near the substrate-film interface. The smooth region is comprised of a dense layer of CZTSSe crystals and carbon appears to be uniformly dispersed throughout this layer. We observe fibrous structures that appear to surround some of the grains.

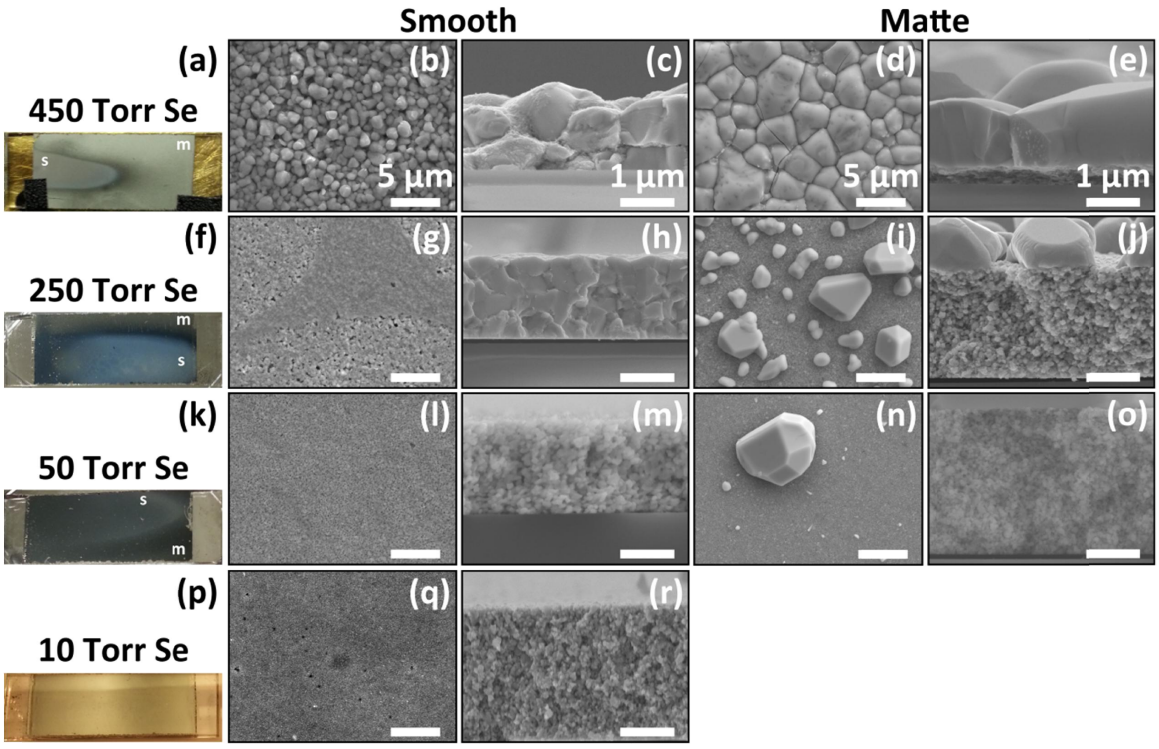

Figure 5.6 Digital photographs, plan view SEM images, and cross-sectional SEM images comparing CZTS nanocrystal coatings cast on fused quartz and then annealed at 700 °C for 1 hour using the hot loading method in different selenium pressures. Selenium pressures in the annealing ampule were (a-e) 450 Torr, (f-j) 250 Torr, (k-o) 50 Torr, and (p-r) 10 Torr. All scale bars in the plan view images (b, d, g, i, l, n, q) and in the cross-sectional images (c, e, h, j, m, o, r) are 5 µm and 1 µm, respectively. The matte and smooth regions are labeled in the digital photographs as "m" and "s," respectively.

Figures 5.7a and 5.7b show XRD patterns and Raman spectra, respectively, for the films annealed using the hot loading method. The extent of selenium substitution for sulfur increases with increasing pressure is similar to the films annealed using the slow ramping method. The selenium concentration calculated from the location of the (112) XRD peak location using Vagard's law is in good agreement with the selenium concentration measured by EDS. (In particular, the selenium content calculated from the XRD peak locations in the regions with the matte appearance in the 450h, 250h, 50h, and 10h films is 86%; 78%; 60%; and 49%, respectively. The regions with the smooth appearance in the 450h, 250h, and 50h films have a relative selenium concentration of 81%; 80%; and 62%, respectively.) Similarly to the films annealed by the slow ramping method, in the films annealed by the hot loading method we detect a small difference in the selenium composition measured by EDS between the abnormal crystals and the floor layer in the regions with the matte appearance, where the abnormal have more selenium.

XRD peaks expected from tetragonal CZTSSe [*i.e.*, (101), (202), (211), (105), and (213)] were all present in the XRD patterns of each of the four films that were annealed by the hot loading method. XRD peaks for secondary phases were either not present in the sampled volume or were below the detection limit. However, infrequently we observed Cu(S,Se) platelets and Zn(S,Se) crystals protruding from large abnormal CZTSSe crystals in the 450h film via SEM and EDS (similar to those shown in Figure 5.5). Raman spectra of the films annealed using the hot loading method are similar to those films that were annealed using the slow ramping method. The Raman spectrum of the floor in the matte region of the 450h film has a broad peak centered at 257 cm^{-1}, which may arise from ZnSe (~250 cm^{-1}) and/or $Cu_{2-x}Se$ (260-270 cm^{-1}).

Table 5.2 Elemental compositions (%) of the different regions of films annealed at 700 °C for 1 hour using the hot loading method. The values in columns for Cu%, Zn%, Sn%, S%, and Se% sum to 100%. The relative concentration of carbon, shown within the bold column boundaries, was quantified on the basis of all elements present in the coating: $\frac{C\%}{C\%+Cu\%+Zn\%+Sn\%+S\%+Se\%} \cdot 100\%$. The right-most column shows the relative concentration of selenium on the basis of both chalcogens: $\frac{Se\%}{S\%+Se\%} \cdot 100\%$.

Se Pressure (Torr) at 700 °C	Location	Cu %	Zn %	Sn %	S %	Se %	C %	Se/(S+Se) %
450	Matte, Abnormal Crystal	23	11	12	7	47		90
	Matte, Floor	21	10	9	8	52	50	90
	Smooth	23	12	12	8	45	20	85
250	Matte, Abnormal Crystal	24	12	11	7	46		85
	Matte, Floor	24	12	12	14	38	20	75
	Smooth	23	12	12	13	40	10	75
50	Matte, Abnormal Crystal	26	13	11	15	35		70
	Matte, Floor	23	11	12	23	31	20	55
	Smooth	23	12	12	21	32	20	60
10	Matte, Floor	25	12	13	27	23	20	45

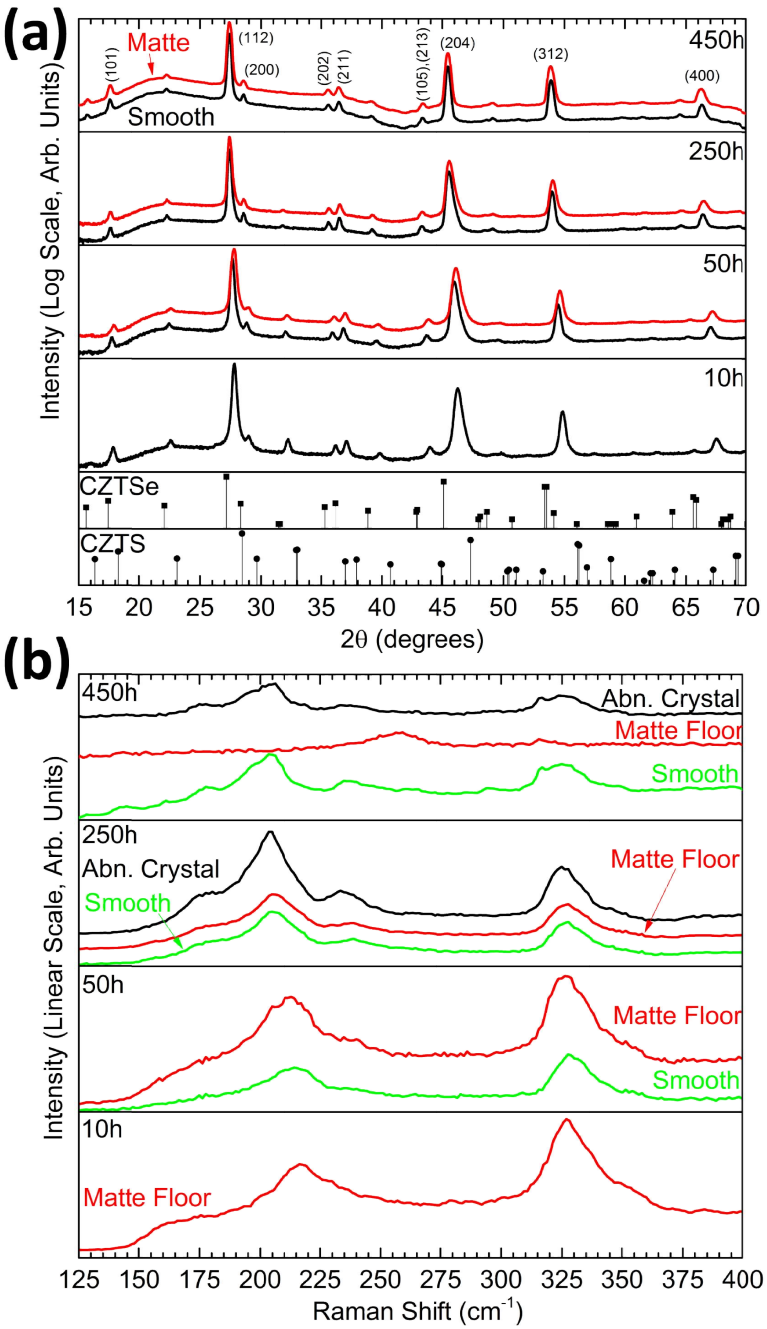

Figure 5.7 (a) XRD patterns and (b) Raman spectra of CZTSSe films annealed using the hot loading method. The films were annealed at 700 °C for 1 hour in 450 Torr ("450h"), 250 Torr ("250h"), 50 Torr ("50h"), and 10 Torr ("10h") of selenium. The letter "h" in the sample aliases stands for annealing using the hot loading method. The labels "Matte" and "Smooth" refer to the film regions with the matte and smooth appearances, respectively. In (b), the black and red Raman spectra labeled "Abn. Crystal" and "Matte Floor" refer to Raman collected from the abnormal crystals and the floor layers, respectively, in the regions with the matte appearance at the four different pressures. The green spectra labeled "Smooth" refers to Raman collected in the regions with the smooth appearance. Raman spectra from the 450h film have several peaks that were due to artifacts of the filter used at the time: 295 cm^{-1}, 315 cm^{-1}, and 335 cm^{-1}.

The hot loading annealing method leads to the development of regions with matte and smooth appearances at other annealing temperatures, such as 600 ^{o}C. Figure 8 shows two films annealed at 600 ^{o}C using the hot loading method. One of the films was annealed in ~240 Torr selenium (8a-8e) while the other was annealed in ~40 Torr selenium (8f-8j). At 600 ^{o}C, the highest achievable pressure is ≈240 Torr. The abnormal crystals in the regions with the matte appearance in the films annealed at 600 ^{o}C are smaller than the abnormal crystals in the matte regions of the films annealed at 700 ^{o}C at both selenium pressures. Similarly, the nanocrystals in the floor of the regions with the smooth appearance are smaller in the films annealed at 600 ^{o}C than in the films annealed at 700 ^{o}C, which is determined from the difference in the XRD peak broadening. The smooth region of the film annealed in 240 Torr of selenium (8b & 8c) contains some abnormal grains but at a much lower density (*i.e.*, #/area) than the density of the abnormal grains in the matte region. The relative selenium concentrations in the different regions of the films annealed at 600 ^{o}C in 240 and 40 Torr, summarized in Table 3, are nearly identical to the selenium concentrations in the different regions of the films annealed at 700 ^{o}C at 250 and 50 Torr, respectively. Figures 9a and 9b show the XRD patterns and the Raman spectra, respectively, for the films annealed at 600 ^{o}C in 240 and 40 Torr of selenium.

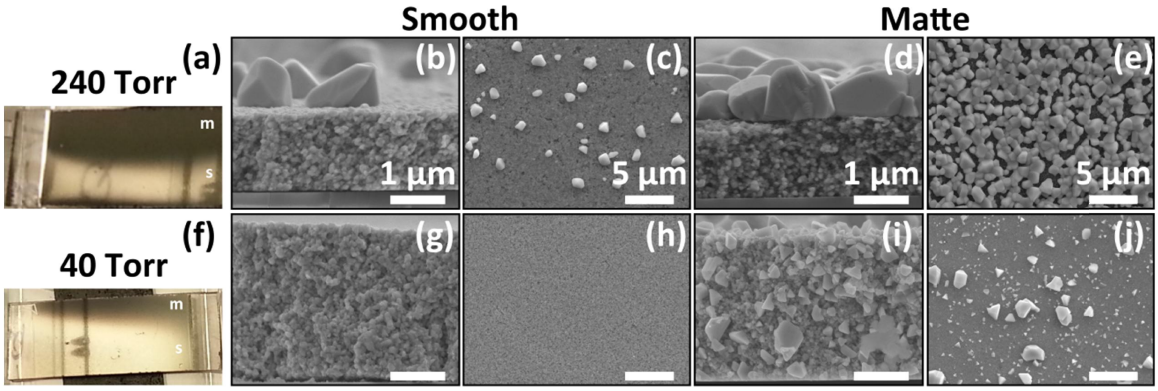

Figure 5.8 Digital photographs, plan view SEM images, and cross-sectional SEM images comparing films annealed at 600 °C for 1 hour in (a-e) 240 Torr and in (f-j) 40 Torr selenium using the hot loading method. All films were on fused quartz substrates. All scale bars in the plan view images (b, d, g, i) and in the cross-sectional images (c, e, h, j) are 5 µm and 1 µm, respectively. The matte and smooth regions are labeled in the digital photographs as "m" and "s," respectively.

Table 5.3 Elemental compositions (%) of the different regions of films annealed at 600 °C for 1 hour using the hot loading method. The values in columns for Cu%, Zn%, Sn%, S%, and Se% sum to 100%. The relative concentration of carbon, shown within the bold column boundaries, was quantified on the basis of all elements present in the coating: $\frac{C\%}{C\%+Cu\%+Zn\%+Sn\%+S\%+Se\%} \cdot 100\%$. The right-most column shows the relative concentration of selenium on the basis of both chalcogens: $\frac{Se\%}{S\%+Se\%} \cdot 100\%$.

Se Pressure (Torr) at 600 °C	Location	Cu %	Zn %	Sn %	S %	Se %	C %	Se/(S+Se) %
240	Matte, Abnormal Crystal	23	11	12	8	46		85
	Matte, Floor	21	10	9	9	51	52	85
	Smooth	24	12	12	8	44	27	85
40	Matte, Abnormal Crystal	24	11	12	19	34		65
	Matte, Floor	23	11	12	21	33	26	60
	Smooth	22	11	12	18	37	22	65

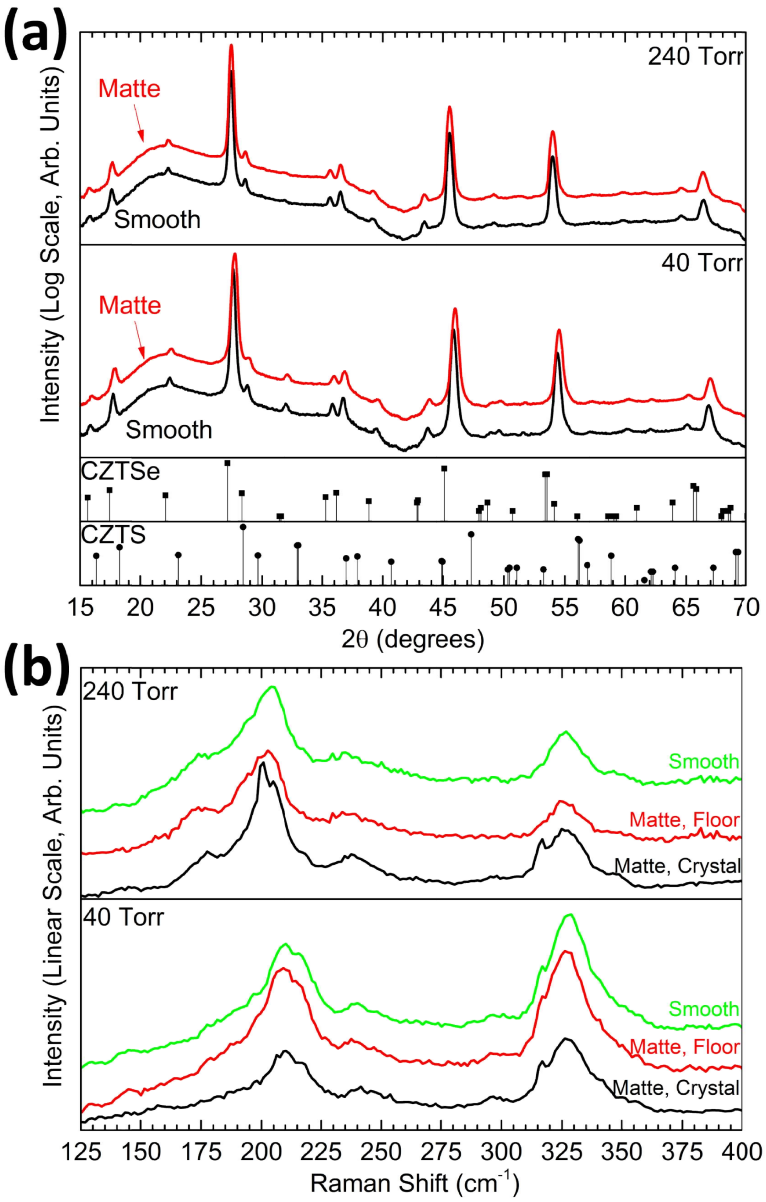

Figure 5.9 (a) XRD patterns and (b) Raman spectra of CZTSSe films annealed at 600 °C for 1 hour in 240 Torr and 40 Torr selenium using the hot loading method. The labels "Matte" and "Smooth" refer to the film regions with the matte and smooth appearances, respectively. In (b), the black and red Raman spectra labeled "Matte, Crystal" and "Matte, Floor" refer to Raman collected from the abnormal crystals and the floor layers, respectively, in the regions with the matte appearance at the four different pressures. The green spectra labeled "Smooth" refers to Raman collected in the regions with the smooth appearance. Note that the Raman spectrum of the abnormal crystal from the 240 Torr film and all spectra from the 40 Torr films several peaks that were due to artifacts of the filter used at the time: 295 cm^{-1}, 315 cm^{-1}, and 335 cm^{-1}.

The appearance of two regions with different microstructures, matte and smooth, when annealing using the hot loading method is not unique to quartz substrates but occurs on soda lime glass (SLG), as well. For example, Figures 5.10a, 5.10b, and 5.10c show a

digital photograph and plan view SEM images of a film on SLG that was annealed at 600 ^{o}C for 1 hour in 240 Torr of selenium. Indeed, there is a smooth region and a matte region.

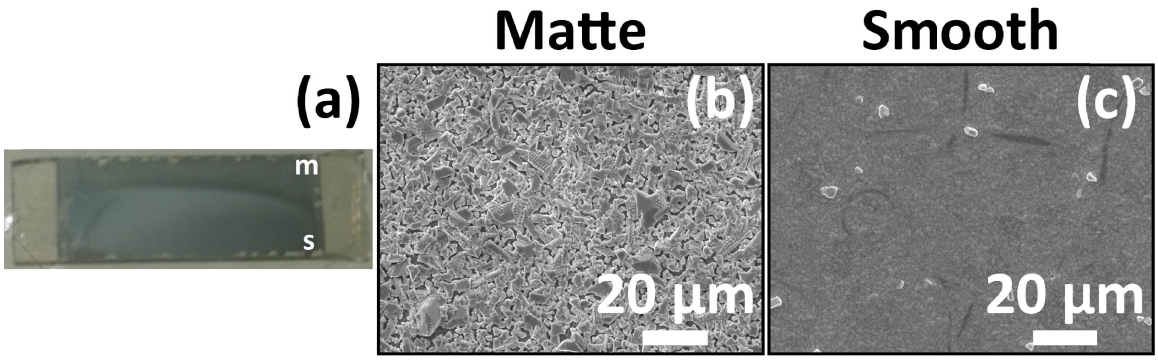

Figure 5.10 (a) Digital photograph of a CZTS nanocrystal coating cast onto an SLG substrate and subsequently annealed at 600 ^{o}C for 1 hour in 240 Torr selenium using the hot loading method. Plan view SEM images of the (b) matte and (c) smooth regions of the film. The matte and smooth regions are labeled in the digital photographs as "m" and "s," respectively.

5.4 Discussion

5.4.1 The Role of Carbon and Selenium In the Formation of a Carbon-Rich Floor Layer

While one would expect the reaction chemistry between carbon and selenium to be similar to that between carbon and sulfur, there are significant differences. These differences offer insight into the reasons for carbon segregation to the interface between the CZTSSe film and the substrate during selenization but not during sulfidation.[12,16,25,47] For example, the CZTS nanocrystal coating annealed at 700 ^{o}C for 1 hour in selenium shows a carbon rich layer between the CZTSSe film and the substrate. In contrast, during sulfidation under identical conditions, carbon is almost entirely removed from the film and there is no sign of carbon rich film at the film-substrate interface. This carbon segregation during selenization is not unique to CZTS nanocrystals and has been observed during selenization of other nanocrystal coatings including $Cu(In,Ga)(S,Se)_2$[48] and $CuInSe_2$.[49] The segregation is also independent of the substrate and the carbon layer forms during selenization when the nanocrystals are on SLG, quartz or Mo.

It has been suggested that the top layer of abnormal crystals develops quickly during selenization and forms a "capping" layer, which traps and segregates the carbon in the bottom floor layer.[16,19,20] However, this hypothesis is not supported by our observations. In our films, the abnormal CZTSSe crystal layer in the regions with the matte appearance is not always continuous: sometimes the abnormal crystals do not form a continuous layer or there are significant voids in the abnormal crystal layer. Where the floor layer is exposed, in the regions with the matte appearance, we observe high concentrations of carbon.

The experimental observations suggest that sulfur is more effective in removing carbon from the nanocrystal coatings then selenium. This is surprising because CSe_2, CS_2, OCS and OCSe, the expected products of the reactions of between the ligands (oleic acid and oleylamine) and the chalcogen vapor, are all very volatile. Both sulfur and selenium vapor penetrate well into the nanocrystal coating. This is evidenced by the efficient exchange of sulfur atoms in CZTS with selenium to form CZTSSe as well as by the formation of $MoSe_2$ and MoS_2 at similar rates, during selenization and sulfidation, respectively, when the substrate is molybdenum-coated glass. One significant difference between CSe_2 and CS_2, however, is that CSe_2 readily polymerizes.[50] Thus, the CSe_2 molecules that form via the reactions between the selenium vapor and the ligands (or their thermal decomposition products) can polymerize to form a $(CSe_{2-x})_n$ matrix trapping carbon and selenium in the film. Figure 5.11 shows a Raman spectrum of the floor layer in the 250s film, as an example. The spectrum exhibits two large peaks at ~1350 cm^{-1} and ~1580 cm^{-1} which are characteristic of graphite with nanocrystalline domains.[51,52] While direct measurement of pure polymerized CSe2 has been reported via Raman spectroscopy, with a peak at ~1475 cm^{-1} (using 647.1 nm excitation),[53] the peak is weak. The intense and broad nature of these peaks masks scattering from CSe_2.

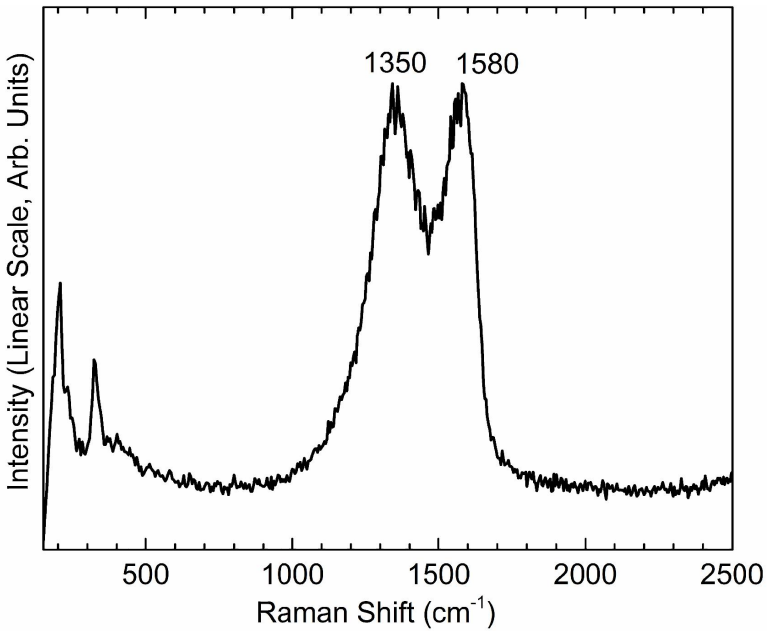

Figure 5.11 Raman spectrum from the floor layer in a film that was annealed at 700 ^{o}C for 1 hour in 250 Torr of selenium.

5.4.2 The Smooth Region Forms During Annealing by the Hot Loading Method, But Not During Annealing By the Slow Ramping Method, Due To Selenium Condensation

Although films annealed by the hot loading method and those annealed by the slow-ramping method spend different amounts of time at elevated temperatures (*i.e.* >350 ^{o}C), this difference does not account for the observation of the smooth region in films annealed by hot loading. The temperatures of the ampule and its contents rise more rapidly to the set point (700 ^{o}C) during annealing by the hot loading method than during annealing by the slow-ramping method. Thus, the film spends less time at elevated temperatures when annealed by hot loading. To explore whether this time difference is related to the formation of the smooth regions, we conducted an experiment where the film is annealed using the hot loading method but the time the film spends at elevated temperatures is longer and similar to that in experiments where the films are annealed using the slow ramping method. Figures 5.12a, 5.12b, 5.12c show a digital photograph and plan view SEM images of a CZTS film annealed at 700 ^{o}C for 3 hours at 250 Torr of selenium using the hot loading method. These conditions are the same as those used to anneal film 250h but the annealing duration was longer and approximately the same as

those used in 250s. Upon removal from the ampule, this film exhibited both a smooth and a matte region, thus ruling out difference in annealing time as the reason for the existence of the smooth microstructure in hot loaded films. The XRD patterns and Raman spectra (not shown) are similar to those for the 250h film (Figure 5.7), but with higher degree of selenium substitution into the floor layer than that measured in the 250h film. In fact, both the matte and smooth regions had ~80-89% selenium substitution as determined by EDS (Table 4) and the locations of the (112) XRD peaks. This higher degree of selenium substitution is expected because the films were at elevated temperatures for a longer period for Se-S exchange to take place.

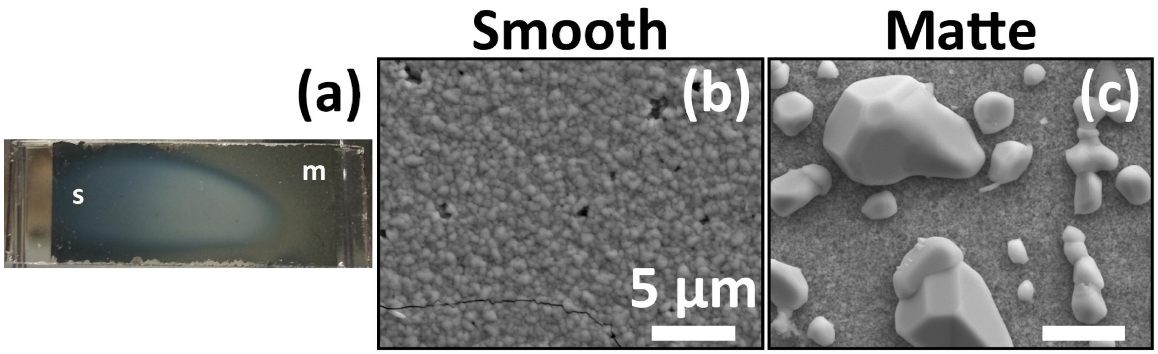

Figure 5.12 (a) Digital photograph of a CZTS nanocrystal coating, cast on fused quartz, and annealed at 700 °C for 3 hours at 250 Torr selenium using the hot loading method.. Plan view SEM images of the (b) smooth and (c) matte regions of the film.

Table 5.4 Elemental compositions (%) of the different regions of the film annealed at 700 °C for 3 hours using the hot loading method. The values in columns for Cu%, Zn%, Sn%, S%, and Se% sum to 100%. The relative concentration of carbon, shown within the bold column boundaries, was quantified on the basis of all elements present in the coating: $\frac{C\%}{C\%+Cu\%+Zn\%+Sn\%+S\%+Se\%} \cdot 100\%$. The right-most column shows the relative concentration of selenium on the basis of both chalcogens: $\frac{Se\%}{S\%+Se\%} \cdot 100\%$.

Se Pressure (Torr) at 700 °C	Location	Cu %	Zn %	Sn %	S %	Se %	C %	Se/(S+Se) %
250	Matte, Abnormal Crystal	22	12	11	6	49		90
	Matte, Floor	22	11	11	11	45	35	80
	Smooth	22	14	12	7	46	25	85

To test whether the development of the smooth microstructure is unique to annealing of CZTS nanocrystal coatings, we annealed a 430 nm thick Cu-Zn-Sn alloy film that was deposited on quartz substrates using cosputtering.[54] This film was annealed at 700 °C in 450 Torr selenium using the hot loading method. The resulting film morphology was uniform and exhibited micron size grains similar to the matte regions of

the nanocrystal coatings annealed under the same conditions. Figures 5.13a and 5.13b, show digital photographs before and after annealing, while Figures 5.13c, 5.13d and 5.13e show a plan view SEM image, XRD pattern, and Raman spectrum from this film. The film's XRD and Raman spectra are similar to those from films obtained by annealing nanocrystal coatings under the same conditions. However, the film synthesized by annealing the metal alloy is uniform and exhibits only one type of morphology. Thus, the microstructure observed in the smooth regions (*e.g.*, Figure 5.3) appears to be unique to the CZTS nanocrystal coatings. The unique attribute that gives rise to the two types of morphologies, and in particular to the smooth appearance microstructure may be the presence of the CZTS nanocrystals, carbon (*i.e,* the ligands), or the combination of both. We test these possibilities in the following experiments.

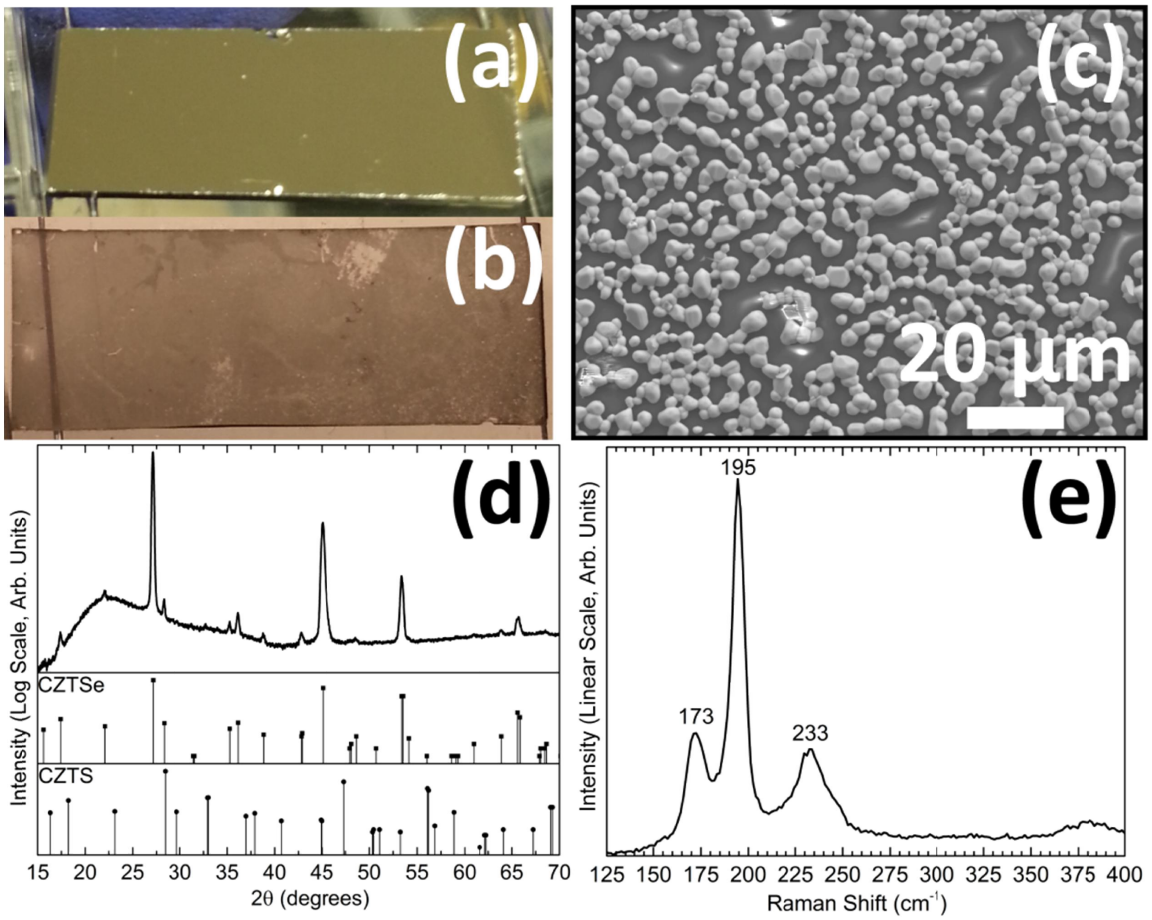

Figure 5.13 Digital photographs of a Cu-Zn-Sn metal alloy film deposited by co-sputtering (a) before and (b) after annealing. The film was annealed at 700 ^{o}C in 450 Torr of selenium for 1 hour using the hot loading method. (c) A representative plan view SEM image of the annealed film. (d) XRD pattern and (e) Raman spectrum from the annealed CZTSe film.

The selenium vapor can condense in the pores of the nanocrystal film due to the pressure difference across the high curvature liquid-vapor interfaces that may form within the interparticle voids.[55,56] Although capillary condensation would occur everywhere on the film and is not entirely consistent with the observation of two regions with different morphologies, nevertheless, this hypothesis may be tested with experiments. To test whether capillary condensation may be responsible for the smooth region, we annealed a film using the slow ramping method such that the selenium vapor pressure was saturated and on the liquid-vapor equilibrium line (black curve in Figure 5.2b) during the entire heating and cooling cycle. Slow heating eliminates the possibility that the selenium is condensing due to temperature gradients. Selenium may still condense in the capillaries because the entire system is kept in the two-phase region of the phase diagram. If selenium is condensing in the nanopores of the film we should again see the non-uniform morphology. Figure 5.14 shows a film annealed using the slow ramping method at 600 ^{o}C with 240 Torr of selenium (or 26 mg, which is in excess of the 11 mg necessary to establish 240 Torr) such that selenium vapor and liquid coexist in the ampule during annealing. The resulting film is entirely uniform and has the microstructure corresponding to matte appearance, suggesting that capillary condensation is not the cause for the formation of the morphology with smooth appearance.

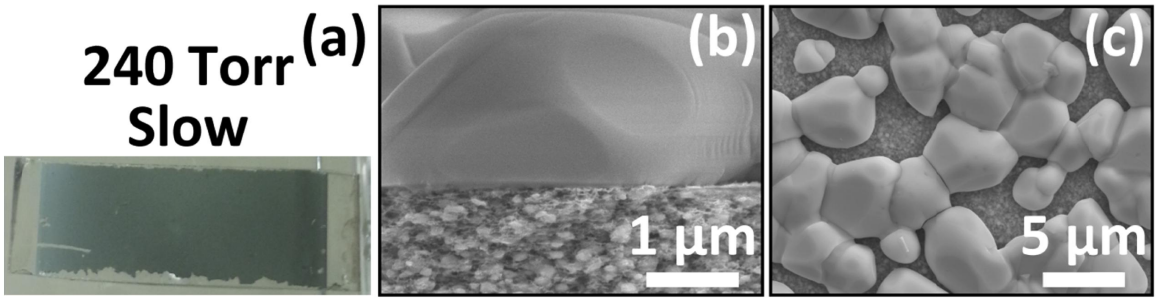

Figure 5.14 (a) Digital photograph of a CZTS nanocrystal coating cast onto fused quartz and then annealed at 700 ^{o}C for 1 hour in 240 Torr of selenium using the slow-ramping method. (b) Cross sectional and (c) plan view SEM images of this film which uniformly had the microstructure with the matte appearance.

One possibility is that a smooth region may form due to an interaction between condensed liquid selenium and the carbon species present in the nanocrystal coating during annealing. To test this, a 25 nm thick amorphous carbon film was deposited on the quartz substrate using thermal evaporation. Amorphous carbon was taken as a proxy for

the CZTS nanocrystal ligands. (While an oleic acid film would have been a better proxy, unfortunately, a uniformly dried oleic acid film could not be deposited.) The thickness of the amorphous carbon film was chosen such that the total number of moles of carbon in the amorphous film was approximately equal to that in a CZTS nanocrystal coating (see Appendix B.4 for details).[57] After annealing, the film became darker but the microstructure under SEM observation (not shown) remained uniform. Figures 5.15a and 5.15b show digital photographs and Raman spectra of an amorphous carbon film before and after it was annealed at 700 ^{o}C in 450 Torr selenium for 1 hour using the hot loading method. The XRD (not shown) shows an amorphous coating before and after annealing and elemental analysis by EDS (also not shown) showed no significant change in the film composition after annealing and no significant selenium incorporation. The Raman spectrum before annealing is consistent with amorphous carbon and the spectrum after annealing is consistent with annealed graphite with nanocrystalline domains.[52,58] Assuming that amorphous carbon is a good proxy for CZTS nanocrystal ligands, this experiment shows that chemistry of carbon with selenium (vapor or condensed) is not a significant factor in the development of non-uniform microstructure in the nanocrystal coatings. It appears that CZTS nanocrystals and selenium condensation on part of the substrate are the key ingredients for observing different microstructures in the annealed films.

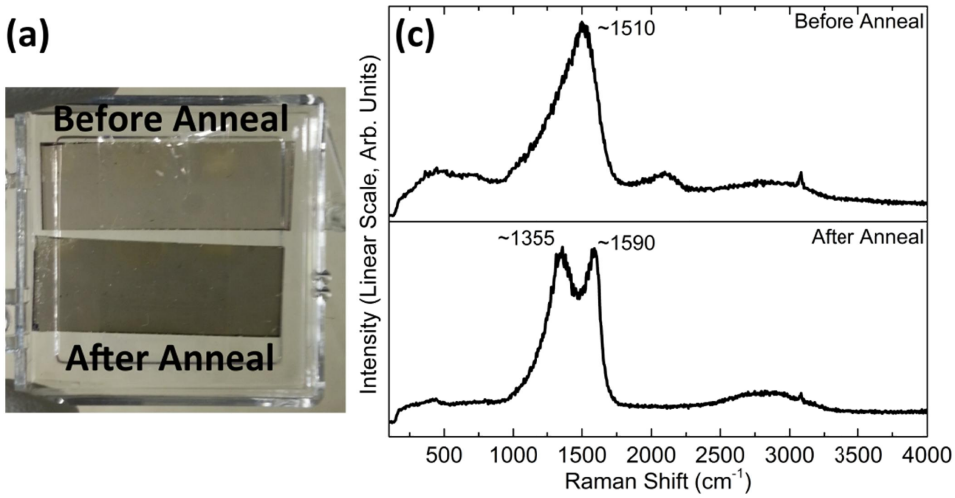

Figure 5.15 (a) Digital photograph an amorphous carbon film evaporated onto fused quartz before and after annealing. The film was annealed at 700 ^{o}C in 450 Torr selenium for 1 hour using the hot loading method. (b) Raman spectra of the amorphous carbon film before and after annealing, showing the change from amorphous carbon to graphite with nanocrystalline domains.[52,58]

Another possibility for the formation of a smooth and a matte region during annealing using the hot loading method is the existence of spatial temperature gradients both within the different regions of the ampule and the substrate during the rapid temperature rise. We hypothesized that such gradients can lead to evaporation from the hotter regions of the ampule and condensation on the colder regions including the substrate. During rapid heating, the temperature of the substrate lags behind that of the region where the selenium is placed. Such a lag is plausible because the temperature of the thin-wall quartz ampule, which is in contact with the hot alumina block, increases faster than that of the thicker quartz substrate, which is inside of the ampule. As the temperature of the ampule increases, the selenium evaporates and then the selenium vapor can condense when it encounters the colder quartz substrate. The visual clue implicating spatial gradients is the parabolic shape of the boundary between the smooth and matte regions: see for example, the digital photograph of the film 450h in Figure 5.6a. Moreover, we found that the direction that the vertex of this parabolic boundary points is determined by the position of the solid selenium charge relative to the substrate: the vertex is always positioned on the side away from the solid selenium charge, e.g., the smooth region always appears closer to the solid selenium charge while the matte region is always on the farthest side. Figure 5.16 illustrates this observation regarding the shape of the smooth region and its relation to the position of the selenium charge with respect to

the substrate. These observations suggest that selenium may be condensing on the film during the temperature transient because the substrate temperature lags behind that of the region with the selenium charge.

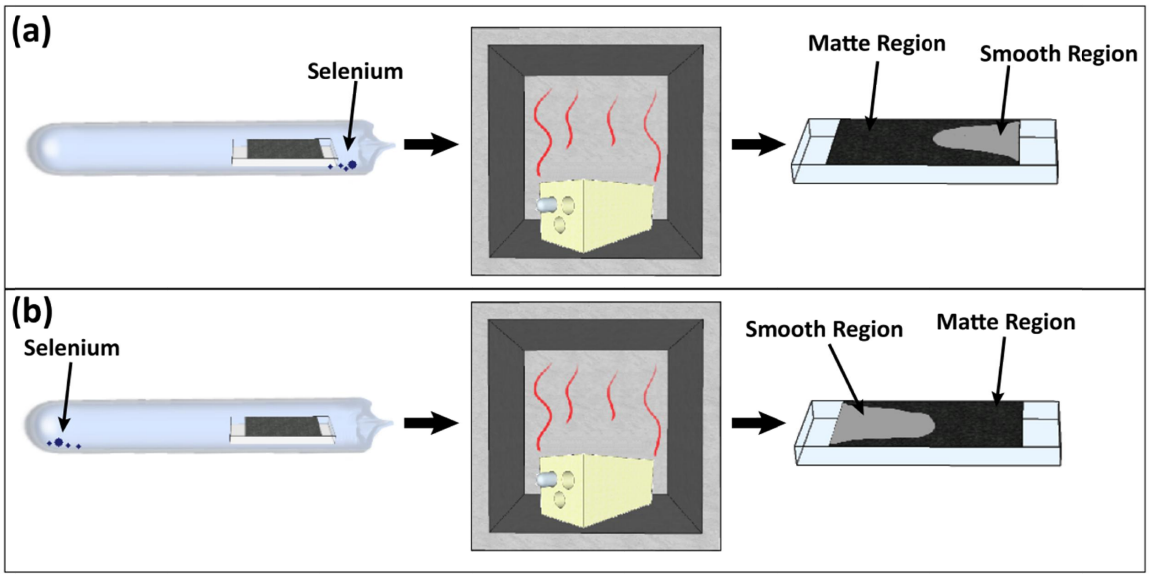

Figure 5.16 An illustration depicting the shape of the region that has the microstructure with smooth appearance as a function of the location of the selenium shot with respect to the substrate. The vertex of the parabola shaped boundary between the smooth and matte regions is always away from the solid selenium as shown in (a) and in (b).

5.4.3 A Mechanism for the Formation of the Smooth Region Microstructure: Liquid Phase Sintering

We propose that the two regions with different microstructure develop through two different mechanisms: the morphology with the smooth appearance develops through liquid-phase (selenium) sintering, while the matte morphology develops through solid state sintering while interacting with selenium vapor. These two fundamentally different mechanisms are revealed, serendipitously, in annealing experiments where the ampules are heated rapidly. Transient temperature gradients, caused by the rapid heating, condense selenium on the side of the substrate closest to the selenium source while condensation does not take place on the farther side. Liquid phase sintering is a mechanism wherein both grain size coarsening and film densification is mediated by the presence of a liquid phase.[59] Coarsening refers to an increase in crystal size while densification necessarily implies the removal of pores and voids. Liquid phase sintering

typically involves 5-30 vol.% liquid.[60] Liquid phase sintering generally occurs in three sequential stages: (1) rearrangement of the nanocrystals within the liquid toincrease packing, (2) solution-precipitation, where atoms at particle contact points dissolve due to high capillary pressure and then re-precipitate in low-pressure regions of solid the particles leading to contact flattening and densification, and (3) a combination of solid phase sintering of the solid particle skeletal network, pore migration, and continuation of solution-precipitation to a lesser degree depending on factors such as liquid content, pore size, and solid-liquid solubility.[60,61] For densification, it is desirable for the liquid phase to wet the solid particles. Solubility of the solid phase in the liquid phase is also desired because liquid diffusivities are higher than solid diffusivities.[59,61] Chemical gradients contribute an additional driving force for boundary motion and coalescence during sintering. Such gradients are present in our films as CZTS transforms into CZTSSe. During annealing using the hot loading method, liquid phase sintering would be active during the time that the substrate temperature lags behind that of the ampule and the selenium vapor. As the temperature lag decreases, the liquid selenium evaporates from the coating. Following, grain growth occurs predominantly by solid state sintering.

To investigate the possibility of liquid phase sintering occurring in the smooth regions of the films annealed by the hot loading method, a CZTS nanocrystal coating was annealed with several pieces of selenium shots placed directly on top of the coating. The annealing conditions were chosen such that, in the absence of these selenium shots on the coating, a uniform film with matte appearance is obtained. Specifically, the film was annealed at 600 ^{o}C in 240 Torr selenium, which is the saturated vapor pressure of selenium at 600 ^{o}C, using the slow ramping method. The mass of selenium charged into the ampule was double the mass necessary to establish the saturated vapor pressure. This was done to ensure that liquid selenium was present during annealing (*i.e.*, 26 mg of selenium was charged into the ampule, such that 13 mg of selenium was present as liquid at 600 ^{o}C). As the temperature increased, the selenium shot melted on the CZTS nanocrystal film, forming a liquid selenium pool that covered the coating partially. Figures 5.17a and 5.17b, show the digital photographs of the film before and after annealing, respectively. The left half of the film, where the selenium shots were placed, exhibits the microstructure that appears smooth (Figure 5.17e) whereas the right half of

the film exhibits the microstructure with matte appearance (Figure 17d). The emergence of the microstructure with smooth appearance where selenium has melted, even though the coatings were annealed using the slow ramping approach, conclusively associates this microstructure with the presence of liquid selenium on the coatings. The size, shape, and location of the region where the smooth microstructure appears are consistent with liquid selenium spreading out towards the left slide of the film after the shots have melted. On the left side we also observe circular patches where the selenium shots were placed. The contrast is due to the grain size between the CZTS film in the circular patches and the regions surrounding the patches. Within the circular patches, the average crystal size (~450 nm) is double that of the surrounding regions (~200 nm). We surmise that the size difference is due to the difference in the amount of time that these regions were exposed to liquid selenium: it is reasonable to hypothesize that the regions within the circular patches, where the selenium shots were placed, were exposed to liquid selenium the longest and therefore exhibit larger grains. As the selenium shots melt, spread and evaporate, the liquid thickness would always be highest where the selenium shots were placed. There is no evidence of elemental selenium remaining in the film: all of the excess selenium eventually condensed on the opposite end of the ampule during the oven cooling stage.

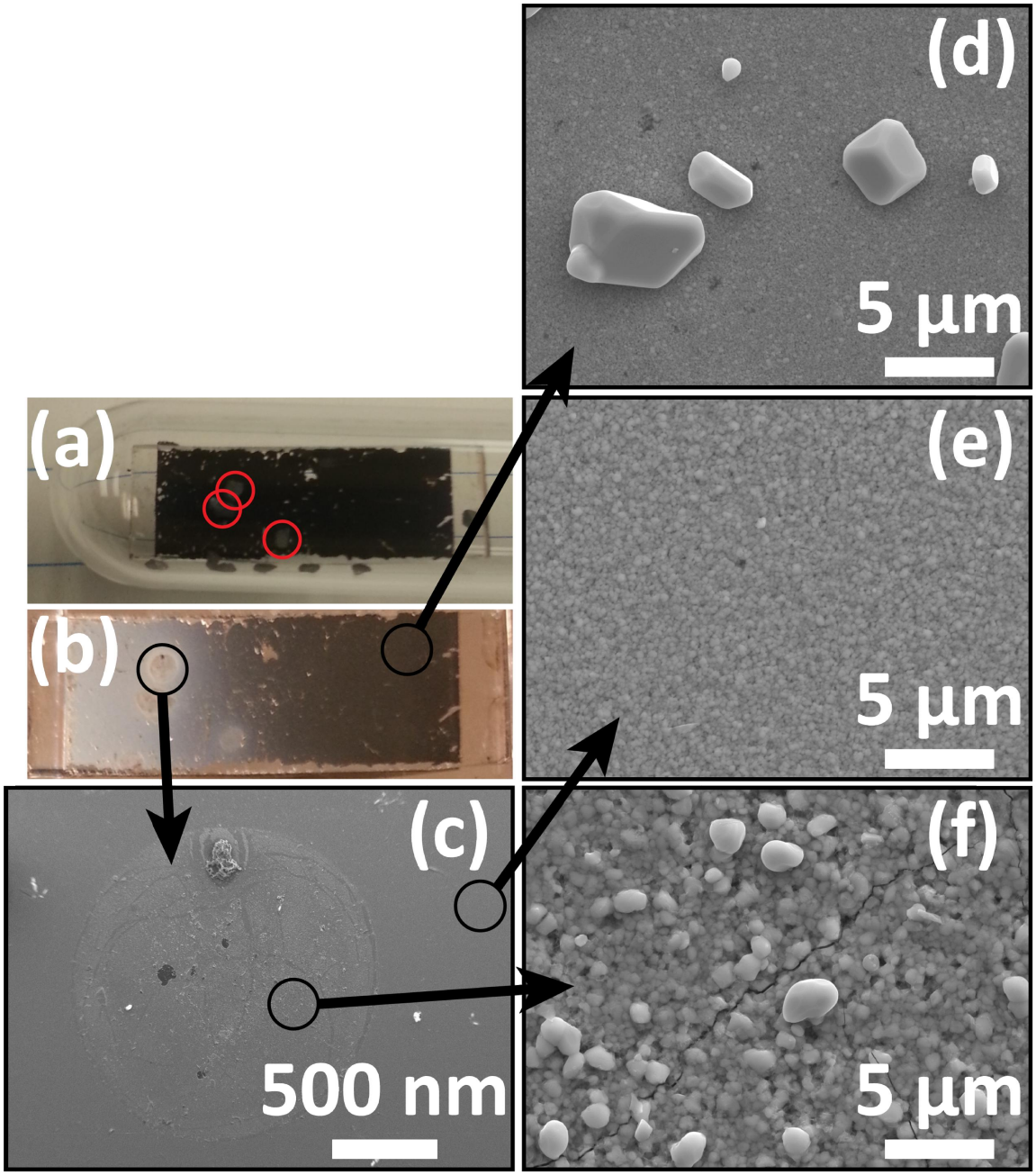

Figure 5.17 Several pieces of the selenium shot (out of 26 mg total; circled in red) were placed on top of the CZTS nanocrystal film prior to annealing, as shown in the digital photograph in (a) where the film is inside the sealed quartz ampule with the selenium. (b) The digital photograph of the film after annealing shows that the left half of the film is different in appearance than the right half of the film, and there are circular patches in the locations where selenium pellets were placed. Plan view SEM images showing (c) a circular patch, (d) the right-half of the film, (e) the shiny region outside of the circular patches, and (f) the microstructure inside of the circular patch.

5.5 Conclusions

Effect of temperature, selenium pressure and heating rate on the microstructure of CZTS films formed by annealing coatings cast from CZTS nanocrystal dispersions was studied in a closed system. Two different types of microstructures were discovered depending on whether the CZTS nanocrystals are exposed to liquid selenium. Films annealed without liquid selenium condensation on the nanocrystal coating develop into a microstructure comprised of micron-size abnormal CZTSSe crystals on top of a nanocrystalline, carbon-rich, CZTSSe floor layer. Significant fraction of carbon, originally present as ligands on the nanocrystals, remains as polymerized $(CSe_{2-x})_n$. The size of the abnormal crystals increases with selenium pressure and temperature. Continuous CZTSSe films with largest CZTSSe crystals were obtained when films were annealed at 700 ^oC in 450 Torr of selenium. This type of microstructure had a matte appearance. In contrast, when liquid selenium is present on the nanocrystal coating during annealing, the nanocrystals in the floor layer grow rapidly and this rapid growth suppresses the abnormal crystal formation. Instead, the floor layer transforms into a dense film with ~1 μm to ~10 μm (~4 μm on average) CZTSSe grains: grain sizes increase with increasing temperature and selenium pressure. This microstructure has a smooth and shiny appearance.

Future experiments could include attempting to develop methods to cover the entire substrate with the smooth microstructure. One way to accomplish this is by evaporating a uniform thin coating of selenium onto the substrate before coating the substrate with CZTS nanocrystals: this layer would melt during annealing and become a source of liquid selenium. Another way is to use a two-zone furnace to keep the substrate at a uniform lower temperature than the zone where the selenium shots are placed. This would induce selenium condensation on the nanocrystals during annealing. Switching the hot and cold zones at the end of the process may be used to evaporate the excess selenium from the film's surface.

5.6 References

1. H. Katagiri, K. Saitoh, T. Washio, H. Shinohara, T. Kurumadani, and S. Miyajima, *Sol. Energ. Mat. Sol. Cells*, 2001, **65**, 141–148.

2. W. Wang, M. T. Winkler, O. Gunawan, T. Gokmen, T. K. Todorov, Y. Zhu, and D. B. Mitzi, *Adv. Energy Mater.*, 2013, 10.1002/aenm.201301465.

3. I. Repins, C. Beall, N. Vora, C. DeHart, D. Kuciauskas, P. Dippo, B. To, J. Mann, W.-C. Hsu, A. Goodrich, and R. Noufi, *Sol. Energ. Mat. Sol. Cells*, 2012, **101**, 154–159.

4. J. B. Li, V. Chawla, and B. M. Clemens, *Adv. Mater.*, 2012, **24**, 720–723.

5. Z. Su, K. Sun, Z. Han, H. Cui, F. Liu, Y. Lai, J. Li, X. Hao, Y. Liu, and M. A. Green, *J. Mater. Chem. A*, 2014, **2**, 500–509.

6. J.-O. Jeon, K. D. Lee, L. Seul Oh, S.-W. Seo, D.-K. Lee, H. Kim, J.-H. Jeong, M. J. Ko, B. Kim, H. J. Son, and J. Y. Kim, *ChemSusChem*, 2014, **7**, 1073–1077.

7. Y. Cao, M. S. Denny, J. V Caspar, W. E. Farneth, Q. Guo, A. S. Ionkin, L. K. Johnson, M. Lu, I. Malajovich, D. Radu, H. D. Rosenfeld, K. R. Choudhury, and W. Wu, *J. Am. Chem. Soc.*, 2012, **134**, 15644–15647.

8. C. K. Miskin, W. C. Yang, C. J. Hages, N. J. Carter, C. S. Joglekar, E. A. Stach, and R. Agrawal, *Prog. Photovoltaics Res. Appl.*, 2014, 10.1002/pip.2472.

9. K. Woo, Y. Kim, W. Yang, K. Kim, I. Kim, Y. Oh, J. Y. Kim, and J. Moon, *Sci. Rep.*, 2013, **3**, 3069.

10. H. Xin, J. K. Katahara, I. L. Braly, and H. W. Hillhouse, *Adv. Energy Mater.*, 2014, 10.1002/aenm.201301823.

11. T. Schnabel, M. Löw, and E. Ahlswede, *Sol. Energ. Mat. Sol. Cells*, 2013, **117**, 324–328.

12. B. D. Chernomordik, A. E. Béland, D. D. Deng, L. F. Francis, and E. S. Aydil, *Chem. Mater.*, 2014, 10.1021/cm500791a.

13. B. Shin, O. Gunawan, Y. Zhu, N. A. Bojarczuk, S. J. Chey, and S. Guha, *Prog. Photovoltaics Res. Appl.*, 2013, **21**, 72–76.

14. A. Redinger, M. Mousel, M. H. Wolter, N. Valle, and S. Siebentritt, *Thin Solid Films*, 2013, **535**, 291–295.

15. S. Chen, A. Walsh, X.-G. Gong, and S.-H. Wei, *Adv. Mater.*, 2013, **25**, 1522–1539.

16. R. Mainz, B. C. Walker, S. S. Schmidt, O. Zander, A. Weber, H. Rodriguez-Alvarez, J. Just, M. Klaus, R. Agrawal, and T. Unold, *Phys. Chem. Chem. Phys.*, 2013, **15**, 18281.

17. G. Wang, W. Zhao, Y. Cui, Q. Tian, S. Gao, L. Huang, and D. Pan, *ACS Appl. Mater. Interfaces*, 2013, **5**, 10042–10047.

18. G. M. Ilari, C. M. Fella, C. Ziegler, A. R. Uhl, Y. E. Romanyuk, and A. N. Tiwari, *Sol. Energ. Mat. Sol. Cells*, 2012, **104**, 125–130.

19. W. Wang, S.-Y. Han, S.-J. Sung, D.-H. Kim, and C.-H. Chang, *Phys. Chem. Chem. Phys.*, 2012, **14**, 11154–11159.

20. S. J. Ahn, C. W. Kim, J. H. Yun, J. Gwak, S. Jeong, B.-H. Ryu, and K. H. Yoon, *J. Phys. Chem. C*, 2010, **114**, 8108–8113.

21. Q. Guo, G. M. Ford, W.-C. Yang, B. C. Walker, E. A. Stach, H. W. Hillhouse, and R. Agrawal, *J. Am. Chem. Soc.*, 2010, **132**, 17384–17386.

22. H. Rau, T. R. N. Kutty, and J. R. F. Guedes De Carvalho, *J. Chem. Thermodyn.*, 1973, **5**, 833–844.

23. H. Rau, *J. Chem. Thermodyn.*, 1974, **6**, 525–535.

24. C. V. Thompson, *J. Appl. Phys.*, 1985, **58**, 763–772.

25. J. van Embden, A. S. R. Chesman, E. Della Gaspera, N. W. Duffy, S. E. Watkins, and J. J. Jasieniak, 2014, 10.1021/ja501218u.

26. A. Khare, B. Himmetoglu, M. Johnson, D. J. Norris, M. Cococcioni, and E. S. Aydil, *J. Appl. Phys.*, 2012, **111**, 083707.

27. K. Wang, O. Gunawan, T. Todorov, B. Shin, S. J. Chey, N. A. Bojarczuk, D. Mitzi, and S. Guha, *Appl. Phys. Lett.*, 2010, **97**, 143508.

28. M. Grossberg, J. Krustok, J. Raudoja, and T. Raadik, *Appl. Phys. Lett.*, 2012, **101**, 102102.

29. M. Grossberg, J. Krustok, J. Raudoja, K. Timmo, M. Altosaar, and T. Raadik, *Thin Solid Films*, 2010, **519**, 7403–7406.

30. A. Fairbrother, X. Fontané, V. Izquierdo-Roca, M. Placidi, D. Sylla, M. Espindola-Rodriguez, S. Marino-Lopez, F. A. Pulgarin, O. Vigil-Galán, A. Perez-Rodriguez, and E. Saucedo, *Prog. Photovoltaics Res. Appl.*, 2014, **22**, 479–487.

31. J. He, L. Sun, S. Chen, Y. Chen, P. Yang, and J. Chu, *J. Alloys Compd.*, 2012, **511**, 129–132.

32. A. Khare, B. Himmetoglu, M. Cococcioni, and E. S. Aydil, *J. Appl. Phys.*, 2012, **111**, 123704.

33. A.-J. Cheng, M. Manno, A. Khare, C. Leighton, S. A. Campbell, and E. S. Aydil, *J. Vac. Sci. Technol. A*, 2011, **29**, 051203.

34. M. Ganchev, J. Iljina, L. Kaupmees, T. Raadik, O. Volobujeva, A. Mere, M. Altosaar, J. Raudoja, and E. Mellikov, *Thin Solid Films*, 2011, **519**, 7394–7398.

35. Y. C. Cheng, C. Q. Jin, F. Gao, X. L. Wu, W. Zhong, S. H. Li, and P. K. Chu, *J. Appl. Phys.*, 2009, **106**, 123505.

36. Z. Levi, I. Bineva, and D. Nesheva, *Acta Phys. Pol. A*, 2009, **116**, 75–77.

37. P. A. Fernandes, P. M. P. Salomé, and A. F. da Cunha, *J. Alloys Compd.*, 2011, **509**, 7600–7606.

38. C. Wang, *Chem. Phys. Lett.*, 2002, **357**, 371–375.

39. H. R. Chandrasekhar and R. G. Humphreys, *Phys. Rev. B*, 1977, **15**, 2177–2183.

40. A. J. Smith, P. E. Meek, and L. W. Y, *J. Phys. C Solid State Phys.*, 1977, **10**, 1321–1333.

41. V. Izquierdo-Roca, A. Pérez-Rodríguez, A. Romano-Rodríguez, J. R. Morante, J. Álvarez-García, L. Calvo-Barrio, V. Bermudez, P. P. Grand, O. Ramdani, L. Parissi, and O. Kerrec, *J. Appl. Phys.*, 2007, **101**, 103517.

42. C. Xue, D. Papadimitriou, Y. S. Raptis, W. Richter, N. Esser, S. Siebentritt, and M. C. Lux-Steiner, *J. Appl. Phys.*, 2004, **96**, 1963.

43. P. A. Fernandes, P. M. P. Salomé, and A. F. da Cunha, *J. Phys. D. Appl. Phys.*, 2010, **43**, 215403.

44. C. G. Munce, G. K. Parker, S. a. Holt, and G. a. Hope, *Colloids Surfaces A*, 2007, **295**, 152–158.

45. T. P. Mernagh and A. G. Trudu, *Chem. Geol.*, 1993, **103**, 113–127.

46. P. a. Fernandes, M. G. Sousa, P. M. P. Salomé, J. P. Leitão, and A. F. da Cunha, *CrystEngComm*, 2013, **15**, 10278.

47. C. Wang and A. Manthiram, *ACS Sustain. Chem. Eng.*, 2014, **2**, 561–568.

48. I. Klugius, R. Miller, A. Quintilla, T. M. Friedlmeier, D. Blázquez-Sánchez, E. Ahlswede, and M. Powalla, *Phys. status solidi - Rapid Res. Lett.*, 2012, **6**, 297–299.

49. A. Niemegeers, M. Burgelman, and A. De Vos, *Appl. Phys. Lett.*, 1995, **67**, 843–845.

50. D. J. G. Ives, R. W. Pittman, and W. Wardlaw, *J. Chem. Soc.*, 1947, 1080–1083.

51. Y. Wang, D. C. Alsmeyer, and R. L. McCreery, *Chem. Mater.*, 1990, **2**, 557–563.

52. P. K. Chu and L. Li, *Mater. Chem. Phys.*, 2006, **96**, 253–277.

53. Z. Iqbal, S. T. Correale, F. Reidinger, R. H. Baughman, and Y. Okamoto, *J. Chem. Phys.*, 1988, **88**, 4492–4497.

54. M. Johnson, S. V Baryshev, E. Thimsen, M. Manno, X. Zhang, I. V Veryovkin, C. Leighton, and E. S. Aydil, *Energy Environ. Sci.*, 10.1039/c3ee44130j.

55. P. C. Hiemenz and R. Rajagopalan, in *Principles of Colloid and Surface Chemistry*, eds. P. C. Hiemenz and R. Rajagopalan, Taylor & Francis, Boca Raton, Florida, 3rd edn., 1997, pp. 437–439.

56. Z. Gemici, P. I. Schwachulla, E. H. Williamson, M. F. Rubner, and R. E. Cohen, *Nano Lett.*, 2009, **9**, 1064–1070.

57. B. S. Tosun, B. D. Chernomordik, A. Gunawan, B. Williams, K. A. Mkhoyan, L. F. Francis, and E. S. Aydil, *Chem. Commun.*, 2013, **49**, 3549–3551.

58. A. C. Ferrari and J. Robertson, *Phys. Rev. B*, 2000, **61**, 14095–14107.

59. R. M. German, *Liquid Phase Sintering*, Plenum Press, 1985.

60. R. M. German, P. Suri, and S. J. Park, *J. Mater. Sci.*, 2009, **44**, 1–39.

61. W. D. Kingery, *J. Appl. Phys.*, 1959, **30**, 301–306.

COMPREHENSIVE BIBLIOGRAPHY

Chapter 1

1. International Energy Outlook 2013, U.S. Energy Information Administration Energy, U.S. Department of Energy, Washington, DC, 2013.
2. S. Solomon, D. Qin, M. Manning, Z. Chen, M. Marquis, K. B. Averyt, M. Tignor, and H. L. Miller, Fourth Assessment Report of the Intergovernmental Panel on Climate Change, Cambridge University Press, Cambridge, UK, 2007.
3. Fifth Assessment Report of the Intergovernmental Panel on Climate Change, Cambridge University Press, Cambridge, UK, 2014.
4. M. I. Hoffert, K. Caldeira, A. K. Jain, E. F. Haites, L. D. D. Harvey, S. D. Potter, M. E. Schlesinger, S. H. Schneider, R. G. Watts, T. M. L. Wigley, and D. J. Wuebbles, Nature, 1998, 395, 881.
5. C. A. Wolden, J. Kurtin, J. B. Baxter, I. Repins, S. E. Shaheen, J. T. Torvik, A. A. Rockett, V. M. Fthenakis, and E. S. Aydil, J. Vac. Sci. Technol. A, 2011, 29, 030801.
6. N. S. Lewis, MRS Bull., 2007, 32, 808.
7. D. J. Norris and E. S. Aydil, Science, 2012, 338, 625–626.
8. S. Abermann, Sol. Energy, 2013, 94, 37–70.
9. A. Jaeger-Waldau, Joint Research Centre, PV Status Report 2010, Office for Official Publications of the European Union, Brussels, 2010.
10. International Energy Outlook 2010, U.S. Energy Information Administration, U.S. Department of Energy, Washington, DC, 2010.

11. A. Hagfeldt, G. Boschloo, L. Sun, L. Kloo, and H. Pettersson, Chem. Rev., 2010, 110, 6595–6663.

12. H. J. Snaith, J. Phys. Chem. Lett., 2013, 4, 3623–3630.

13. F. Dross, K. Baert, T. Bearda, J. Deckers, V. Depauw, O. El Daif, I. Gordon, A. Gougam, J. Govaerts, S. Granata, R. Labie, X. Loozen, R. Martini, A. Masolin, B. O'Sullivan, Y. Qiu, J. Vaes, D. Van Gestel, J. Van Hoeymissen, A. Vanleenhove, K. Van Nieuwenhuysen, S. Venkatachalam, M. Meuris, and J. Poortmans, Prog. Photovolt: Res. Appl., 2012, 20, 770–784.

14. A. Henemann, Renew. Energy Focus, 2008, 9, 14–19.

15. T. Dullweber, G. Hanna, U. Rau, and H. W. Schock, Sol. Energ. Mat. Sol. C., 2001, 67, 145–150.

16. W. Shockley and H. J. Queisser, J. Appl. Phys., 1961, 32, 510–519.

17. K. Nagaich, S. Campbell, and E. Aydil, Photovolt. Spec. Conf. (PVSC), 2011 37th IEEE, 2011, 425–429.

18. S. Delbos, EPJ Photovoltaics, 2012, 3, 35004.

19. S. Siebentritt, M. Igalson, C. Persson, and S. Lany, Prog. Photovolt: Res. Appl., 2010, 18, 390–410.

20. S. Abermann, Sol. Energy, 2013, 94, 37–70.

21. C. Wadia, A. P. Alivisatos, and D. M. Kammen, Environ. Sci. Technol., 2009, 43, 2072–2077.

22. D. L. Staebler and C. R. Wronski, Appl. Phys. Lett., 1977, 31, 292–294.

23. B. A. Andersson, Prog. Photovolt: Res. Appl., 2000, 8, 61–76.

24. G. B. Haxel, J. B. Hedrick, G. J. Orris, P. H. Stauffer, and H. W. I. Hendley, Fact Sheet 087-02: Rare Earth Elements-Critical Resources for High Technology, U.S. Geological Survey, 2002.

25. Abundance of elements in Earth's crust, Wikipedia, 2014.

26. H. Katagiri, K. Jimbo, S. Yamada, T. Kamimura, W. S. Maw, T. Fukano, T. Ito, and T. Motohiro, Appl. Phys. Express, 2008, 1, 041201.

27. S. Chen, X. G. Gong, A. Walsh, and S.-H. Wei, Appl. Phys. Lett., 2009, 94, 041903.

28. K. Timmo, M. Altosaar, J. Raudoja, K. Muska, M. Pilvet, M. Kauk, T. Varema, M. Danilson, O. Volobujeva, and E. Mellikov, Sol. Energ. Mat. Sol. C., 2010, 94, 1889–1892.

29. S. Chen, A. Walsh, X.-G. Gong, and S.-H. Wei, Adv. Mater., 2013, 25, 1522–1539.

30. W. Wang, M. T. Winkler, O. Gunawan, T. Gokmen, T. K. Todorov, Y. Zhu, and D. B. Mitzi, Adv. Energy Mater., 2013, 10.1002/aenm.201301465.

31. K. Ito and T. Nakazawa, Jpn. J. Appl. Phys., 1988, 27, 2094–2097.

Chapter 2

1. J. J. Scragg, Copper Zinc Tin Sulfide Thin Films for Photovoltaics: Synthesis and Characterisation by Electrochemical Methods, Springer-Verlag, Berlin/Heidelberg, 2011.

2. V. A. Akhavan, Ph.D. Thesis, University of Texas at Austin, 2011.

3. K. Moriya, K. Tanaka, and H. Uchiki, Jpn. J. Appl. Phys., 2007, 46, 5780–5781.

4. K. Ramasamy, M. A. Malik, and P. O'Brien, Chem. Sci., 2011, 2, 1170–1172.

5. E. Thimsen, S. C. Riha, S. V Baryshev, A. B. F. Martinson, J. W. Elam, and M. J. Pellin, Chem. Mater., 2012, 24, 3188–3196.

6. H. Katagiri, N. Sasaguchi, S. Hando, S. Hoshino, J. Ohashi, and T. Yokota, Sol. Energ. Mat. Sol. C., 1997, 49, 407–414.

7. H. Katagiri, K. Saitoh, T. Washio, H. Shinohara, T. Kurumadani, and S. Miyajima, Sol. Energ. Mat. Sol. C., 2001, 65, 141–148.

8. H. Katagiri, Thin Solid Films, 2005, 480-481, 426–432.

9. T. Tanaka, D. Kawasaki, M. Nishio, Q. Guo, and H. Ogawa, Phys. Status Solidi C, 2006, 3, 2844–2847.

10. B.-A. Schubert, B. Marsen, S. Cinque, T. Unold, R. Klenk, S. Schorr, and H. W. Schock, Prog. Photovolt: Res. Appl., 2011, 19, 93–96.

11. M. Bär, B.-A. Schubert, B. Marsen, R. G. Wilks, S. Pookpanratana, M. Blum, S. Krause, T. Unold, W. Yang, L. Weinhardt, C. Heske, and H.-W. Schock, Appl. Phys. Lett., 2011, 99, 222105.

12. K. Wang, O. Gunawan, T. Todorov, B. Shin, S. J. Chey, N. A. Bojarczuk, D. Mitzi, and S. Guha, Appl. Phys. Lett., 2010, 97, 143508.

13. T. Tanaka, T. Nagatomo, D. Kawasaki, M. Nishio, Q. Guo, A. Wakahara, A. Yoshida, and H. Ogawa, J. Phys. Chem. Solids, 2005, 66, 1978–1981.

14. K. Jimbo, R. Kimura, T. Kamimura, S. Yamada, W. S. Maw, H. Araki, K. Oishi, and H. Katagiri, Thin Solid Films, 2007, 515, 5997–5999.

15. H. Katagiri, K. Jimbo, S. Yamada, T. Kamimura, W. S. Maw, T. Fukano, T. Ito, and T. Motohiro, Appl. Phys. Express, 2008, 1, 041201.

16. H. Katagiri, K. Jimbo, M. Tahara, H. Araki, and K. Oishi, Mater. Res. Soc. Symp. Proc., 2009, 1165, M04–01.

17. P. A. Fernandes, P. M. P. Salomé, and A. F. da Cunha, Semicond. Sci. Technol., 2009, 24, 105013.

18. H. Yoo and J. Kim, Thin Solid Films, 2010, 518, 6567–6572.

19. N. Momose, M. T. Htay, T. Yudasaka, S. Igarashi, T. Seki, S. Iwano, Y. Hashimoto, and K. Ito, Jpn. J. Appl. Phys., 2011, 50, 01BG09.

20. M. Johnson, S. V. Baryshev, E. Thimsen, M. Manno, X. Zhang, I. V. Veryovkin, C. Leighton, and E. S. Aydil, Energy Environ. Sci., 2014, 10.1039/c3ee44130j.

21. T. K. Todorov, J. Tang, S. Bag, O. Gunawan, T. Gokmen, Y. Zhu, and D. B. Mitzi, Adv. Energy Mater., 2013, 3, 34.

22. W. Wang, M. T. Winkler, O. Gunawan, T. Gokmen, T. K. Todorov, Y. Zhu, and D. B. Mitzi, Adv. Energy Mater., 2013, 10.1002/aenm.201301465.

23. T. Todorov and D. B. Mitzi, Eur. J. Inorg. Chem., 2010, 2010, 17–28.

24. C. M. Fella, A. R. Uhl, Y. E. Romanyuk, and A. N. Tiwari, Phys. Status Solidi A, 2012, 209, 1043–1048.

25. Y. Sun, K. Zong, H. Zheng, H. Wang, J. Liu, H. Yan, and M. Zhu, Mater. Lett., 2013, 92, 195–197.

26. G. M. Ilari, C. M. Fella, C. Ziegler, A. R. Uhl, Y. E. Romanyuk, and A. N. Tiwari, Sol. Energ. Mat. Sol. C., 2012, 104, 125–130.

27. K. Tanaka, M. Oonuki, N. Moritake, and H. Uchiki, Sol. Energ. Mat. Sol. C., 2009, 93, 583–587.

28. K. Maeda, K. Tanaka, Y. Nakano, and H. Uchiki, Jpn. J. Appl. Phys., 2011, 50, 05FB08.

29. A. Fischereder, T. Rath, W. Haas, H. Amenitsch, J. Albering, D. Meischler, S. Larissegger, M. Edler, R. Saf, F. Hofer, and G. Trimmel, Chem. Mater., 2010, 22, 3399–3406.

30. M. Kurokawa, K. Tanaka, K. Moriya, and H. Uchiki, Jpn. J. Appl. Phys., 2012, 51, 10NC33.

31. W. Ki and H. W. Hillhouse, Adv. Energy Mater., 2011, 1, 732–735.

32. T. Schnabel, M. Löw, and E. Ahlswede, Sol. Energ. Mat. Sol. C., 2013, 117, 324–328.

33. H. Xin, J. K. Katahara, I. L. Braly, and H. W. Hillhouse, Adv. Energy Mater., 2014, 10.1002/aenm.201301823.

34. W. Yang, H.-S. Duan, B. Bob, H. Zhou, B. Lei, C.-H. Chung, S.-H. Li, W. W. Hou, and Y. Yang, Adv. Mater., 2012, 24, 6323–6329.

35. S.-N. Park, S.-J. Sung, D.-H. Son, D.-W. Kim, M. Gansukh, H. Cheong, and J.-K. Kang, RSC Adv., 2014, 4, 9118–9125.

36. A. R. Uhl, C. Fella, A. Chirilă, M. R. Kaelin, L. Karvonen, A. Weidenkaff, C. N. Borca, D. Grolimund, Y. E. Romanyuk, and A. N. Tiwari, Prog. Photovolt: Res. Appl., 2012, 20, 526–533.

37. G. Wang, W. Zhao, Q. Tian, L. Huang, D. Pan, Y. Cui, and S. Gao, ACS Appl. Mater. Interfaces, 2013, 5, 10042–10047.

38. D. B. Mitzi, O. Gunawan, T. K. Todorov, K. Wang, and S. Guha, Sol. Energ. Mat. Sol. C., 2011, 95, 1421–1436.

39. T. Todorov, H. Sugimoto, O. Gunawan, T. Gokmen, and D. B. Mitzi, IEEE J. Photovolt., 2014, 4, 483–485.

40. Z. Su, K. Sun, Z. Han, H. Cui, F. Liu, Y. Lai, J. Li, X. Hao, Y. Liu, and M. A. Green, J. Mater. Chem. A, 2014, 2, 500–509.

41. N. Kamoun, H. Bouzouita, and B. Rezig, Thin Solid Films, 2007, 515, 5949–5952.

42. N. Nakayama and K. Ito, Appl. Surf. Sci., 1996, 92, 171–175.

43. K. Maeda, K. Tanaka, Y. Fukui, and H. Uchiki, Sol. Energ. Mat. Sol. C., 2011, 95, 2855–2860.

44. J. J. Scragg, T. Ericson, T. Kubart, M. Edoff, and C. Platzer-Björkman, Chem. Mater., 2011, 23, 4625–4633.

45. B. D. Chernomordik, A. E. Béland, D. D. Deng, L. F. Francis, and E. S. Aydil, Chem. Mater., 2014, 10.1021/cm500791a.

46. C. Leidholm, C. Hotz, A. Breeze, C. Sunderland, and W. Ki, NREL Subcontract Rep., 2012, NREL/SR–5200–56501.

47. C. Steinhagen, M. G. Panthani, V. Akhavan, B. Goodfellow, B. Koo, and B. A. Korgel, J. Am. Chem. Soc., 2009, 131, 12554–5.

48. Q. Guo, H. W. Hillhouse, and R. Agrawal, J. Am. Chem. Soc., 2009, 131, 11672–11673.

49. B. D. Chernomordik, A. E. Béland, N. D. Trejo, A. A. Gunawan, D. D. Deng, K. A. Mkhoyan, and E. S. Aydil, J. Mater. Chem. A, 2014, 10.1039/C4TA01658K.

50. S. C. Riha, B. A. Parkinson, and A. L. Prieto, J. Am. Chem. Soc., 2009, 131, 12054–12055.

51. Q. Guo, G. M. Ford, W.-C. Yang, B. C. Walker, E. A. Stach, H. W. Hillhouse, and R. Agrawal, J. Am. Chem. Soc., 2010, 132, 17384–17386.

52. A. Singh, H. Geaney, F. Laffir, and K. M. Ryan, J. Am. Chem. Soc., 2012, 134, 2910–2913.

53. A. Shavel, J. Arbiol, and A. Cabot, J. Am. Chem. Soc., 2010, 132, 4514–4515.

54. Y. Liu, D. Yao, L. Shen, H. Zhang, X. Zhang, and B. Yang, J. Am. Chem. Soc., 2012, 134, 7207–7210.

55. Y. Cao, M. S. Denny, J. V Caspar, W. E. Farneth, Q. Guo, A. S. Ionkin, L. K. Johnson, M. Lu, I. Malajovich, D. Radu, H. D. Rosenfeld, K. R. Choudhury, and W. Wu, J. Am. Chem. Soc., 2012, 134, 15644–15647.

56. C. K. Miskin, W. C. Yang, C. J. Hages, N. J. Carter, C. S. Joglekar, E. A. Stach, and R. Agrawal, Prog. Photovolt: Res. Appl., 2014, 10.1002/pip.2472.

57. G. Wang, W. Zhao, Y. Cui, Q. Tian, S. Gao, L. Huang, and D. Pan, ACS Appl. Mater. Interfaces, 2013, 5, 10042–10047.

58. Q. Guo, G. M. Ford, W.-C. Yang, C. J. Hages, H. W. Hillhouse, and R. Agrawal, Sol. Energ. Mat. Sol. C., 2012, 105, 132–136.

59. R. Mainz, B. C. Walker, S. S. Schmidt, O. Zander, A. Weber, H. Rodriguez-Alvarez, J. Just, M. Klaus, R. Agrawal, and T. Unold, Phys. Chem. Chem. Phys., 2013, 15, 18281.

60. W. Wang, S.-Y. Han, S.-J. Sung, D.-H. Kim, and C.-H. Chang, Phys. Chem. Chem. Phys., 2012, 14, 11154–11159.

61. Q. Guo, G. M. Ford, H. W. Hillhouse, and R. Agrawal, Nano Lett., 2009, 9, 3060–3065.

62. Q. Tian, X. Xu, L. Han, M. Tang, R. Zou, Z. Chen, M. Yu, J. Yang, and J. Hu, CrystEngComm, 2012, 14, 3847.

63. M. Lu, Y. Cao, J. V Caspar, I. Malajovich, D. Radu, and H. D. Rosenfeld, 2011 37th IEEE Photovolt. Spec. Conf., 2011, 000402–000406.

64. J.-O. Jeon, K. D. Lee, L. Seul Oh, S.-W. Seo, D.-K. Lee, H. Kim, J.-H. Jeong, M. J. Ko, B. Kim, H. J. Son, and J. Y. Kim, ChemSusChem, 2014, 7, 1073–1077.

65. S. Ahmed, K. B. Reuter, O. Gunawan, L. Guo, L. T. Romankiw, and H. Deligianni, Adv. Energy Mater., 2012, 2, 253–259.

Chapter 3

1. C. A. Wolden, J. Kurtin, J. B. Baxter, I. Repins, S. E. Shaheen, J. T. Torvik, A. A. Rockett, V. M. Fthenakis, and E. S. Aydil, J. Vac. Sci. Technol. A, 2011, 29, 030801.

2. S. Abermann, Sol. Energy, 2013, 94, 37–70.

3. W. C. Liu, B. L. Guo, X. S. Wu, F. M. Zhang, C. L. Mak, and K. H. Wong, J. Mater. Chem. A, 2013, 1, 3182–3186.

4. M. Cao and Y. Shen, J. Cryst. Growth, 2011, 318, 1117–1120.

5. B. Flynn, W. Wang, C. Chang, and G. S. Herman, Phys. Status Solidi A, 2012, 209, 2186–2194.

6. S. W. Shin, J. H. Han, Y. C. Park, G. L. Agawane, C. H. Jeong, J. H. Yun, a. V. Moholkar, J. Y. Lee, and J. H. Kim, J. Mater. Chem., 2012, 22, 21727–21732.

7. Q. Guo, H. W. Hillhouse, and R. Agrawal, J. Am. Chem. Soc., 2009, 131, 11672–11673.

8. K.-L. Ou, J.-C. Fan, J.-K. Chen, C.-C. Huang, L.-Y. Chen, J.-H. Ho, and J.-Y. Chang, J. Mater. Chem., 2012, 22, 14667–14673.

9. C. Zou, L. Zhang, D. Lin, Y. Yang, Q. Li, X. Xu, X. Chen, and S. Huang, CrystEngComm, 2011, 13, 3310–3313.

10. A. Khare, A. W. Wills, L. M. Ammerman, D. J. Norris, and E. S. Aydil, Chem. Commun., 2011, 47, 11721–11723.

11. T. J. Pundsack, B. D. Chernomordik, A. E. Béland, E. S. Aydil, and D. A. Blank, J. Phys. Chem. Lett., 2013, 4, 2711–2714.

12. R. D. Deegan, O. Bakajin, T. F. Dupont, G. Huber, S. R. Nagel, and T. A. Witten, Nature, 1997, 389, 827–829.

13. B. D. Chernomordik, A. E. Béland, D. D. Deng, L. F. Francis, and E. S. Aydil, Chem. Mater., 2014, 10.1021/cm500791a.

14. B. S. Tosun, C. Pettit, S. A. Campbell, and E. S. Aydil, ACS Appl. Mater. Interfaces, 2012, 4, 3676–3684.

15. M. J. Behr, K. A. Mkhoyan, and E. S. Aydil, ACS Nano, 2010, 4, 5087–5094.

16. K. S. Leschkies, R. Divakar, J. Basu, E. Enache-Pommer, J. E. Boercker, C. B. Carter, U. R. Kortshagen, D. J. Norris, and E. S. Aydil, Nano Lett., 2007, 7, 1793–1798.

17. Y. K. Jung, J. Il Kim, and J.-K. Lee, J. Am. Chem. Soc., 2010, 132, 178–184.

18. D. Pan, L. An, Z. Sun, W. Hou, Y. Yang, Z. Yang, and Y. Lu, J. Am. Chem. Soc., 2008, 130, 5620–5621.

19. W. Niu, S. Wu, and S. Zhang, J. Mater. Chem., 2011, 21, 10894–10902.

20. H. Wu, Y. Yang, and Y. C. Cao, J. Am. Chem. Soc., 2006, 128, 16522–16523.

21. M. A. Malik, M. Afzaal, and P. O'Brien, Chem. Rev., 2010, 110, 4417–4446.

22. K. Ramasamy, M. A. Malik, and P. O'Brien, Chem. Sci., 2011, 2, 1170–1172.

23. A.-J. Cheng, M. Manno, A. Khare, C. Leighton, S. A. Campbell, and E. S. Aydil, J. Vac. Sci. Technol. A, 2011, 29, 051203.

24. A. Khare, B. Himmetoglu, M. Johnson, D. J. Norris, M. Cococcioni, and E. S. Aydil, J. Appl. Phys., 2012, 111, 083707.

25. A. Pein, M. Baghbanzadeh, T. Rath, W. Haas, E. Maier, H. Amenitsch, F. Hofer, C. O. Kappe, and G. Trimmel, Inorg. Chem., 2011, 50, 193–200.

26. X. Lu, Z. Zhuang, Q. Peng, and Y. Li, Chem. Commun., 2011, 47, 3141–3143.

27. A. Singh, H. Geaney, F. Laffir, and K. M. Ryan, J. Am. Chem. Soc., 2012, 134, 2910–2913.

28. M. D. Regulacio, C. Ye, S. H. Lim, M. Bosman, E. Ye, S. Chen, Q.-H. Xu, and M.-Y. Han, Chemistry, 2012, 18, 3127–3131.

29. M. Li, W.-H. Zhou, J. Guo, Y.-L. Zhou, Z.-L. Hou, J. Jiao, Z.-J. Zhou, Z.-L. Du, and S.-X. Wu, J. Phys. Chem. C, 2012, 116, 26507–26516.

30. S. Chen, A. Walsh, Y. Luo, J.-H. Yang, X. G. Gong, and S.-H. Wei, Phys. Rev. B, 2010, 82, 195203.

31. D. Bersani, P. P. Lottici, and X.-Z. Ding, Appl. Phys. Lett., 1998, 72, 73–75.

32. D. Dumcenco and Y. Huang, Opt. Mater., 2013, 35, 419–425.

33. A. F. Routh, Rep. Prog. Phys., 2013, 76, 046603.

34. W. P. Lee and A. F. Routh, Langmuir, 2004, 20, 9885–9888.

35. M. S. Tirumkudulu and W. B. Russel, Langmuir, 2004, 20, 2947–2961.

36. K. Singh and M. Tirumkudulu, Phys. Rev. Lett., 2007, 98, 218302.

37. M. S. Tirumkudulu and W. B. Russel, Langmuir, 2005, 21, 4938–4948.

38. T. Kanai and T. Sawada, Langmuir, 2009, 25, 13315–13317.

39. J. M. Luther, M. Law, Q. Song, C. L. Perkins, M. C. Beard, and A. J. Nozik, ACS Nano, 2008, 2, 271–280.

40. Q. Guo, G. M. Ford, W.-C. Yang, B. C. Walker, E. A. Stach, H. W. Hillhouse, and R. Agrawal, J. Am. Chem. Soc., 2010, 132, 17384–17386.

Chapter 4

1. K. Ito and T. Nakazawa, Jpn. J. Appl. Phys., 1988, 27, 2094–2097.

2. C. A. Wolden, J. Kurtin, J. B. Baxter, I. Repins, S. E. Shaheen, J. T. Torvik, A. A. Rockett, V. M. Fthenakis, and E. S. Aydil, J. Vac. Sci. Technol. A, 2011, 29, 030801.

3. W. Wang, M. T. Winkler, O. Gunawan, T. Gokmen, T. K. Todorov, Y. Zhu, and D. B. Mitzi, Adv. Energy Mater., 2013, 10.1002/aenm.201301465.

4. K. Wang, O. Gunawan, T. Todorov, B. Shin, S. J. Chey, N. A. Bojarczuk, D. Mitzi, and S. Guha, Appl. Phys. Lett., 2010, 97, 143508.

5. I. Repins, C. Beall, N. Vora, C. DeHart, D. Kuciauskas, P. Dippo, B. To, J. Mann, W.-C. Hsu, A. Goodrich, and R. Noufi, Sol. Energ. Mat. Sol. C., 2012, 101, 154–159.

6. A.-J. Cheng, M. Manno, A. Khare, C. Leighton, S. A. Campbell, and E. S. Aydil, J. Vac. Sci. Technol. A, 2011, 29, 051203.

7. H. Katagiri, N. Sasaguchi, S. Hando, S. Hoshino, J. Ohashi, and T. Yokota, Sol. Energ. Mat. Sol. C., 1997, 49, 407–414.

8. H. W. Hillhouse and M. C. Beard, Curr. Opin. Colloid Interface Sci., 2009, 14, 245–259.

9. V. A. Akhavan, B. W. Goodfellow, M. G. Panthani, C. Steinhagen, T. B. Harvey, C. J. Stolle, and B. A. Korgel, J. Solid State Chem., 2012, 189, 2–12.

10. Q. Guo, H. W. Hillhouse, and R. Agrawal, J. Am. Chem. Soc., 2009, 131, 11672–11673.

11. A. Khare, A. W. Wills, L. M. Ammerman, D. J. Norris, and E. S. Aydil, Chem. Commun., 2011, 47, 11721–11723.

12. Q. Guo, G. M. Ford, W.-C. Yang, B. C. Walker, E. A. Stach, H. W. Hillhouse, and R. Agrawal, J. Am. Chem. Soc., 2010, 132, 17384–17386.

13. D.-Y. Peng and J. Zhao, J. Chem. Thermodyn., 2001, 33, 1121–1131.

14. H. Rau, T. R. N. Kutty, and J. R. F. Guedes De Carvalho, J. Chem. Thermodyn., 1973, 5, 833–844.

15. B. Meyer, Chem. Rev., 1976, 76, 367–388.

16. C. V. Thompson, J. Appl. Phys., 1985, 58, 763–772.

17. C. V Thompson, Annu. Rev. Mater. Sci., 1990, 20, 245–268.

18. M. W. Barsoum, in Fundamentals of Ceramics, Taylor & Francis, Boca Raton, Florida, 2002, pp. 302–355.

19. C. L. Yaws, P. Narasimhan K., and C. Gabbula, Yaws' Handbook of Antoine Coefficients for Vapor Pressure, Knovel, 2nd edn., 2009.

20. D. J. Chakrabarti and D. E. Laughlin, Bull. Alloy Phase Diagrams, 1983, 4, 254–271.

21. A. Khare, B. Himmetoglu, M. Johnson, D. J. Norris, M. Cococcioni, and E. S. Aydil, J. Appl. Phys., 2012, 111, 083707.

22. X. Zhang, M. Manno, A. Baruth, M. Johnson, E. S. Aydil, and C. Leighton, ACS Nano, 2013, 7, 2781–2789.

23. T. Gürel, C. Sevik, and T. Çağın, Phys. Rev. B, 2011, 84, 205201.

24. D. Dumcenco and Y. Huang, Opt. Mater., 2013, 35, 419–425.

25. B. S. Tosun, B. D. Chernomordik, A. Gunawan, B. Williams, K. A. Mkhoyan, L. F. Francis, and E. S. Aydil, Chem. Commun., 2013, 49, 3549–3551.

26. R. Mainz, B. C. Walker, S. S. Schmidt, O. Zander, A. Weber, H. Rodriguez-Alvarez, J. Just, M. Klaus, R. Agrawal, and T. Unold, Phys. Chem. Chem. Phys., 2013, 15, 18281.

27. Q. Guo, G. M. Ford, W.-C. Yang, C. J. Hages, H. W. Hillhouse, and R. Agrawal, Sol. Energ. Mat. Sol. C., 2012, 105, 132–136.

28. C. M. Fella, A. R. Uhl, Y. E. Romanyuk, and A. N. Tiwari, Phys. Status Solidi A, 2012, 209, 1043–1048.

29. F. Liu and R. Kirchheim, J. Cryst. Growth, 2004, 264, 385–391.

30. F. Humphreys and M. Hatherly, in Recrystallization and Related Annealing Phenomena, ed. D. Sleeman, Elsevier Ltd, Oxford, Kidlington, UK, 2nd edn., 2004, pp. 368–378.

31. F. Inam, H. Yan, T. Peijs, and M. J. Reece, Compos. Sci. Technol., 2010, 70, 947–952.

32. W. J. Moore and E. L. Williams, Discuss. Faraday Soc., 1959, 28, 86–93.

33. W. C. Hagel, P. J. Jorgensen, and D. S. Tomalin, J. Am. Ceram. Soc., 1966, 49, 23–26.

34. C. Ting and H. Lu, J. Am. Ceram. Soc., 1999, 82, 841–848.

35. T. Bansagi, E. A. Secco, O. K. Srivastava, and R. R. Martin, Can. J. Chem., 1968, 46, 2881–2886.

36. C. E. Birchenall, in Geochemical Transport and Kinetics, eds. A. W. Hofmann, B. J. Giletti, H. S. J. Yoder, and R. A. Yund, Carnegie Institution of Washington, 1974, pp. 53–59.

37. D. A. Stevenson, in Atomic Diffusion in Semiconductors, ed. D. Shaw, Springer US, Boston, MA, 1973, pp. 431–541.

38. M. N. Rahaman, in Ceramic Processing and Sintering, ed. M. N. Rahaman, CRC Press, New York, 2nd edn., 2003, pp. 800–815.

39. S.-H. Wei, S. B. Zhang, and A. Zunger, J. Appl. Phys., 1999, 85, 7214–7218.

40. D. Schmid, M. Ruckh, and H. Schock, Sol. Energ. Mat. Sol. C., 1996, 41-42, 281–294.

41. D. Braunger, D. Hariskos, G. Bilger, U. Rau, and H. W. Schock, Thin Solid Films, 2000, 361-362, 161–166.

42. A. Rockett, J. S. Britt, T. Gillespie, C. Marshall, M. M. Al Jassim, and F. Hasoon, Thin Solid Films, 2000, 372, 212–217.

43. T. Prabhakar and N. Jampana, Sol. Energ. Mat. Sol. C., 2011, 95, 1001–1004.

44. M. Johnson, S. V. Baryshev, E. Thimsen, M. Manno, X. Zhang, I. V. Veryovkin, C. Leighton, and E. S. Aydil, Energy Environ. Sci., 2014, 10.1039/c3ee44130j.

45. K. Granath, M. Bodegård, and L. Stolt, Sol. Energ. Mat. Sol. C., 2000, 60, 279–293.

46. D. Rudmann, G. Bilger, M. Kaelin, F.-J. Haug, H. Zogg, and A. N. Tiwari, Thin Solid Films, 2003, 431-432, 37–40.

47. W. M. Hlaing Oo, J. L. Johnson, A. Bhatia, E. A. Lund, M. M. Nowell, and M. A. Scarpulla, J. Electron. Mater., 2011, 40, 2214–2221.

48. L. Kronik, D. Cahen, and H. W. Schock, Adv. Mater., 1998, 10, 31–36.

49. D. W. Niles, K. Ramanathan, F. Hasoon, R. Noufi, B. J. Tielsch, and J. E. Fulghum, J. Vac. Sci. Technol. A, 1997, 15, 3044–3049.

50. A. Rockett, Thin Solid Films, 2000, 362, 330–337.

51. D. Rudmann, Ph.D. Thesis, Swiss Federal Institute of Technology (ETH) Zürich, 2004.

Chapter 5

1. H. Katagiri, K. Saitoh, T. Washio, H. Shinohara, T. Kurumadani, and S. Miyajima, Sol. Energ. Mat. Sol. Cells, 2001, 65, 141–148.

2. W. Wang, M. T. Winkler, O. Gunawan, T. Gokmen, T. K. Todorov, Y. Zhu, and D. B. Mitzi, Adv. Energy Mater., 2013, 10.1002/aenm.201301465.

3. I. Repins, C. Beall, N. Vora, C. DeHart, D. Kuciauskas, P. Dippo, B. To, J. Mann, W.-C. Hsu, A. Goodrich, and R. Noufi, Sol. Energ. Mat. Sol. Cells, 2012, 101, 154–159.

4. J. B. Li, V. Chawla, and B. M. Clemens, Adv. Mater., 2012, 24, 720–723.

5. Z. Su, K. Sun, Z. Han, H. Cui, F. Liu, Y. Lai, J. Li, X. Hao, Y. Liu, and M. A. Green, J. Mater. Chem. A, 2014, 2, 500–509.

6. J.-O. Jeon, K. D. Lee, L. Seul Oh, S.-W. Seo, D.-K. Lee, H. Kim, J.-H. Jeong, M. J. Ko, B. Kim, H. J. Son, and J. Y. Kim, ChemSusChem, 2014, 7, 1073–1077.

7. Y. Cao, M. S. Denny, J. V Caspar, W. E. Farneth, Q. Guo, A. S. Ionkin, L. K. Johnson, M. Lu, I. Malajovich, D. Radu, H. D. Rosenfeld, K. R. Choudhury, and W. Wu, J. Am. Chem. Soc., 2012, 134, 15644–15647.

8. C. K. Miskin, W. C. Yang, C. J. Hages, N. J. Carter, C. S. Joglekar, E. A. Stach, and R. Agrawal, Prog. Photovoltaics Res. Appl., 2014, 10.1002/pip.2472.

9. K. Woo, Y. Kim, W. Yang, K. Kim, I. Kim, Y. Oh, J. Y. Kim, and J. Moon, Sci. Rep., 2013, 3, 3069.

10. H. Xin, J. K. Katahara, I. L. Braly, and H. W. Hillhouse, Adv. Energy Mater., 2014, 10.1002/aenm.201301823.

11. T. Schnabel, M. Löw, and E. Ahlswede, Sol. Energ. Mat. Sol. Cells, 2013, 117, 324–328.

12. B. D. Chernomordik, A. E. Béland, D. D. Deng, L. F. Francis, and E. S. Aydil, Chem. Mater., 2014, 10.1021/cm500791a.

13. B. Shin, O. Gunawan, Y. Zhu, N. A. Bojarczuk, S. J. Chey, and S. Guha, Prog. Photovoltaics Res. Appl., 2013, 21, 72–76.

14. A. Redinger, M. Mousel, M. H. Wolter, N. Valle, and S. Siebentritt, Thin Solid Films, 2013, 535, 291–295.

15. S. Chen, A. Walsh, X.-G. Gong, and S.-H. Wei, Adv. Mater., 2013, 25, 1522–1539.

16. R. Mainz, B. C. Walker, S. S. Schmidt, O. Zander, A. Weber, H. Rodriguez-Alvarez, J. Just, M. Klaus, R. Agrawal, and T. Unold, Phys. Chem. Chem. Phys., 2013, 15, 18281.

17. G. Wang, W. Zhao, Y. Cui, Q. Tian, S. Gao, L. Huang, and D. Pan, ACS Appl. Mater. Interfaces, 2013, 5, 10042–10047.

18. G. M. Ilari, C. M. Fella, C. Ziegler, A. R. Uhl, Y. E. Romanyuk, and A. N. Tiwari, Sol. Energ. Mat. Sol. Cells, 2012, 104, 125–130.

19. W. Wang, S.-Y. Han, S.-J. Sung, D.-H. Kim, and C.-H. Chang, Phys. Chem. Chem. Phys., 2012, 14, 11154–11159.

20. S. J. Ahn, C. W. Kim, J. H. Yun, J. Gwak, S. Jeong, B.-H. Ryu, and K. H. Yoon, J. Phys. Chem. C, 2010, 114, 8108–8113.

21. Q. Guo, G. M. Ford, W.-C. Yang, B. C. Walker, E. A. Stach, H. W. Hillhouse, and R. Agrawal, J. Am. Chem. Soc., 2010, 132, 17384–17386.

22. H. Rau, T. R. N. Kutty, and J. R. F. Guedes De Carvalho, J. Chem. Thermodyn., 1973, 5, 833–844.

23. H. Rau, J. Chem. Thermodyn., 1974, 6, 525–535.

24. C. V. Thompson, J. Appl. Phys., 1985, 58, 763–772.

25. J. van Embden, A. S. R. Chesman, E. Della Gaspera, N. W. Duffy, S. E. Watkins, and J. J. Jasieniak, 2014, 10.1021/ja501218u.

26. A. Khare, B. Himmetoglu, M. Johnson, D. J. Norris, M. Cococcioni, and E. S. Aydil, J. Appl. Phys., 2012, 111, 083707.

27. K. Wang, O. Gunawan, T. Todorov, B. Shin, S. J. Chey, N. A. Bojarczuk, D. Mitzi, and S. Guha, Appl. Phys. Lett., 2010, 97, 143508.

28. M. Grossberg, J. Krustok, J. Raudoja, and T. Raadik, Appl. Phys. Lett., 2012, 101, 102102.

29. M. Grossberg, J. Krustok, J. Raudoja, K. Timmo, M. Altosaar, and T. Raadik, Thin Solid Films, 2010, 519, 7403–7406.

30. A. Fairbrother, X. Fontané, V. Izquierdo-Roca, M. Placidi, D. Sylla, M. Espindola-Rodriguez, S. Marino-Lopez, F. A. Pulgarin, O. Vigil-Galán, A. Perez-Rodriguez, and E. Saucedo, Prog. Photovoltaics Res. Appl., 2014, 22, 479–487.

31. J. He, L. Sun, S. Chen, Y. Chen, P. Yang, and J. Chu, J. Alloys Compd., 2012, 511, 129–132.

32. A. Khare, B. Himmetoglu, M. Cococcioni, and E. S. Aydil, J. Appl. Phys., 2012, 111, 123704.

33. A.-J. Cheng, M. Manno, A. Khare, C. Leighton, S. A. Campbell, and E. S. Aydil, J. Vac. Sci. Technol. A, 2011, 29, 051203.

34. M. Ganchev, J. Iljina, L. Kaupmees, T. Raadik, O. Volobujeva, A. Mere, M. Altosaar, J. Raudoja, and E. Mellikov, Thin Solid Films, 2011, 519, 7394–7398.

35. Y. C. Cheng, C. Q. Jin, F. Gao, X. L. Wu, W. Zhong, S. H. Li, and P. K. Chu, J. Appl. Phys., 2009, 106, 123505.

36. Z. Levi, I. Bineva, and D. Nesheva, Acta Phys. Pol. A, 2009, 116, 75–77.

37. P. A. Fernandes, P. M. P. Salomé, and A. F. da Cunha, J. Alloys Compd., 2011, 509, 7600–7606.

38. C. Wang, Chem. Phys. Lett., 2002, 357, 371–375.

39. H. R. Chandrasekhar and R. G. Humphreys, Phys. Rev. B, 1977, 15, 2177–2183.

40. A. J. Smith, P. E. Meek, and L. W. Y, J. Phys. C Solid State Phys., 1977, 10, 1321–1333.

41. V. Izquierdo-Roca, A. Pérez-Rodríguez, A. Romano-Rodríguez, J. R. Morante, J. Álvarez-García, L. Calvo-Barrio, V. Bermudez, P. P. Grand, O. Ramdani, L. Parissi, and O. Kerrec, J. Appl. Phys., 2007, 101, 103517.

42. C. Xue, D. Papadimitriou, Y. S. Raptis, W. Richter, N. Esser, S. Siebentritt, and M. C. Lux-Steiner, J. Appl. Phys., 2004, 96, 1963.

43. P. A. Fernandes, P. M. P. Salomé, and A. F. da Cunha, J. Phys. D. Appl. Phys., 2010, 43, 215403.

44. C. G. Munce, G. K. Parker, S. a. Holt, and G. a. Hope, Colloids Surfaces A, 2007, 295, 152–158.

45. T. P. Mernagh and A. G. Trudu, Chem. Geol., 1993, 103, 113–127.

46. P. a. Fernandes, M. G. Sousa, P. M. P. Salomé, J. P. Leitão, and A. F. da Cunha, CrystEngComm, 2013, 15, 10278.

47. C. Wang and A. Manthiram, ACS Sustain. Chem. Eng., 2014, 2, 561–568.

48. I. Klugius, R. Miller, A. Quintilla, T. M. Friedlmeier, D. Blázquez-Sánchez, E. Ahlswede, and M. Powalla, Phys. status solidi - Rapid Res. Lett., 2012, 6, 297–299.

49. A. Niemegeers, M. Burgelman, and A. De Vos, Appl. Phys. Lett., 1995, 67, 843–845.

50. D. J. G. Ives, R. W. Pittman, and W. Wardlaw, J. Chem. Soc., 1947, 1080–1083.

51. Y. Wang, D. C. Alsmeyer, and R. L. McCreery, Chem. Mater., 1990, 2, 557–563.

52. P. K. Chu and L. Li, Mater. Chem. Phys., 2006, 96, 253–277.

53. Z. Iqbal, S. T. Correale, F. Reidinger, R. H. Baughman, and Y. Okamoto, J. Chem. Phys., 1988, 88, 4492–4497.

54. M. Johnson, S. V Baryshev, E. Thimsen, M. Manno, X. Zhang, I. V Veryovkin, C. Leighton, and E. S. Aydil, Energy Environ. Sci., 10.1039/c3ee44130j.

55. P. C. Hiemenz and R. Rajagopalan, in Principles of Colloid and Surface Chemistry, eds. P. C. Hiemenz and R. Rajagopalan, Taylor & Francis, Boca Raton, Florida, 3rd edn., 1997, pp. 437–439.

56. Z. Gemici, P. I. Schwachulla, E. H. Williamson, M. F. Rubner, and R. E. Cohen, Nano Lett., 2009, 9, 1064–1070.

57. B. S. Tosun, B. D. Chernomordik, A. Gunawan, B. Williams, K. A. Mkhoyan, L. F. Francis, and E. S. Aydil, Chem. Commun., 2013, 49, 3549–3551.

58. A. C. Ferrari and J. Robertson, Phys. Rev. B, 2000, 61, 14095–14107.

59. R. M. German, Liquid Phase Sintering, Plenum Press, 1985.

60. R. M. German, P. Suri, and S. J. Park, J. Mater. Sci., 2009, 44, 1–39.

61. W. D. Kingery, J. Appl. Phys., 1959, 30, 301–306.

APPENDIX A

Supplementary and Preliminary Data

A.1 Grain Growth Onset Temperature

Figure A.1a shows XRD patterns from kesterite CZTS nanocrystals as a function of temperature. The initial CZTS nanocrystals were 5 nm in diameter, as calculated from the FWHM of the (112) XRD peak and confirmed by TEM. The nanocrytals were nominally stoichiometric as determined by EDS. After synthesis and washing, the nanocrystals were stirred in pyridine overnight and then dried over N_2. The dry nanocrystal powder was poured into a quartz capillary (1 mm OD, 10 μm wall thickness, Hampton Research) and glass wool was used to keep the powder inside the capillary. The XRD measurements were performed on the X7B beamline of the National Synchrotron Light Source (NSLS) at the Brookhaven National Laboratory. The measurements were performed in a transmission geometry and a Perkin-Elmer Amorphous Silicon Detector was used to collect the two-dimensional diffraction data, which was processed using Fit2D to obstain XRD patterns. The X-ray wavelength was 0.3196 Å and the sample to the 2D area detector distance was 376.3 mm. (The patterns shown in Figure A1a were plotted vs. 2θ after conversion to Cu Kα radiation). A thermocouple was inserted into the quartz capillary and position within 5 mm of the CZTS powder. Then a heating wire was wrapped around the outside of the capillary region containing the CZTS powder and thermocouple (~10 revolutions) such that the coil length was ~2 cm. The CZTS powder was heated to 700 ^{o}C at 10 ^{o}C/min. Helium gas was flown through the capillary during measurements. The initial XRD peaks are broad due to the small crystallite size (5 nm), but they narrow and increase in intensity as the nanocrystals are heated. Figure A1.b shows the peak intensity of the (112) XRD peak (28.4^{o}) as a function of temperature. The sharp increase in intensity at 330 ^{o}C is attributed to the onset of crystal growth and the concomitant increase in the grain size. This onset at ~330 ^{o}C (603 K) is

approximately 0.5 T_m where T_m is the melting point of CZTS (1263 K).[1] Grain growth and sintering is expected to occur in the range $0.5 < T/T_M < 0.95$, where T_M is the melting point temperature.[2] The intensity and the width saturates due to the instrumental broadening limit.

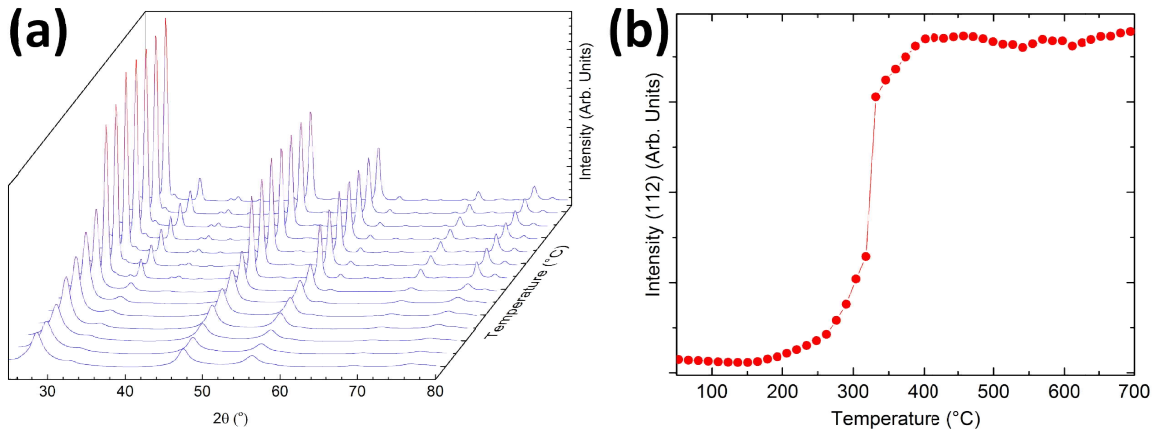

Figure A.1 (a) XRD from CZTS nanocrystals as a function of temperature and (b) the (112) peak intensity (at 28.4°) as a function of temperature.

A.2 Wurtzite CZTS Nanocrystal Annealing

During the annealing experiments detailed in section A.1, the kesterite CZTS nanocrystals also began to decompose at the grain growth onset temperature. Specifically, the XRD from SnS was detected simultaneously with the increase in the kesterite peak intensities. Examination of the nanocrystals after annealing with scanning electron microscopy revealed that the decomposition occurred only on the surfaces of the dried nanocrystal powder clumps, which form during drying. Sintered and 100-500 nm nm crystals of kesterite CZTS were found on the inside regions of these clumps after breaking them apart. The decomposition and presence of SnS on the surface regions of nanocrystal clumps is consistent with thermodynamic calculations by Scragg *et al.* who showed that CZTS will decompose into SnS if annealed in the absence of sulfur vapor and Sn. SnS has high vapor pressure and vaporizes, leaving the films Sn and S deficient. In our annealing experiments, SnS from the exposed CZTS surfaces is continually removed by flowing He. Figure A.2b shows an XRD pattern (red) of kesterite CZTS nanocrystals at 350 °C (at the beginning stages of grain growth). XRD peaks from SnS are clearly visible in addition to the kesterite CZTS peaks.

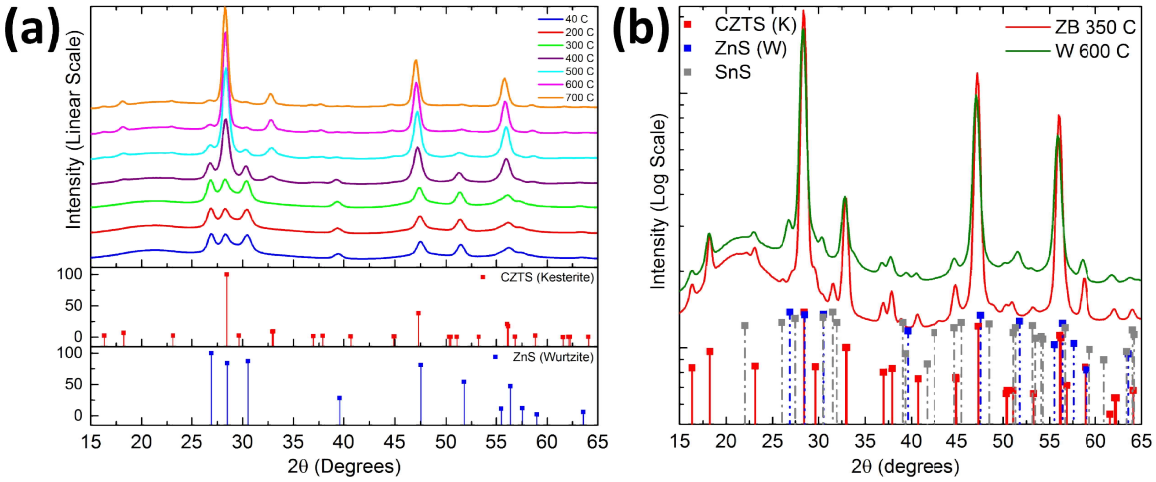

Figure A.2 (a) XRD patterns of wurtzite CZTS nanocrystals as a function of temperature. The patterns are in the top panel are linearly stacked for clarity. The different colors represent different patterns collected at different temperatures (between 40 °C and 700 °C). The bottom two panels show standard reference XRD patterns for kesterite CZTS (ICDD-ref 04-005-0388) and wurtzite ZnS (ICDD-ref 00-036-1450). (b) XRD patterns of wurtzite CZTS nanocrystals at 600 °C (green and labeled "W 600 C") and of kesterite CZTS nanocrystals at 350 °C (red and labeled "ZB 350 C," where ZB refers to zinc blende). The red, blue, and gray vertical lines represent the standard reference XRD patterns for kesterite CZTS, wurtzite ZnS, and orthorhombic SnS (ICDD-ref 00-039-0354), respectively.

The measurements described in section A.1 were also conducted with 5 nm wurtzite CZTS nanocrystals. Wurtzite nanocrystals were synthesized by Ankur Khare by similar methods as discussed in Khare et al.,[3] except that dodecanethiol was used instead of oleic acid. Figure A.2a shows XRD from wurtzite CZTS nanocrystals as they were heated to 700 °C at 10 °C/min. The nanocrystals were confirmed to be wurtzite CZTS using Raman spectroscopy. As the temperature is increased above 300 °C and near the onset temperature for grain growth (i.e., between 300 and 400 °C), the patterns become a linear combination of diffraction from wurtzite and kesterite phase. The wurtzite phase of CZTS is thermodynamically unstable with respect to transformation to the kesterite phase. Thus, the transformation from the wrtzite to the kesterite phase is expected. That this transformation takes place at around the same temperature is also not surprising since the atoms in the lattice become sufficiently mobile at this temperature for solid state transformations including phase change and grain growth to take place. Indeed, with further increase in temperature, the kesterite peaks gain intensity while the peaks specific to wurtzite lose intensity. However, very weak wurzite peaks remain even at 700 °C. The diffractions peaks at 37.0° [(202)], 37.9° [(211)], and 44.9° [(105) and (213)], which

indicate the definite presence of kesterite CZTS,[4] are resolved in the patterns at T > 350 ^{o}C but the peaks corresponding to kesterite CZTS may also include zinc-blend ZnS and monoclinic Cu_2SnS_3.[4] Raman spectroscopy would provide information regarding the presence of ZnS or Cu_2SnS_3.

In contrast to kesterite CZTS nanocrystals, which decompose into SnS upon annealing, wurtzite nanocrystals do not decompose into SnS after annealing: SnS diffractions were not detected in the XRD patterns from annealed wurtzite nanocrystals. For example, Figure A.2b compares an XRD pattern from annealed wurtzite CZTS nanocrystals collected at 600 ^{o}C (green) to that from annealed kesterite CZTS nanocrystals at 350 ^{o}C (red). While the kesterite nanocrystals decompose into SnS between 300 ^{o}C and 400 ^{o}C, SnS diffractions are not detected in annealed wurtzite nanocrystals even after they are heated to 600 ^{o}C. In fact, within the detection limits of XRD, no Sn_xS_y or Cu_xS phases were detected from annealed wurtzite nanocrystals. This suggests that wurtzite CZTS does not decompose into SnS even when heated to 600 ^{o}C in inert atmosphere.[5,6] This is particularly peculiar because by 600 ^{o}C nearly all wurtzite nanocrystals have been converted to Kesterite grains: it is peculiar because kesterite nanocrystals do decompose while annealed kesterite grains appear stable within the detection limits of XRD. This observation suggests that the decomposition to SnS is more severe and readily proceeds in films with large surface area and on the surfaces of the nanocrystals. When the kesterite grains are large, decomposition may occur on the surface still but both the rate and the amount will be reduced to levels not easily detectable by XRD. This explanation is supported by recent experiments by Mainz et al. who have recently showed that annealing wurtzite nanorods in inert atmosphere rapidly forms thin films with large kesterite grains. In their experiments, fast heating rate allowed the wurtzite-to-kesterite phase transformation and grain growth to occur together and rapidly on the same time scale.[7] They too did not observe decomposition. This suggests that decomposition into SnS is exacerbated for small grains but is significantly retarded when the grains are large. This is consistent with the fact that decomposition to SnS occurs at or near surfaces. In situations where the surface area is small, decomposition of CZTS to SnS is significantly reduced. The driving force for wurtzite to kesterite transition helps grain growth and rapid grain growth reduces decomposition. That is, the

grains grow before CZTS has a chance to decompose. This also suggests that in experiments where SnS is observed, the decomposition occurs when the CZTS grains were still small. The ability to transform CZTS nanocrystal films to large grained CZTS films without formation of SnS in an inert atmosphere, without sulfur, would simplify annealing and may offer significant cost reduction in manufacturing.

A.3 Annealing Without Sulfur or Selenium

Figure A.3 compares SEM images of a film annealed at 700 ^{o}C for 1 hour on quartz without sulfur loading in the sealed ampule to those annealed at the same temperature and time but with 50 and 500 Torr of sulfur. The latter two films were also shown and discussed in Chapter 4. Figure A.4 shows XRD and Raman spectra from the film annealed without sulfur. Although sulfur was not added to the ampule, the film retained the kesterite CZTS phase and no decomposition products such as SnS were detected by XRD, Raman, or EDS. Sulfur and tin loss is expected when CZTS films are annealed without sulfur present vapor over the film. However, Scragg et al. suggested that even only 1.7×10^{-4} Torr of sulfur is enough to eliminate sulfur loss.[5] Calculations in Appendix B.5 show that only between 0.0014% and 0.015% of the S-atoms in the CZTS nanocrystal films have to be removed to establish this minimum sulfur vapor pressure required to stabilize CZTS because the annealing ampule is a closed system. Thus, it is not surprising that the CZTS film remains stable during annealing even without sulfur loading into the ampoule. Interestingly, normal crystal sizes in the film annealed without sulfur are smaller than the normal crystals in the film annealed at 500 Torr S (a-c) but larger than in the normal crystals annealed at 50 Torr S (d-f). Although the amount of sulfur loss from the CZTS film is small, the associated rearrangement/perturbation of the sulfur lattice cage may lower the activation energy associated with grain growth or sintering by mechanisms such as evaporation/condensation.[2]

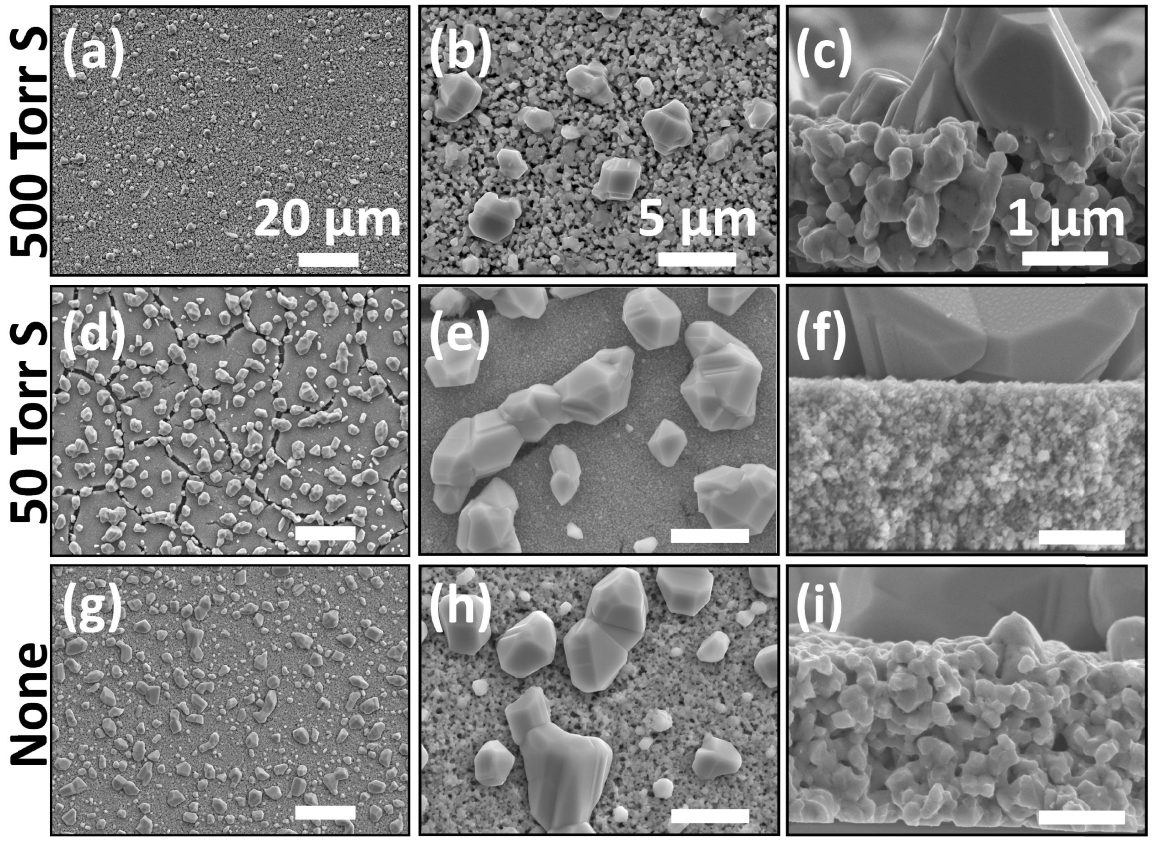

Figure A.3 SEM images of films annealed on quartz at 700 °C for 1 hour with (a-c) 500 Torr of sulfur, (d-f) 50 Torr of sulfur, and (g-i) without sulfur in the ampule.

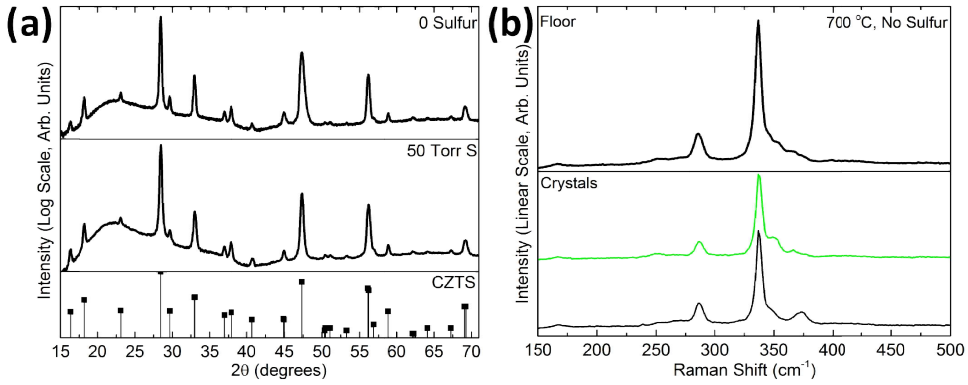

Figure A.4 (a) XRD from CZTS nanocrystal coatings on quartz after annealing at 700 °C on for 1 hour with 50 Torr of sulfur and without sulfur in the ampoule. (b) Raman spectra from the film that was annealed without sulfur. The top panel, labeled "Floor," shows the Raman spectrum from the bottom floor layer of the film which contains the nanocrystalline CZTS grains. The bottom panel shows two Raman spectra (green and black) from the microcrystalline CZTS abnormal grains on top of the floor layer. The latter two spectra were collected from different areas of the CZTS microcrystals and show a convolution of Raman scattering from combinations of several crystal facets. These spectra are consistent with scattering from CZTS. Please see Figure 4.15 and the discussion in chapter section 4.3.2 for more information regarding Raman scattering from different facets of the microcrystalline CZTS grains.

A.4 Crystal Growth Enhancement with Vapor Phase Delivery of Sodium

As discussed in chapter Section 4.3.5, the introduction of alkali metals such as Na, by using an SLG substrate, accelerates crystal growth in CZTS nanocrystal films during annealing. Recently, we showed that alkali metals may also be delivered to the film via the vapor phase to enhance crystal growth during sulfidation of a Cu-Zn-Sn alloy at 600 ^{o}C to form CZTS.[8] (This was achieved by depositing a desired amount of Na onto the ampule walls from known concentrations and volumes of aqueous NaOH. After the water evaporates, the substrate with the CZTS nanocrystal coating and sulfur are loaded into the tube, which is then evacuated and flame sealed as described in Section 4.2.3.) Here, we show that CZTS nanocrystal coatings deposited on quartz and annealed with NaOH in the tube exhibit significantly accelerated crystal growth when compared to films annealed on quartz but without NaOH in the tube.

The effect of introducing Na to the CZTS nanocrystal film via the vapor phase during annealing is clearly shown in Figure A.5. For comparison, SEM images A.5a and A.5d show a CZTS nanocrystal coating, deposited on Mo-coated quartz, annealed at 600 ^{o}C in 50 Torr of sulfur for 1 hour without NaOH in the ampule. This annealed coating contains normal crystals that are ~45 nm. Images A.5b, A.5c, and A.5f show a CZTS film annealed at identical conditions except that a coating containing $3 \cdot 10^{-6}$ mol of NaOH was deposited on one end of the ampule. The latter annealed CZTS film is composed of a dense layer of ~1 μm to ~5 μm CZTS grains. Multiple NaOH quantities were tested and it was found that grain size increases with the amount of NaOH (not shown) until the amount of NaOH is so large that Na containing phases begin to appear.

The grain sizes are larger when bare quartz is used as the substrate instead of Mo-coated quartz, under otherwise identical conditions. This suggests that, although the Na is supplied from the vapor, the molybdenum layer may act as a sink for Na. Experiments were also conducted with molybdenum foil as the substrate and several different combinations of sulfur pressure and NaOH loading were tested. Average crystal sizes greater than ~300 nm were not obtained even when the sulfur pressure was increased to

500 Torr and $3 \cdot 10^{-6}$ mol of NaOH were introduced, suggesting that the Mo foil behaves as a sink for both sulfur (due to formation of MoS_2) and Na.

A more nuanced point is that there exists a gradient of vapor-phase Na-containing species inside the ampule. The grain sizes in A.5b are smaller than in A.5c because the region of the film shown in A.5b was farther away from the NaOH coating at one end of the ampule than the region shown in Figure A.5c. (The NaOH coating extends approximately 1 cm from the end of the ampule and the film is approximately 2 cm long.) Placing the film on the opposite end of the ampule from the NaOH coating further reduces the crystal sizes. An outline of drying front of the NaOH coating on the ampule remains visible to the naked eye after annealing. Peculiarly, this is even true for annealing times as long as 8 hours. This suggests that the rate of Na entering the vapor phase, in whichever form, is extremely slow and the quantity of Na interacting with the CZTS film is not equivalent to the amount contained within the initial NaOH coating.

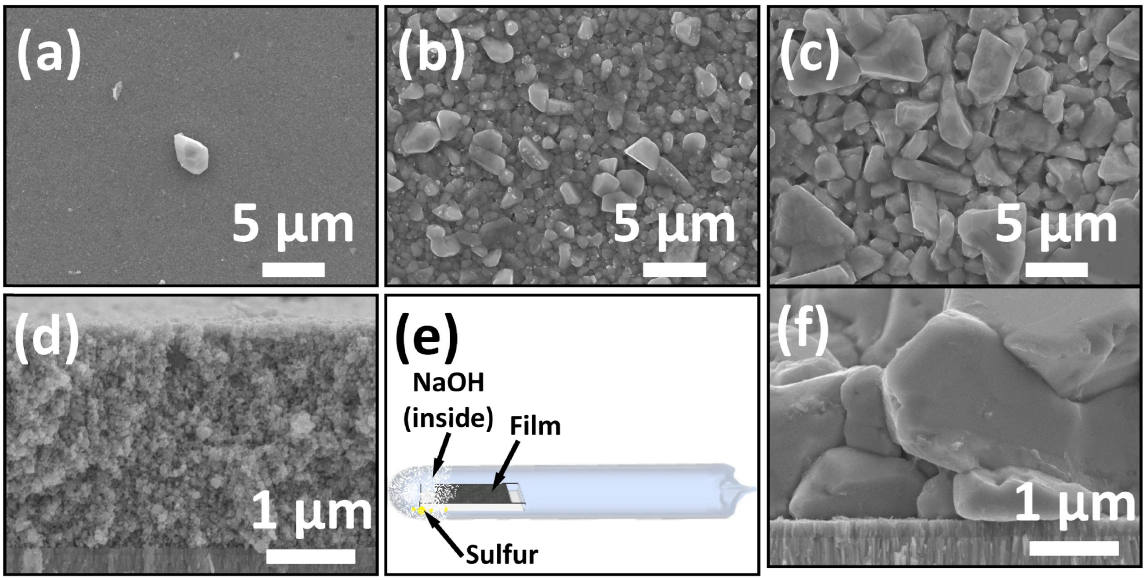

Figure A.5 (a, d) SEM images of a CZTS nanocrystal coating on Mo-coated quartz after annealing at 600 °C with 50 Torr S for 1 hour. (b, c, f) SEM images of a CZTS nanocrystal coating on Mo-coated quartz after annealing at 600 °C with 50 Torr S for 1 hour and $3 \cdot 10^{-6}$ mol NaOH loaded on one end of the annealing ampule. As shown in (e), the sample was placed on the same side of the ampule as the NaOH coating. Image (b) is from the part of the film farthest from NaOH and image (c) is on the part of the film closest to (or directly under) the NaOH coating.

A.5 References

1. I. D. Olekseyuk, I. V. Dudchak, and L. V. Piskach, *J. Alloys Compd.*, 2004, **368**, 135–143.

2. R. M. German, *Crit. Rev. Solid State Mater. Sci.*, 2010, **35**, 263–305.

3. A. Khare, A. W. Wills, L. M. Ammerman, D. J. Norris, and E. S. Aydil, *Chem. Commun.*, 2011, **47**, 11721–11723.

4. A.-J. Cheng, M. Manno, A. Khare, C. Leighton, S. A. Campbell, and E. S. Aydil, *J. Vac. Sci. Technol. A*, 2011, **29**, 051203.

5. J. J. Scragg, T. Ericson, T. Kubart, M. Edoff, and C. Platzer-Björkman, *Chem. Mater.*, 2011, **23**, 4625–4633.

6. A. Weber, R. Mainz, and H. W. Schock, *J. Appl. Phys.*, 2010, **107**, 013516.

7. R. Mainz, A. Singh, S. Levcenko, M. Klaus, C. Genzel, K. M. Ryan, and T. Unold, *Nat. Commun.*, 2014, **5**, 1–10.

8. M. Johnson, S. V Baryshev, E. Thimsen, M. Manno, X. Zhang, I. V Veryovkin, C. Leighton, and E. S. Aydil, *Energy Environ. Sci.*, 10.1039/c3ee44130j.

APPENDIX B

Calculations

B.1 Sulfur and Selenium Vapor Pressure

This section is regarding the making of Figures 4.3 and 5.1. The black curves in Figure 5.1 represent the saturated vapor pressure of sulfur and selenium as a function of temperature. The saturated vapor pressure curve for sulfur was calculated using the Wagner Equation (B.1):

(1) $$\ln\left(\frac{p}{p_c}\right) = [A\left(1-\frac{T}{T_c}\right) + B\left(1-\frac{T}{T_c}\right)^{\frac{3}{2}} + C\left(1-\frac{T}{T_c}\right)^{3} + D\left(1-\frac{T}{T_c}\right)^{6}](\frac{T_c}{T})$$

where,

Table B.1 Critical pressure, critical temperature, and Wagner coefficients for Equation B.1[1]

Variable	Value
p_c	18208 kPa
T_c	1313 K
A	-7.245867
B	0.187391
C	5.271390
D	-12.128352

The Wagner values for the sulfur vapor pressure are from Peng et al.[1] The saturated vapor pressure of selenium was calculated using Equation (B.2):[2]

(2) $$\ln(p) = -\frac{5\ 0\ 4\ 3}{T} + 5.265$$

where the unit of p is atm and T is Kelvin.

The pressure inside the ampule is the saturated vapor pressure until the corresponding molar quantity of S or Se is greater than the moles of solid S or Se charged in the ampule. Past this point, the pressure in the ampule is estimated using the ideal gas

law equation. This equation requires the correct molar quantity, n, of gaseous species. This value was estimated using published vapor pressure speciation data for sulfur[3] and selenium,[4] shown in Figures B.1 and B.2, respectively. See below for more details:

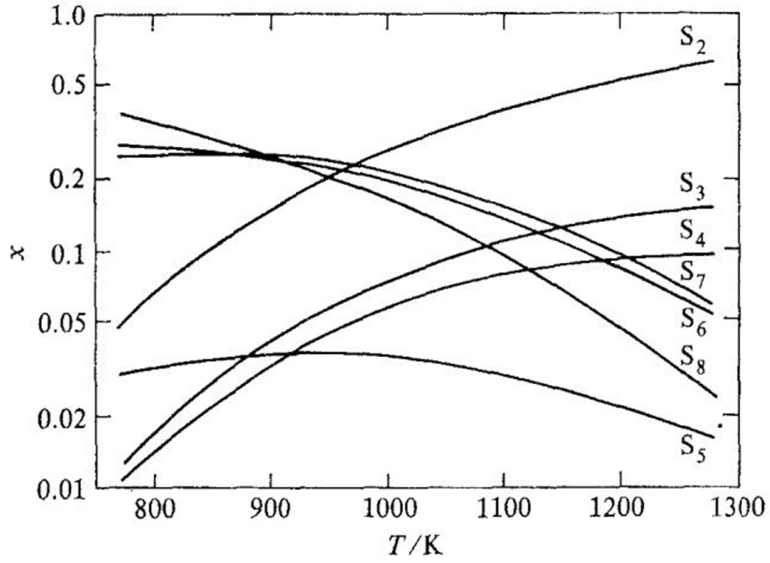

Figure B.1 Sulfur vapor pressure speciation as a function of temperature, showing the mole fraction x of different molecular species.[3]

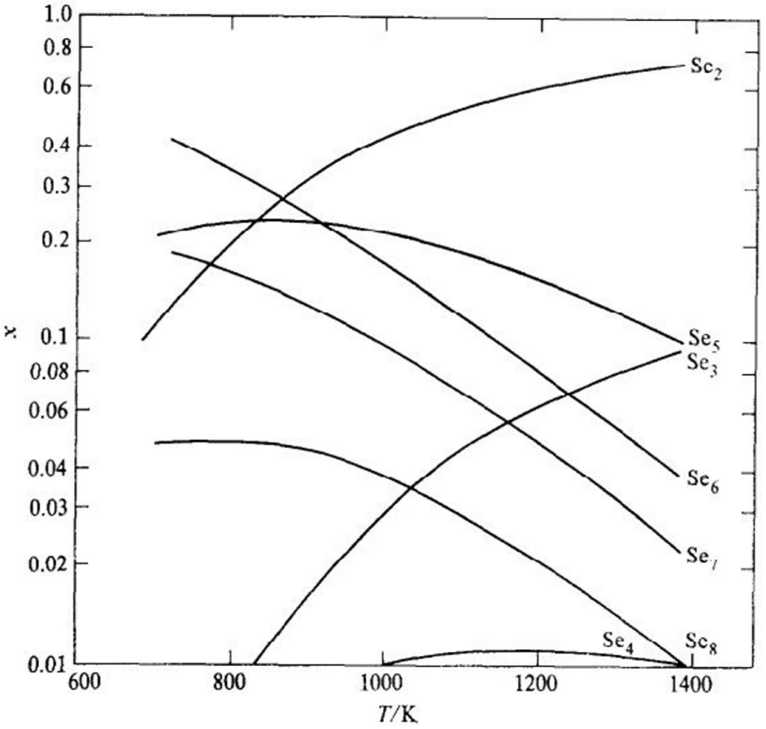

Figure B.2 Selenium vapor pressure speciation as a function of temperature, showing the mole fraction x of different molecular species.[4]

The vapor pressure speciation at 200 °C, 300 °C, and 400 °C were extrapolated. The quantity v was calculated such that $v = \sum_{i=2}^{8} x_i \cdot i$, where i is the number of S or Se atoms in the corresponding polytype (*i.e.*, i=8 in Se_8). Table B.2 shows the value v for S and Se at different temperatures. The quantity n, the number of moles of gaseous species in the ampule, was then calculated by converting the mass of S or Se charged into the ampule into moles of the species S_v or Se_v, respectively. This was then used to calculate the S or Se pressure in the ampule as a function of temperature using the ideal gas law equation.

Table B.2 The values v, corresponding to the equation $v = \sum_{i=2}^{8} x_i \cdot i$, such that the average speciation may be represented as a single molecular species.

Temperature (°C)	S_*v*	Se_*v*
200	7.45	6.19
300	7.31	6.16
400	7.06	5.66
455		5.55
500	6.86	5.42
550	6.41	
600	6.05	4.86
700	5.16	4.22
800	4.57	3.83

B.2 Moles of Carbon in the Film Relative to Sulfur in Vapor

Table B.3 The assumptions and constants and the progression of the calculation of moles of carbon atoms in the CZTS nanocrystal film. The nanocrystals were assumed to be 25 nm in diameter and a ligand surface coverage was assumed to be $9 \cdot 10^{13}$ cm^{-2}, based on calculations in Tosun et al.[5] The calculation shows, with 1 mg S, there is almost two orders of magnitude more S in the vapor than necessary for all carbon in the nanocrystal film to become CS_2.

Film Width (mm)	8
Film Length (mm)	20
Film Thickness (microns)	2
Packing Density (decimal)	0.6
Particle Size (nm)	30
Ligand Shell Size (nm)	1
Carbon Count in Ligand (#)	18
Density of Ligands (# per cm^2)	9.00E+13
Mass of Sulfur (mg)	1
Ampule volume (cm^3)	7.85

Film Volume Total (mm^3)	Solid Volume (including ligand) (mm^3)	# Particles in Film (with ligand)	Total Particle Surface Area (cm^2)	# moles Ligands	# moles C-atoms	# moles S-atoms
0.32	0.192	1.12E+13	3.16E+02	4.73E-08	8.51E-07	3.12E-05

B.3 Ratios of Sulfur in Film to Selenium in Vapor

Table B.4 shows the results of three different ratios comparing the amount of sulfur in the CZTS nanocrystal film to the amount of selenium in the vapor at 700 ^{o}C for four different selenium charges in the ampule. The moles of S in the CZTS nanocrystal film is shown in section B.2 and Table B.3. The ratio "Moles Se / (Moles S + Moles Se)" is the fraction of all Se_1 in the vapor relative to S_1 in the film. The ratio "Torr Se_4.22 / (Torr S_1 + Torr Se_4.22)" is the fraction of speciated Se (i.e., $Se_{4.22}$ where v=4.22) relative to the partial pressure of S_1 if all S in the film became S_1 vapor. The ratio "Moles Se_4.22 / (Moles S_5.157 + Moles Se_4.22)" is the fraction of speciated Se (*i.e.*, $Se_{4.22}$) relative to the moles of speciated S if all S in the film became vapor containing $S_{5.16}$. The purpose of calculating these ratios was to compare the elemental compositions measured by EDS in selenized films to expectations based on ratios of S and Se present. Due to having a closed system, S replaced/removed from the film is assumed to become vapor in the ampule.

Table B.4 Ratios comparing the amount of sulfur in the CZTS nanocrystal film to the amount of selenium in the vapor at 700 ^{o}C for four different selenium charges in the ampule.

Temperature (C)	Ideal Pressure if All S From Film Evaporated into S_1 (Torr)			
700	24.4			
Se Loading in Ampule	**If 0.5 mg Se**	**if 1.96 mg Se**	**if 10.8 mg Se**	**if 19.6 mg Se**
Moles Se / (Moles S + Moles Se)	0.67	0.89	0.98	0.99
Torr Se_4.22 / (Torr S_1 + Torr Se_4.22)	0.33	0.65	0.91	0.95
Moles Se_4.22 / (Moles S_5.157 + Moles Se_4.22)	0.71	0.91	0.98	0.99

B.4 Calculation of Amorphous Carbon Coating Thickness

Table B.5 Assumptions, constants, and progression of calculation to determine the thickness of amorphous carbon to have equivalent moles of carbon in the coating as is normally in a film of nanocrystals with ligands. An amorphous carbon density of 2 g/cm3 was assumed. The nanocrystal film is typically 8 mm by 20 mm, whereas the amorphous carbon coating was deposited over a substrate area of 8 mm by 25 mm.

Film Width (mm)	8
Film Length (mm)	20
Film Thickness (microns)	2
Packing Density (decimal)	0.6
Particle Size (nm)	30
Ligand Shell Size (nm)	1
Carbon Count in Ligand (#)	18
Density of Ligands (# per cm^2)	9.00E+13
Mass of Sulfur (mg)	1
Ampule volume (cm^3)	7.85

Film Volume Total (mm^3)	Solid Volume (including ligand) (mm^3)	# Particles in Film (with ligand)	Total Particle Surface Area (cm^2)	# moles Ligands	# moles C-atoms	# moles S-atoms
0.32	0.192	1.12E+13	3.16E+02	4.73E-08	8.51E-07	3.12E-05

Carbon Coating Thickness in nm on Quartz That is 0.8 cm x 2.5 cm
25.54

B.5 Calculation of Sulfur Removed from Film to Establish Required Sulfur Pressure for CZTS Stability

Scragg et al. showed that it is thermodynamically favorable for CZTS to lose sulfur if films are processed in the absence of a sulfur partial pressure. The CZTS film will then undergo decomposition as the loss of sulfur results in reduction of Sn(IV) to Sn(II), leading to the evolution of SnS. It was suggested that an S_2 pressure of at least $1.7 \cdot 10^{-4}$ Torr is necessary to prevent sulfur loss.[6] Only the S_2 polytype of sulfur was considered. In Table B.6, we calculate the fraction of sulfur that is lost from the CZTS nanocrystal film to establish the stability condition of $1.7 \cdot 10^{-4}$ Torr of S_2. This is done in two ways. In one case, it assumed that only S_2 vapor will exist in the ampule at $1.7 \cdot 10^{-4}$ Torr. This S_2 pressure is then converted to the moles of S atoms and compared to the moles of S atoms in our CZTS nanocrystal film (25 nm NCs), yielding a $1.4 \cdot 10^{-5}$ as the fraction of sulfur removed from the film to stabilize CZTS.

Alternatively, we use the speciation data in Figure B.2 to find that S_2 represents only 23.6% of the sulfur vapor at 700 ^{o}C. In this case, the total sulfur pressure is then $7.3 \cdot 10^{-4}$ Torr. We then convert this pressure to moles of S by using the average

speciation, *v*, of 5.16 (from Table B.2, and compare this quantity the moles of S in the CZTS nanocrystal film. This calculation show that the fraction of sulfur removed from a CZTS film to establish a stabilizing sulfur pressure is $1.5 \cdot 10^{-4}$. In either case, the loss of sulfur from a CZTS film in our sealed ampule system is negligible. These calculations support the lack of observation of binary or ternary decomposition species after annealing without S charging.

Table B.6 Calculations of the fraction of sulfur lost from a CZTS nanocrystal film to establish the sulfur pressure necessary to prevent further sulfur loss and stabilize a CZTS film.

Film Width (mm)	8
Film Length (mm)	20
Film Thickness (microns)	2
Packing Density (decimal)	0.6
Particle Size (nm)	25
Ligand Shell Size (nm)	1
Carbon Count in Ligand (#)	18
Density of Ligands (# per cm^2)	9.00E+13
Mass of Sulfur (mg)	1
Temp (C)	700
Ampule volume (cm^3)	7.85

Film Volume Total (mm^3)	Solid Volume (including ligand) (mm^3)	# Particles in Film (with ligand)	Total Particle Surface Area (cm^2)	#moles Ligands	# moles C-atoms in Film	# moles S-atoms in Vapor
0.32	0.192	1.86E+13	3.66E+02	5.47E-08	9.84E-07	3.12E-05

# S-atoms in Film	Moles S-atoms in Film
1.90E+18	3.16E-06

S2 Pressure for CZTS Stability (Torr)	<--Mol S-atoms Equivalent	Fraction of S-atoms Removed From Film	# S atoms removed from each NC
1.73E-04	4.47E-11	1.41E-05	2.89
Total S_4.22 Pressure for CZTS Stability (Torr)	<--Mol S-atoms Equivalent	Fraction of S-atoms Removed From Film	# S atoms removed from each NC
7.31E-04	4.88E-10	1.54E-04	31.56

B.6 References

1. D.-Y. Peng and J. Zhao, *J. Chem. Thermodyn.*, 2001, **33**, 1121–1131.
2. E. H. Baker, *J. Chem. Soc. A*, 1968, 1089–1092.
3. H. Rau, T. R. N. Kutty, and J. R. F. Guedes De Carvalho, *J. Chem. Thermodyn.*, 1973, **5**, 833–844.
4. H. Rau, *J. Chem. Thermodyn.*, 1974, **6**, 525–535.
5. B. S. Tosun, B. D. Chernomordik, A. Gunawan, B. Williams, K. A. Mkhoyan, L. F. Francis, and E. S. Aydil, *Chem. Commun.*, 2013, **49**, 3549–3551.
6. J. J. Scragg, T. Ericson, T. Kubart, M. Edoff, and C. Platzer-Björkman, *Chem. Mater.*, 2011, **23**, 4625–4633.